Summer 2024

Catalytic Control of the Nanomorphology and Mechanical Properties of Aliphatic Shape-Memory Aerogels

A B M Shaheen ud Doulah
Missouri University of Science and Technology

Department: Chemistry

CATALYTIC CONTROL OF THE NANOMORPHOLOGY AND MECHANICAL PROPERTIES OF ALIPHATIC SHAPE-MEMORY AEROGELS

by

A B M SHAHEEN UD DOULAH

A DISSERTATION

Presented to the Graduate Faculty of the

MISSOURI UNIVERSITY OF SCIENCE AND TECHNOLOGY

In Partial Fulfillment of the Requirements for the Degree

DOCTOR OF PHILOSOPHY

in

CHEMISTRY

2023

Approved by:

Dr. Chariklia Sotiriou-Leventis, Advisor
Dr. Manashi Nath
Dr. Jeffrey Winiarz
Dr. V. Prakash Reddy
Dr. F. Scott Miller

PUBLICATION DISSERTATION OPTION

This dissertation consists of the following two articles, formatted in the style used by the Missouri University of Science and Technology:

Paper I, pages 23-58, has been published in *ACS Applied Polymer Materials*.

Paper II, pages 59-97, has been submitted to *ACS Applied Polymer Materials*.

ABSTRACT

Shape-memory poly(isocyanurate-urethane) (PIR-PUR) aerogels are nanoporous solids that can return to their original shape after being compressed, through a heating actuation step. This thesis compares the effectiveness of various metal ions as catalysts in the formation of PIR-PUR aerogels, and explores the correlation between catalytic activity, nanomorphology, and mechanical properties of the resulting aerogels. The gelation rate was found to increase from Fe to Cu and then decline from Cu to Ga in the periodic table. $CuCl_2$ was found to be the fastest catalyst, and $FeCl_3$ the slowest. The morphology of the aerogels changed from bicontinuous to spheroidal as the catalyst concentration decreased. The elastic modulus (E) was found to be correlated with gelation time, by tuning the nanoporosity of PIR-PUR aerogels.

The shape-memory of PIR-PUR aerogels was also used for synthesizing meta-materials by tuning the micro porous design of flexible aerogels. The shape-memory response of these aerogels has been improved by incorporating an auxetic effect, resulting in a negative Poisson's ratio. This means that the aerogels experience volume contraction upon compression and can be stored indefinitely in a temporary shape by cooling below the glass transition temperature. Upon heating above the glass transition temperature, the compressed form expands to its original shape/size. This technology has various applications in commercial, aeronautical, and aerospace industries, including minimally invasive medical devices, soft robotics, and storage of deployable space structures and planetary habitats during transport.

ACKNOWLEDGMENTS

My profound gratitude goes out to my adviser, Prof. Chariklia Sotiriou-Leventis, as well as my prior advisor, Prof. Nicholas Leventis, for their unwavering support, advice, and genuine interest in my well-being. They helped me with the process of turning my concept into reality as well as with the abundance of information they had to provide. Their systematic and logical approach towards solving a problem has always compelled me and provided a good training for my research. I want to express my gratitude to Dr. Jeffrey G. Winiarz, Dr. Manashi Nath, Dr. V. Prakash Reddy, and Dr. F. Scott Miller for serving on my committee and offering their insightful recommendations as I finished writing my dissertation. I am appreciative of the resources and financial support provided by the Missouri S&T Department of Chemistry and NSF. I would like to thank my group members Hojat, Vaibhav, Rushi, Chandana, Parwani, Suraj, and Stephen for their advice and support during my research. Throughout my PhD program, I received a lot of assistance and friendship, especially from Hojat, Vaibhav, and Rushi.

In particular, I want to thank Shahana Sarmin, my life partner, for her unwavering support throughout my PhD journey. Additionally, I would like to thank my parents, Mr. Shamsud Doulah and Mrs. Gauher Taj Doulah, as well as my brothers and sisters, for their never-ending support and inspiration. They actively encouraged my drive to identify and capitalize into my potential. Words alone are inadequate to convey the depth of my gratitude to them. I would like to extend my gratitude to all my friends and to name a few- Dr. Yaqoob, Himangshu, Galib, Yasin, Palash, for their warm friendship and support during my good as well as tough times.

TABLE OF CONTENTS

Page

LIST OF ILLUSTRATIONS

SECTION Page

PAPER II

LIST OF SCHEMES

SECTION Page

LIST OF TABLES

PAPER I Page

NOMENCLATURE

Symbol	Description
T_g	the glass transition temperature
L_0	distance between neighboring holes
φ	porosity of unit length
G'	the storage moduli
G'	the loss moduli
ε_y	the axial strain
ε_x	the transverse strain
ν	Poisson's ratio
ρ_b	Bulk density
ρ_s	Skeletal density
Π	Porosity
t_{gel}	Gelation time
λ_{Total}	The Total Thermal Conductivity
λ_s	The-Solid Thermal Conductivity
λ_g	The Gaseous Thermal Conductivity
T_f	The Fixation Temperature
T_r	The Recovery Temperature
R_f	The Strain Fixity Ratio
R_r	The Strain Recovery Ratio

1. INTRODUCTION

1.1. AEROGELS – BRIEF HISTORY

Aerogels are solid materials with extremely low density, earning them the nickname "frozen smoke". They are comprised of over 90% empty space, and possess a highly porous, structured framework that imbues them with unique properties such as high surface area, low thermal conductivity and dielectric constants, and high acoustic attenuation. Silica aerogels were the first type of aerogel to be synthesized by S. S. Kistler in the 1930s, through a process involving the conversion of a liquid into a supercritical fluid (SCF) that replaced the pore-filling solvent of wet-gels with air while preserving the gel structure. Kistler also successfully prepared other metal oxide and organic aerogels. Despite recognizing the potential of aerogels for commercial applications, Kistler's method was limited by the time-consuming gelation and solvent exchange process. In 1966, Peri introduced a new process that used alkoxides as precursors for aerogel synthesis, which has since been expanded to include a variety of materials such as non-silica inorganic oxides, organic polymers, carbons, metals and ceramics.

1.2. THE SOL-GEL PROCESS OF SILICA AEROGEL FORMATION

The creation of three-dimensional (3D) porous nanoparticle assemblies is a step in the aerogel preparation process. The size and shape of the pores affect the overall physical qualities, just like with any porous material. Figure 1.1 shows the typical solid network structure of silica aerogels. The solid network is made up of a complicated

hierarchical structure that includes the accumulation of smaller primary particles into fractal porous secondary particles, which eventually aggregate to form a structure like a pearl necklace.

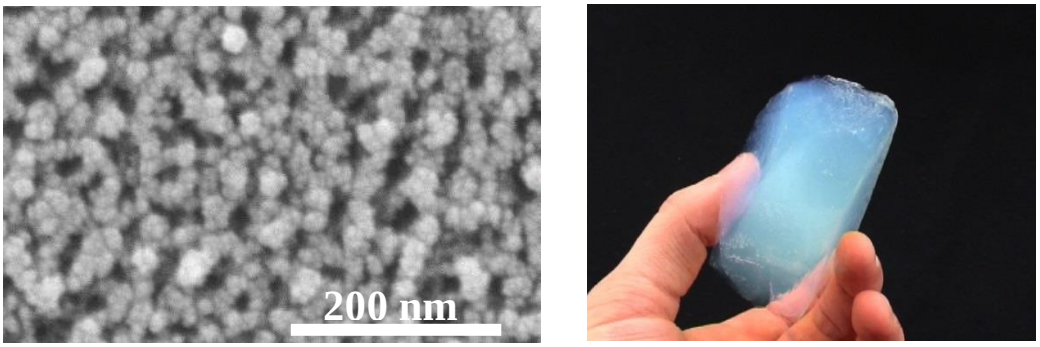

Figure 1.1. The typical nanostructure of a silica aerogel (left) and its macroscopic appearance (right).

Typical alkoxy silane precursors used for the synthesis of silica aerogels include tetramethylorthosilicate ($Si(OCH_3)_4$, abbreviated as TMOS) or tetraethylorthosilicate ($Si(OC_2H_5)_4$, abbreviated as TEOS). Those precursors are dissolved in their respective alcohol, which acts as a co-solvent for the silane and water needed for hydrolysis. Alkoxy silane is first hydrolyzed by either an acid or a base to create silanols, which then undergo an in-place condensation reaction to create Si-O-Si bonds as shown in Scheme 1. The linkages grow in 3D to form a silica network, which in turn yields sequentially primary particles, secondary particles and higher aggregates.[8]

Scheme 1.1. Formation of silica network from the hydrolysis and condensation of TMOS.

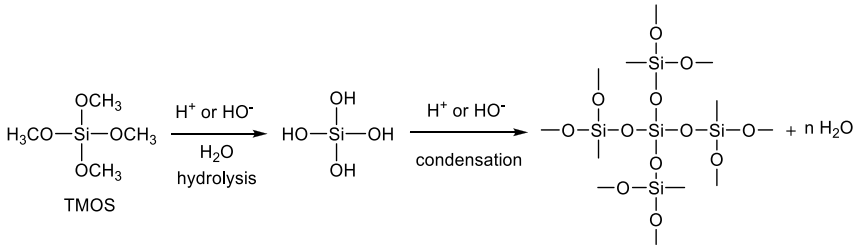

The sol-gel process regulates the formation and aggregation of particles. Aerogels' physical characteristics are actually determined by the size and form of the solid network's pores.[9] As a result, much effort has been made to comprehend and manage the nano-porous structure.[10] Figure 1.2 shows the preparation of silica aerogels via the phase separation of colloidal primary nanoparticles and the mixing of precursors by the sol-gel method, which produces nanoparticles. When enough primary nanoparticles are formed, they are connected to one another to form fractal secondary particles. These secondary particles agglomerate, forming a network that progress in three dimensions to yield a wet-gel. The resulting solvent-filled wet-gels are solvent-exchanged with acetone or alcohol to remove water (other organic solvent for organic aerogels) from the network before drying.

Silica wet-gels can be dried in two different ways resulting in: (a) xerogels created by allowing entrapped solvent to evaporate at air pressure, resulting in a collapsed porous structure with significant shrinkage or, (b) aerogels by using SCF-CO_2 whereas the volume and the porous structure of the original wet-gel are retained. In practice, supercritical drying involves use of an autoclave to replace the gelation solvent with liquid CO_2, which is then converted to SCF and vented off isothermally (critical point of CO_2: 31.1 ^oC at 1072 psi).[10]

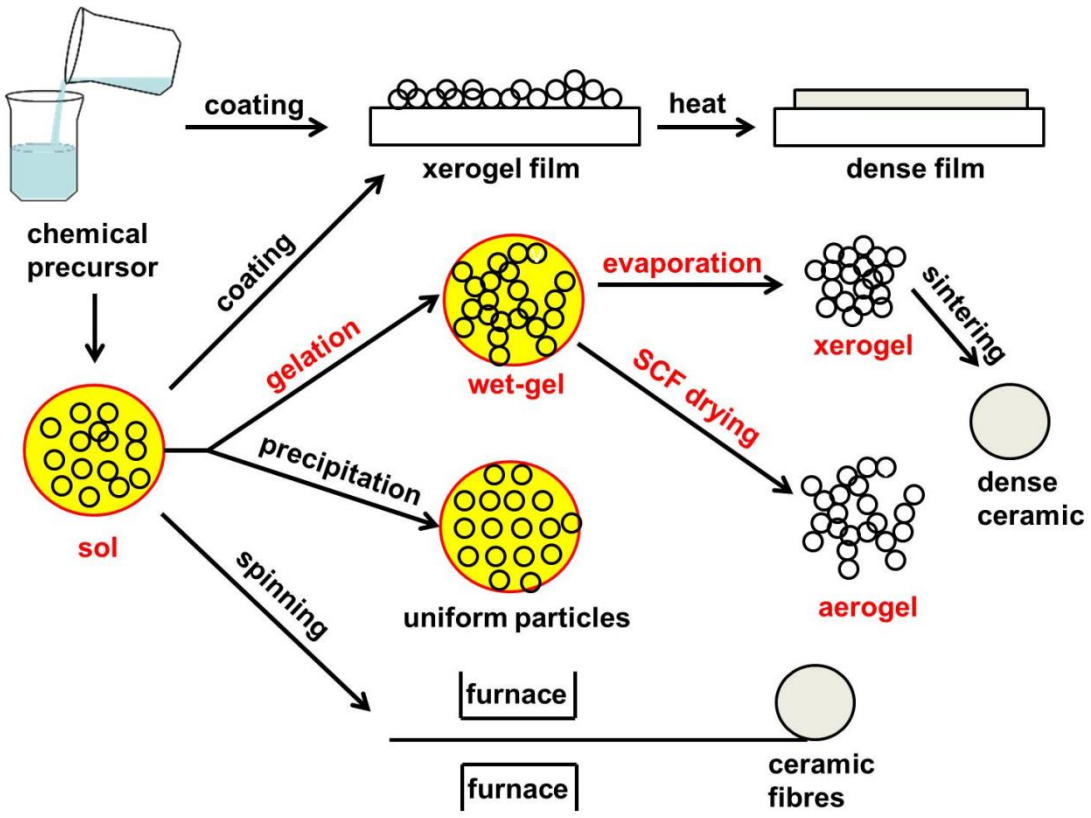

Figure 1.2. Preparation of aerogel via the sol-gel process.

1.3. RESOLVING THE FRAGILITY OF SILICA AEROGELS WITH CROSSLINKED SILICA AEROGELS (X-AEROGELS)

Silica aerogels have been considered for many applications including thermal and acoustic insulation,[11] dielectrics,[12] catalyst supports[13] and as hosts for functional guests in chemical, electronic and optical applications.[14] However, silica aerogels have been actually used only in specialized environments, like as Cerenkov radiation detectors in certain nuclear reactors, aboard spacecraft as collectors for cosmic particles (NASA's Stardust program),[15] and for thermal insulation in planetary vehicles on Mars. The main reason for the slow commercialization of silica aerogels is their fragility and poor

mechanical properties. The poor mechanical properties of silica aerogels are generally attributed to the well-defined narrow interparticle necks.[13] The fragility issue of silica aerogels has been resolved by crosslinking aerogels with organic polymers.[17]

The brittleness of aerogels is mainly due to their nanostructure, which consists of interconnected clusters of nanometer-sized particles. These clusters form a network with many pores and voids, which reduces the amount of material that can resist deformation or fracture. Moreover, the bonds between the particles and clusters are weak and can be easily broken by external forces. The brittleness of aerogels also depends on their composition and synthesis method. For example, silica aerogels tend to be more brittle than carbon aerogels because silica has a lower fracture toughness than carbon.

Briefly, it was realized that skeletal silica nanoparticles possess surface silanol groups, which can react with polyisocyanates to form polyurethane tethers that bridge the nanoparticles chemically, reinforcing the interparticle necks. Thus, the open porosity is kept while the entire skeletal structure is coated conformally with a polymer (Figure 1.3). The resulting materials have been referred to as polymer-crosslinked aerogels (X-aerogels). While crosslinking does not significantly affect any of the other bulk characteristics of X-aerogels, it does result in a 300 increase in the flexural strength of typical X-aerogel monoliths when the bulk density is increased by a factor of 3. X-aerogels are exceptionally strong in comparison not only with their non-crosslinked counterparts (native aerogels), but also with other materials that are usually considered strong, such as steel, Kevlar, and silicon carbide.[18]

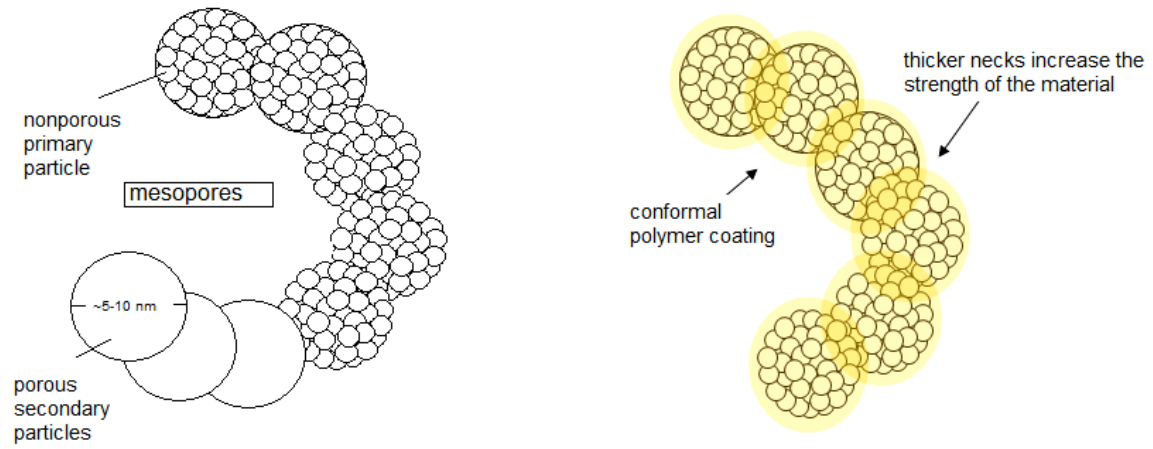

Figure 1.3. On the skeletal silica nanoparticles, a thin polymer film is created conformally.

In X-linked aerogels, the silica nanoparticle framework serves as a template for the accumulation of polymer, which covalently connects the skeletal particles. However, since the exceptional mechanical properties of X-aerogels are traced to the polymer coating, it was reasoned that aerogels made out of the crosslinkers themselves, i.e., purely polymeric aerogels with the same nanomorphology and interparticle connectivity of X-aerogels, should have similar mechanical properties and a much simpler synthetic protocol.

Our most widely used crosslinkers and isocyanates, are industrial precursors for the synthesis of polyurethanes and polyureas.[19] These isocyanate-derived polymers are very robust and their mechanical properties can be easily tuned. Therefore, we explored isocyanates and their chemistry in order to synthesize new soft and flexible porous materials.

1.4. THE CHEMISTRY OF ISOCYANATES

The isocyanate, -N=C=O, is one of the most reactive organic groups. Owing to the electron withdrawing ability of both the oxygen and nitrogen atoms, the electron density at the carbon is much smaller than in a typical carbonyl group (Scheme 2). Therefore, the isocyanate group is susceptible to nucleophilic attack (Scheme 3).

Scheme 1.2. Possible resonance structures of the isocyanate group.

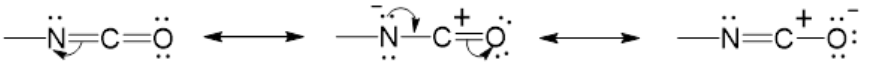

Scheme 1.3. Addition of nucleophile to the isocyanates.

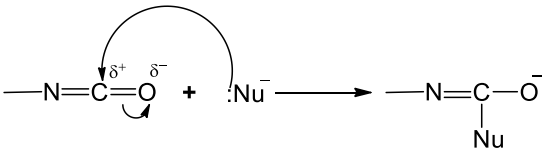

The reactivity of the isocyanate group (N=C=O) is further modulated by electron withdrawing or electron donating groups attached on N. The aromatic isocyanates are generally more reactive than their aliphatic counterparts.[21] In addition, electron-withdrawing substitution on aromatic isocyanates will increase the positive charge on the carbon atom, thereby will increase the reactivity of the isocyanate towards nucleophilic attack when steric factors are neglected.[22] Conversely, an electron donating group (EDG) will reduce the reactivity of the NCO group, as illustrated in Scheme 4. Isocyanates can react with various functional groups and can undergo self-addition reactions.[23]

In particular, below we review the reaction of isocyanates with specific nucleophiles relevant to the synthesis of aerogels.

Scheme 1.4. Decreasing order of isocyanate reactivity in the presence of EDG.

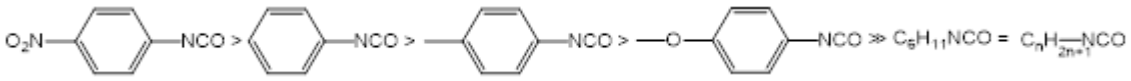

1.4.1. Reaction of Isocyanates with Alcohols. The addition reaction between an isocyanate and an alcohol yields urethane. The stoichiometry of the reaction is illustrated in Scheme 1.5.

Scheme 1.5. Formation of urethanes from isocyanates and alcohols.

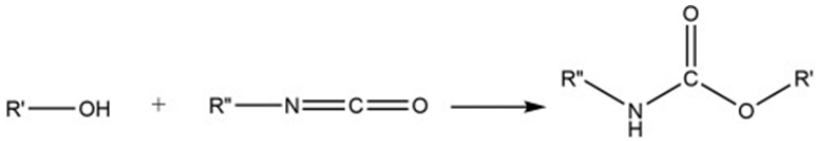

The reactivity of alcohol is reduced from primary to secondary for steric reasons. Due to the resonance delocalization of the electron pair on oxygen to the aromatic ring, phenols are even less reactive. Due to alcohols' typically limited reactivity with isocyanates, Lewis acids or bases are frequently used to catalyze the synthesis of urethane.

1.4.2. Lewis Acid/Base Catalyst Mechanism for Urethane Synthesis. The generally accepted mechanism proposed for the dibutyltin dilaurate (DBTDL) catalyzed

reaction of isocyanate with alcohol can be viewed as a Lewis acid type mechanism involving polarization of the carbonyl by the metal complex followed by nucleophilic attack of the alcohol.[24]

Scheme 1.6. Formation of urethanes by Lewis acid/base mechanism.

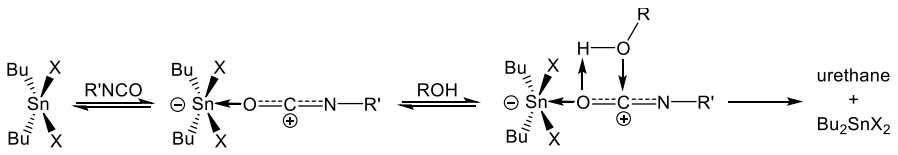

Urethanes can be synthesized by base-catalysis, which involves the reaction of an alcohol with an isocyanate in the presence of a base. The base acts as a catalyst by deprotonating the alcohol and activating it for nucleophilic attack on the isocyanate carbon. Baker *et al.* explained the formation of polyurethanes via tertiary amine (B) catalysis in dibutyl ether as solvent.[25,26]

Scheme 1.7. Formation of urethanes according to Baker *et al.*

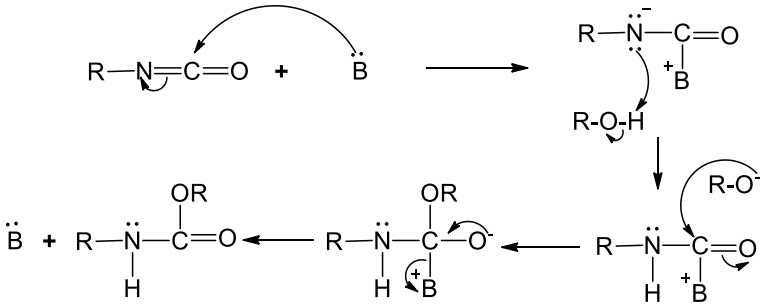

Scheme 1.8. Formation of urethanes from isocyanates and alcohols by base catalysis.

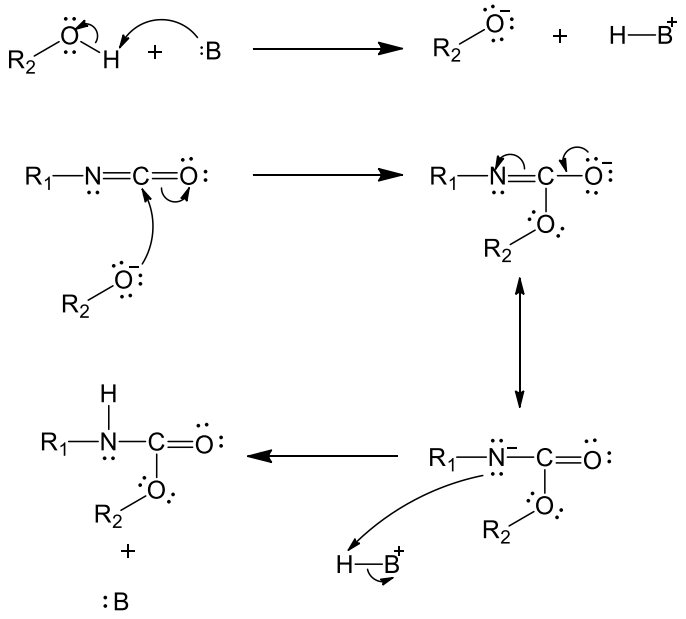

1.4.3. Urethanes by Insertion Method. The reaction of metal catalyst with isocyanates and alcohols is an efficient way to synthesize urethanes. The mechanism of this reaction has been investigated by several authors and the results indicate that the alcohol plays a crucial role in activating the metal center. The coordination of the alcohol to metal centers like $Zr(OAc)_4$ leads to the formation of an alkoxide complex, which can be either a pentacoordinate or a hexacoordinate species depending on the steric and electronic factors.[27] The alkoxide complex then reacts with the isocyanate to form an insertion intermediate, which undergoes nucleophilic attack by another alcohol molecule to yield the urethane product and regenerate the alkoxide complex (Scheme 8). This mechanism differs from the conventional Lewis-acid catalyzed reaction, where the isocyanate coordinates to the metal center first and then reacts with the alcohol.

This proposed mechanism is consistent with all the authors and provides a rational explanation for the high selectivity and efficiency of this reaction.

Scheme 1.9. Formation of urethanes from isocyanates and alcohols by insertion.

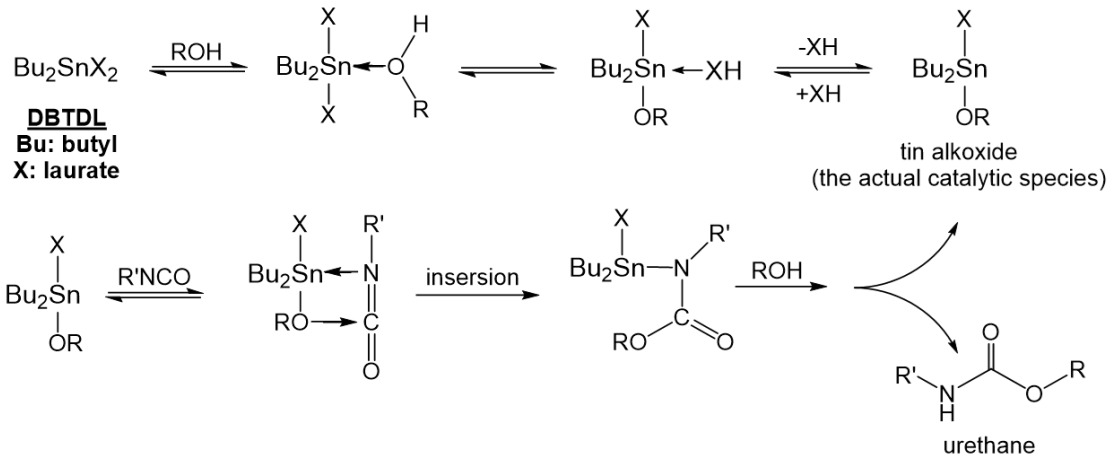

1.5. ORGANIC AEROGELS

Organic aerogels are more diverse in terms of flexibility and mechanical strength. This type of aerogels is made from different polymers such as polyurethane, polyurea, polyamide, polyimide, different composite of polymers, etc. The majority of recent research on organic aerogels has focused on carbon aerogels, with high yield resorcinol-formaldehyde (RF) aerogels serving as key raw materials in the production of carbon aerogels upon pyrolysis.[32] Subsequently, several other types of organic aerogels were reported such as polyurethane, polyurea, polybenzoxazine, ring opening metathesis polymerization (ROMP) derived, polyacrylates and more recently polyimides. The

targeted practical applications have always been in the area of thermal insulation as well as hydrogen storage, catalysis, energy storage, etc. (Figure 1.4).

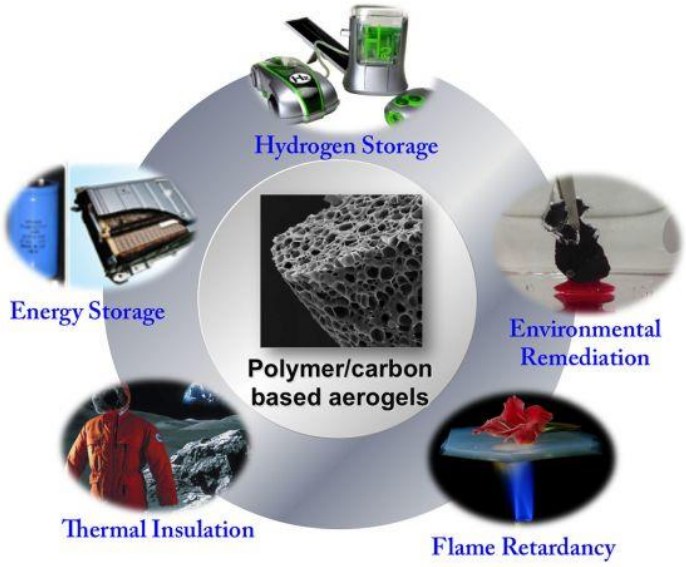

Figure 1.4. Applications of organic aerogels.

In this work, we focused on how we may improve the flexibility of aerogels by tuning their nano-morphology and micro-morphology utilizing polyurethane aerogel chemistry, while we rely on our experience with aerogels in which we confronted the issues associated with the rigidity of aerogels.

For a very long time polyurethane (PU), the reaction product of multifunctional isocyanate and polyols[19], was well-established in foams, elastomers, fibers, sealants, adhesives, and coatings.[21] By modifying the reagents' chemical identities with chain extenders and/or crosslinkers, their mechanical properties can be customized.[21] Polyurethane foams in particular are extremely successful in thermal barrier

applications.[33] Moreover, polyurethane (PU) aerogels are porous and also desirable for thermal insulation.

1.5.1. Polyurethane Aerogels. Polyurethane (PU) aerogels were first reported without chemical identification in 1998 by Biesmans, who used Suprasec DNR (an aromatic oligomeric isocyanate) and 1,4-diazabicyclo[2.2.2]octane (DABCO) as a catalyst.[34] Curiously, no alcohol was reported, and the materials were referred to as polyurethanes and polyisocyanurates almost interchangeably. Figure 1.4 shows the thermal conductivity of polyisocyanurate aerogels as a function of pressure. At 0.21 g cm^{-3}, those materials possessed exceptionally low thermal conductivity values (0.0085 W m^{-1} K^{-1} for evacuated and 0.015 W m^{-1} K^{-1} for air filled samples), and they were carbonizable with 40% w/w yield upon pyrolysis under inert atmosphere.[34]

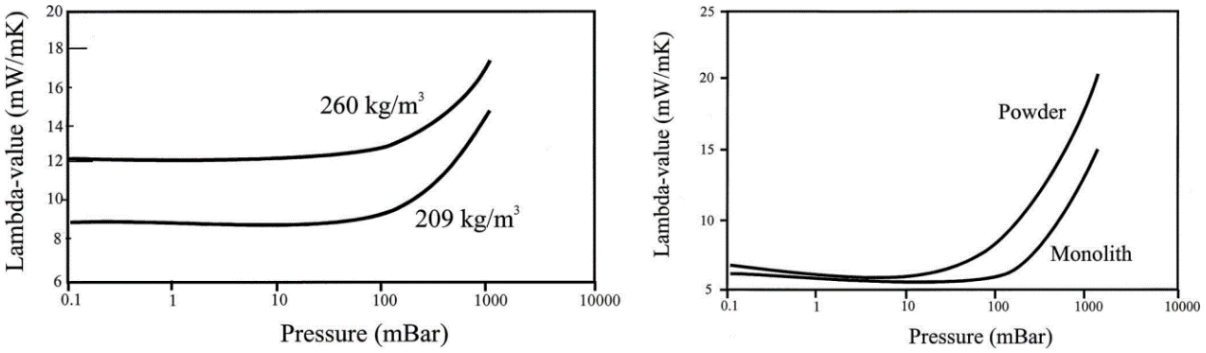

Figure 1.5. Thermal conductivity of polyisocyanurate aerogels as a function of pressure.

The monolith (ρ_b = 0.1 gcm^{-3}) has been measured and pulverized to particles with a size below 50 μm. The thermal conductivity of the pulverized aerogel has once again been measured, and Figure 1.4 displays the trend as a function of pressure. In order to

enhance the mechanical properties of silica aerogels, Yim *et al.* reported silica-polyurethane hybrid aerogels in 2002. These aerogels demonstrated thermal conductivity of 0.0184 W m^{-1} K^{-1} at 1 torr for aerogels with bulk density of 0.07 g cm^{-3}.[36] In 2004, Rigacci *et al.* revisited PU aerogels with emphasis on thermal superinsulation, and synthesized materials from Lupranat M20S [4,4´-methylenebis (phenylisocyanate)] and two aliphatic polyols, saccharose and pentaerythritol, using DABCO as catalyst in DMSO/ethyl acetate mixtures.[37] Both supercritical and subcritical drying routes were used and the resultant materials were compared in terms of bulk density, pore volume, and thermal conductivity. The latter was less than that of polyurethane foam (0.022 versus 0.030 W m^{-1} K^{-1} at room temperature and atmospheric pressure). Importantly, it was further shown that the aerogel morphology depends on the solubility of the precursors as well as the solubility parameter (δ_m) of the reaction medium. When δ_m was lower than the solubility parameter of the polyurethane (δ_{PU}), the aerogel consisted of aggregates of micrometer sized particles; if $\delta_m > \delta_{PU}$, smaller-sized particles and mesoporous structures were reported.[37]

1.5.2. Rigid PU Foams. These foams can be utilized primarily as materials for energy-efficient insulation and can give appliances and automobiles added structural strength.[38] They have been used as barrier sealants as well as windows due to their efficient insulating qualities. They can be made from polyols derived from petroleum or from biomaterials. The kind of polyol employed affects how the resulting PU foams behave. Numerous investigations have been conducted to find alternatives to petroleum-based polyols, such as polyols derived from plants. High flame-retardant qualities can be seen in PU foams made from soybean oil.[39] Incorporation of nano clays increases the

thermal stability of PU foams with light weight, increased compressive strength and good flame-retardant properties. Incorporation of polyisocyanurate (PIR) in the rigid PU foams can be used to insulate buildings.[40] They are synthesized from the trimerization of aliphatic or aromatic isocyanates upon heating whose forward reaction is more favored than the backward reaction. Due to high crosslinking, the rigid foams have closed pores and hence trapped solvents in the pores. Therefore, the solvents with low thermal conductivities are preferred for the synthesis of rigid foams.[41]

1.5.3. Flexible PU Foams. Flexible polyurethane foams are synthesized by three separate and consecutive processes: blowing, polymerization and crosslinking process. In the blowing process, the reaction of isocyanate with water that is trapped by the reaction mixture results in the formation of CO_2 and urea, whereas the reaction of isocyanate and alcohols results in the formation of urethane bonds. The CO_2 acts as blowing agent. Apart from CO_2, other blowing agents are methylene chloride, chlorofluorocarbon, etc. These blowing agents are chemically inert and are only used to expand the foam by vaporization.

In the second step, the isocyanate reacts with diols to form polyurethanes. In the third step i.e., the crosslinking step, the morphology and microstructure are varied. Flexible PU foams consist of block copolymers of two or more segments and their flexibility is controlled by the phase separation of the soft segment and the hard segment.[42] By varying the proportion of the soft and hard segments, the flexibility of these foams can be adjusted. Applications of flexible PU foams include cushion materials, carpets, furniture, packaging, and nanocomposites.[41] Flexibility can be enhanced by using lower crosslinking, lower NCO:OH ratio, and longer chain length of

the monomers. Using longer chain length for monomers, the glass transition temperature of the flexible PU foams decreases. The most commonly used isocyanates for foams are 2,4 and 2,6-toluene diisocyanate, while the alcohols used are polyether polyols with the general formula H-$(CHOH)_m$-CH_2O-$(C_2H_5O)_n$-H. That is, typical polyols are polyether's from active hydrogen compounds like glycerol, sorbitol, sucrose, etc. Though flexible polyurethanes are crosslinked, they have weak tensile and tear properties. To overcome this mechanical issue, flexible PU foams can be reinforced with textile-based fibers of carbon, basalt and aramids.[42]

1.6. MORPHOLOGY OF AEROGELS

Aerogels, usually made of colloidal particles or polymers, have a three-dimensional network structure and are filled with gas.[43] Inorganic aerogels, such as silica aerogels, have a high surface area and porosity with a morphology of connected particles that have various neck sizes. According to a 2005 study by Leventis et al.,[44] the morphology varies depending on the processing method (Figure 1.6).

Different groups suggested that the modification of morphology enhances the mechanical, optical and rigidity propereties.[43,45,46] Silica aerogels highly porous materials that consist of a nanostructured solid network of silica particles. These particles are formed as a result of a hydrolysis and condensation process of the silica precursor molecules, in which siloxane bridges (Si-O-Si) are formed. (Figure 1.6) Such reactions are equivalent to a polymerization process in organic chemistry, where bonds between the carbon atoms of organic precursors lead to linear chains or branched (cross-linked) structures.

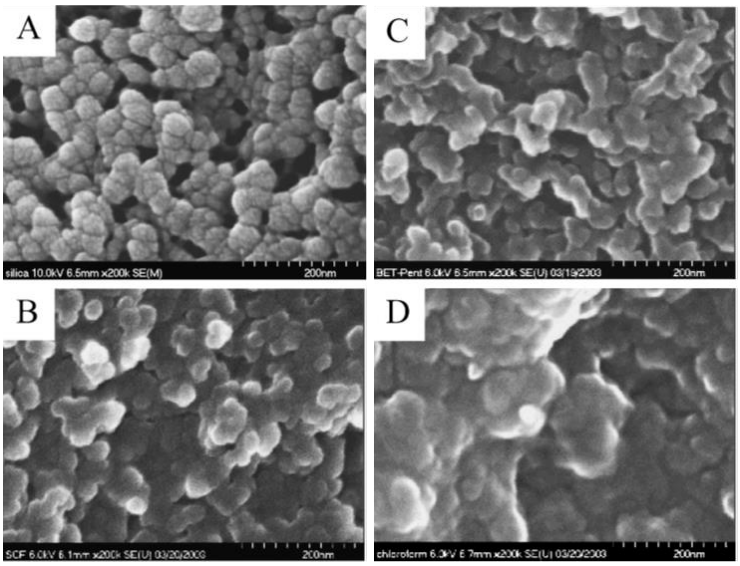

Figure 1.6. SEMs of a native silica aerogel monolith (A), and of three SCF-CO_2 dried cross-linked silica aerogel monoliths re-processed as follows. (B): no further processing; (C): soaked in pentane and redried at ambient pressure at 40°C for 2 d; (D): soaked in chloroform and re-dried at ambient pressure at 40°C.

The form of organic aerogels is greatly influenced by the microphase separation. The degree of microphase separation depends on the balance between the kinetic and thermodynamic factors that drive the polymerization and cross-linking reactions. At low precursor concentrations and high catalyst amounts, the polymerization is fast and favors the formation of smooth-surfaced domains with a non-fractal structure. These domains are correlated in a non-self-similar fashion, resulting in a hierarchical porous network with large pores and high surface area. At high precursor concentrations and low catalyst amounts, the polymerization is slow and allows for more thermodynamic control over the structure formation.

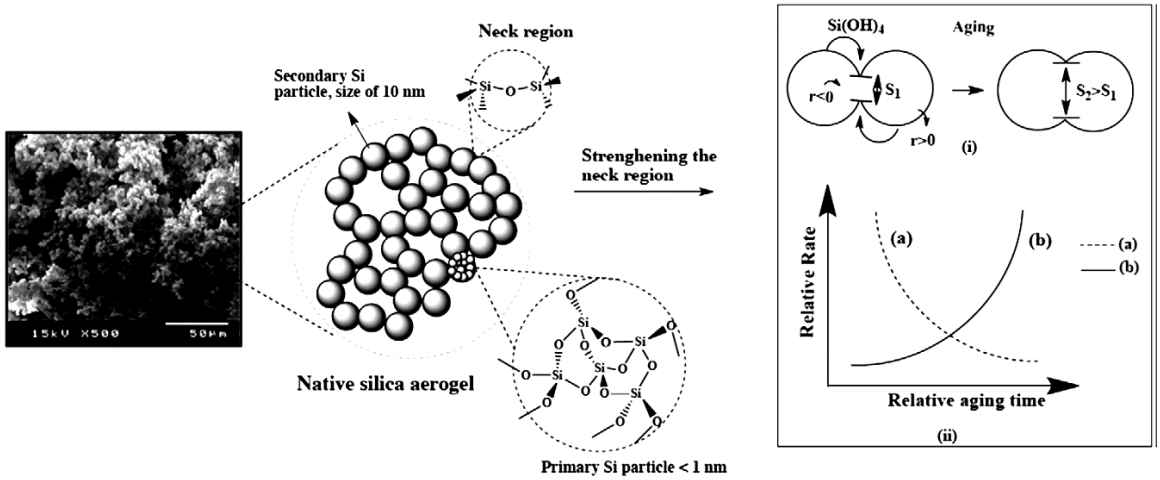

Figure 1.7. Silica aerogels with schematic representation of primary and secondary silica particles (left); (i) neck growth mechanism of secondary silica particles and (ii) relative aging rate as a function of time for two mechanisms (a, b).

This leads to the development of fractal microstructures with rough surfaces and self-similar scaling. These microstructures have smaller pores and lower surface area than the smooth-surfaced domains.[46]

1.7. TUNING OF MECHANICAL CHARACTERISTICS

Silica aerogels are the most widely studied and used aerogels due to their high thermal insulation and low density, but they are still brittle and prone to cracking under stress. Several attempts to address the mechanical properties by conformal coating with a crosslinker or making composites with fibers or graphene oxides showed significant improvement.[46] In a 2019 k-index publication, the Leventis research group demonstrated that the morphology has a significant impact on the physical characteristics of polyurea gels.[47] Continuing the inquiry of how morphology affects mechanical properties In this thesis, the relationship between morphology and mechanical properties was established to

support the idea. This was done by altering the catalyst's concentration or type, integrating micro-voids using templates, or applying air pressure.

1.8. 3D TEMPLATING TO INCORPORATE POROSITY

3D templating is a technique that uses sacrificial templates to create complex porous structures with high fidelity and tunability. This technique involves coating a template material with a desired material and then removing the template by thermal decomposition, dissolution or etching.[49] The resulting structure inherits the shape and size of the template, but with a porous network that can be tailored by varying the materials.[50] Moreover, 3D templating can utilize a wide range of template and coating materials, enabling the fabrication of multifunctional and composite porous materials.

The templates are fabricated by 3D printing or other methods, and then infiltrated with a matrix material such as polymer, metal, or ceramic. After curing or solidification, the templates are removed by dissolution(organic solvents), pyrolysis, or etching (CO_2 or acid), leaving behind porous materials with the desired morphology.[49] The general route for templated synthesis of nanostructured materials includes the following steps: (1) template preparation, (2) directed synthesis of target materials using the template, and (3) template removal (if necessary).

1.8.1. Additive Manufacturing (3D Printing) for Template Preparation.

Additive manufacturing (AM), often known as 3D printing, was first developed in the 1980s to meet the highly specialized needs of model creation and rapid prototyping (RP). It has since become a flexible technology platform for computer-aided design (CAD) and rapid production. Customized items made of metals, ceramics, and polymers can be

produced via additive manufacturing (AM) without the use of molds or machining necessary for traditional formative and subtractive fabrication.[50] Today's commercially accessible 3D printers cost less than $500, making it possible to create 3D items on a desktop even at home.AM allows the production of 3D structures with high shape complexity. Although a coffee mug is not very complex, it provides a convenient object to demonstrate the concepts of AM (Figure 1.6).[51] One possible way to create a negative mold with tiny voids is to use a 3D printer that can produce high-resolution (100–150 m) models. A prototype design that can serve as a template for adding tiny voids can be 3D printed using a suitable material and then removed from the mold. The resulting negative mold can then be used to cast other materials with the desired microstructure.

1.8.2. Meta Materials or Auxetic Behavior. Meta-materials are artificial materials that exhibit properties that are not found in nature.[52] They are composed of periodic or quasi-periodic arrangements of subunits that interact with electromagnetic waves, sound waves, or mechanical forces. By manipulating the shape, size, orientation, and material of the subunits, meta-materials can achieve negative refractive index, negative Poisson's ratio, negative thermal expansion coefficient, and other unusual phenomena.[53-54]

Poisson’s ratio, denoted ν and named after Siméon Denis Poisson (1787-1840), as a measure of the Poisson’s effect, is employed to characterize a material, which is the property of materials to expand (contract) in directions perpendicular to the direction of compression (tension). Poisson[55] defined the ratio ν between transverse strain (e_t) and longitudinal strain (e_l) in the elastic loading directions as $\nu = -e_t/e_l$. Negative Poisson’s ratio materials are referred to as NPR material. The most notable example of this is how

they contract under uniaxial compression rather than expanding in the transverse direction.

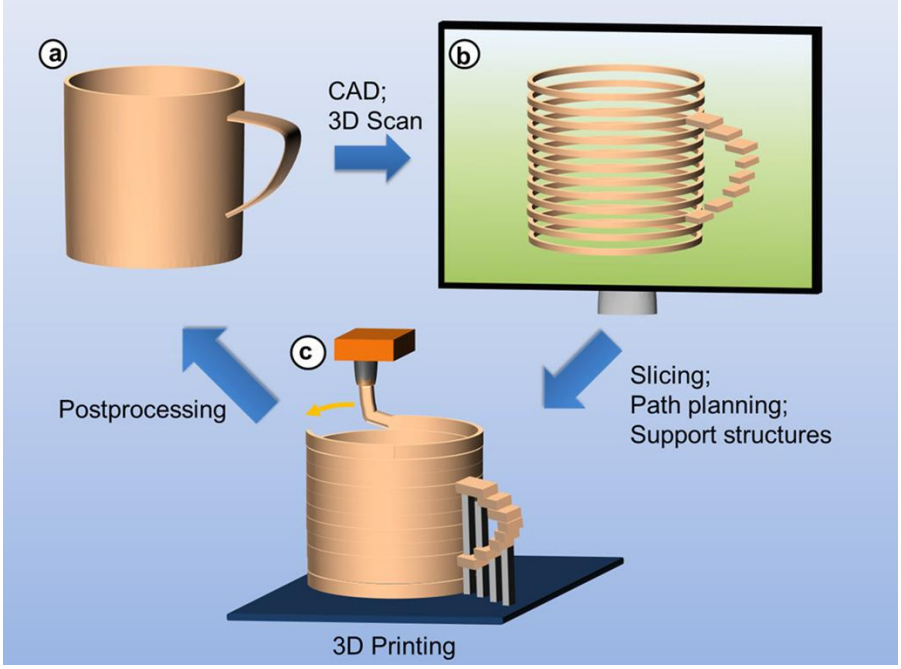

Figure 1.8. Basic principles of additive manufacturing. (a) Development of product idea by means of CAD or 3D scanning; (b) preprocessing of model data: slicing of virtual model into layered data, adjustment of support structures to stabilize craning structures, path planning, and successive transfer of layered data to 3D printer; (c) and additive manufacturing of model or product by melt extrusion.

Two-dimensional periodic porous structures recently attracted considerable attention because of dramatic transformations of the original geometry observed as the result of mechanical instabilities.[56] Upon reaching a critical applied stress, a square array of circular holes in an elastomeric matrix is found to suddenly transform into a periodic pattern of alternating, mutually orthogonal ellipses. This behavior has been demonstrated to provide opportunities for the design of materials with tunable negative Poisson's ratio.[57]

A negative template for an oval-shaped repeating unit can be created via 3D printing. As per Bertoldi, negative Poisson's ratio will be observed with those oval shapes after removing the template. In this research, we examined whether PIR-PUR shape memory aerogels' mechanical properties were improved by large voids. Also, we examined the auxetic behavior to explore further applicability of flexible aerogels.

PAPER

I. META-AEROGELS: AUXETIC SHAPE-MEMORY POLYURETHANE AEROGELS

ABSTRACT

Shape-memory poly(isocyanurate−urethane) (PIR−PUR) aerogels are low-density monolithic nano porous solids that remember and return to their permanent shape through a heating actuation step. Herein, through structural design at the macro scale, the shape-memory response is augmented with an auxetic effect manifested by a negative Poisson's ratio of approximately −0.8 at 15% compressive strain. Thus, auxetic shape-memory PIR−PUR monoliths experience volume contraction upon compression at a temperature above the glass transition temperature of the base polymer ($T_g \approx 30$ °C), and they can be stowed indefinitely in that temporary shape by cooling below T_g. By heating back above T_g, the compressed/shrunk form expands back to their original shape/ size. This technology is relevant to a broad range of industries spanning the commercial, aeronautical, and aerospace sectors. The materials are referred to as meta-aerogels, and their potential applications include minimally invasive medical devices, soft robotics, and situations where volume is at a premium, as for example for storage of deployable space structures and planetary habitats during transport to the point of service.

1. INTRODUCTION

The shape-memory effect is a mechanical material property by which a material remembers and can be triggered to return to a permanent shape after it is deformed to and stored in a so-called temporary shape. The temporary-to-permanent shape transition is triggered by an external stimulus such as heat,[1] light,[2] humidity,[3] pH,[4] or electric and magnetic fields.[5] Shape-memory materials have many potential applications in medical technology,[6,7] implantable and wearable devices,[8,9] robotics,[10,11] and unassisted deployable structures aboard various aerospace platforms.[12,13] The typical trade-off in many of those applications is between mass density and mechanical strength. Yet lightweight, but at the same time high-toughness structural components are needed in applications ranging from delicate devices of interest to the reconstructive orthopedic surgery and implantable cardiovascular devices,[14–16] to large structures of interest to the aeronautical and aerospace industries.[17] In that regard, thermally triggered, shape-memory polymers are particularly attractive.[18,19] One further refinement in the weight-to-performance ratio of shape-memory polymers was demonstrated recently by introducing polymeric shape-memory aerogels.

Aerogels are low-density three-dimensional nanostructured solids, mainly pursued for thermal insulation management in terrestrial, and aerospace, environments.[20–22] The "aero" part of the name "aerogel" points to the fact that they are prepared from wet gels by replacing their pore-filling solvent with air. This wet-gel origin of aerogels comprises their distinguishing difference from other aerogel-like micro- or nano-cellular structures. In practice, the major concern during the drying process of wet gels is how to halt

collapse of the skeletal framework during solvent removal; this is carried out by first replacing their pore-filling solvent with a low surface-tension liquid, such as liquid CO_2, which is then converted to a supercritical fluid that is vented off like a gas. The most well studied class of aerogels is based on silica.[20,23,24] However, silica aerogels are notorious for their fragility, which limits the range of their applications. One way to address the fragility issue of oxide aerogels is to apply a conformal nano-thin polymer coating over their entire skeletal framework.[25−28] These materials are referred to as X-aerogels, and their strength-to-mass ratio renders them suitable even for ballistic protection (armor).[29−31] The topology of the nanoscopic composition of X-aerogels directed the rational design and development of purely polymeric aerogels from all major classes of polymers ranging from polyolefins,[32] and phenolic resins including polybenzoxazines,[33] polyimides,[34] polyamides,[35] and polyureas[36] to polyurethanes.[37−39] The latter class of aerogels includes recently reported rubber-like super-elastic poly(isocyanurate−urethane) (PIR−PUR) aerogels that show a strong nanostructure-dependent shape-memory effect triggered by a temperature swing around their glass transition temperature.[40−42]

On the other hand, mechanical metamaterials exhibit auxetic physical properties such as negative Poisson's ratios,[43,44] the most striking manifestation of which is that under uniaxial compression they shrink instead of expanding in the transverse direction.[45] Such auxetic material designs have been utilized in biomedical devices, e.g., as artificial arteries, the wall thickness of which increases, rather than decreases, under the tension exerted during pulse-driven blood flow, thus enhancing the artery structural integrity, and thereby its lifespan.[46] Overall, materials with a negative Poisson's ratio tend to be more

resilient to impact and indentation, and thus they are attractive for body armor technologies such as in bullet-proof helmets and vests.[47,48]

A large class of auxetic metamaterials comprises macroscopic structures based on blocks of rubber-like elastic polymers perforated through their bulk by a periodic arrangement of parallel tubes. i.e., tubes placed at regular intervals.[43,49] Since shape-memory polymeric aerogels are super-elastic to begin with, it was reasoned that fabrication of such auxetic meta-structures with polymeric aerogels that show the shape-memory effect would comprise a new class of materials, referred to herewith as meta-aerogels, which will be especially suitable as deployable panels in aerospace applications as they will contract and occupy less space during stowing in their folded temporary shape on their way to the location of their deployment in their permanent shape.

This concept is explored here with shape-memory PIR− PUR aerogels prepared via a sol−gel method with a commercial aliphatic isocyanurate-based triisocyanate (Desmodur N3300A), and triethylene glycol (TEG). The PIR− PUR sol was cast in suitable molds fabricated using 3D printing of the negative of the computer-aided design (CAD) model of the meta-structures of interest. After gelation and demolding, wet-gels were dried to monolithic meta-aerogels perforated with empty parallel tubes of the desired cross-sectional area, shape, and periodicity. Such meta-aerogels were programmed using a thermomechanical compressive load starting at a temperature above the glass transition temperature of the PIR−PUR aerogel. Expressing their negative Poisson's ratio, the PIR−PUR meta-aerogels shrunk under compression; then, while under load, meta-aerogels were cooled to a temperature well below their glass transition, thus fixing their temporary shape indefinitely. Meta-aerogels expanded quickly and

recovered their original permanent shape via a heating actuation step back above their glass transition temperature.

2. RESULTS AND DISCUSSION

2.1. DESIGN AND PREPARATION OF META-AEROGELS

It is well-known that compressible polymeric blocks perforated with transverse parallel voids with specific cross-sectional shape running along the entire length of the blocks at regular intervals show auxetic properties and negative Poisson's ratios.[45,50] Recently, Bertoldi et al. studied the effect of the shape of the cross-section of the tubes on the compressive behavior of such 2D periodic structures and showed that the negative Poisson's ratios through buckling instabilities do depend on the cross-sectional shape of the tubes.[49] The cross-sectional shape of the tubes chosen for this work (Figure 2.1A − inset) was selected as the one with the most negative Poisson's ratio from the shapes investigated by Betroldi.[49] That auxetic structure was reconstructed using the SolidWorks 3D CAD software,[51] using a parametric function in polar coordinates with the center-to-center distance between neighboring holes set at L_0 = 10 mm; the total porosity due to the tubes was set at $\varphi = 0.47$, and the number of repeat unit cells within the structure was set at N = 8. Other details for the design are given in Figure 1 of Appendix A in the Supporting Information. The design was implemented with additive manufacturing as described below.

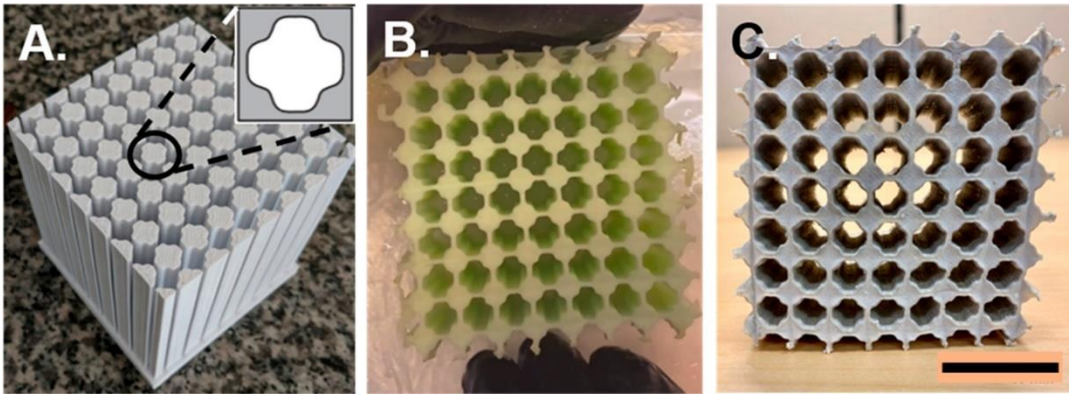

Figure 1. (A) Poly(lactic acid) (PLA) mold: negative of the intended auxetic structure. The pillars become the periodic tubes with the cross-sectional shape shown as an inset. The side faces of the assembly were wrapped around with aluminum tape, and the sol was poured in from the top. (B) Poly(isocyanurate–urethane) (PIR–PUR) wet gel right after demolding. The greenish color is due to the copper catalyst. (C) PIR–PUR meta-aerogel after washing and drying of the wet gel shown in part B. The scale bar in (C) is 2 cm.

Additive manufacturing and specifically desktop 3D printing techniques are emerging as a strong manufacturing tool for rapid prototyping of objects with complex geometries and topologies.[52,53] However, there are still limitations on the types of materials that can be 3D-printed directly. For example, we are not aware of any reports on 3D printed purely polymer aerogels.[54–57] Thus, the target design (Figures 1) was prepared using 3D printing in conjunction with an inverse-molding process,[58] which has been utilized recently to prepare polyimide aerogel based materials with a LEGO brick shape.[59] Accordingly, the desirable meta-structure was used to guide the fabrication of a mold of its negative by subtracting the meta-structure from a solid body that envelops the entire meta-structure. All manipulations were carried out with the SolidWorks software. The mold is shown in Figure 1A. Details for the steps involved in this inverse molding technique, from design to fabrication, are provided in Figure 2 of Appendix A in the

Supporting Information. The spikes in the mold that would eventually become the tubes perforating the meta-aerogel were held in place by the base of the mold, fabricated as an integral part with the spikes; eventually, that base plays the role of the bottom of the molding vessel during the molding process. The molding material for the spikes and the base was poly(lactic acid) (PLA) printed in place directly using the fused-filament fabrication (FFF) method.60 PLA is an extremely versatile molding material,[61] and it was chosen because it is not soluble in our acetonitrile-based sol (see below). The molding vessel was completed by wrapping the outer spikes (i.e., around their perimeter of the 3D-printed object) with aluminum tape. To facilitate demolding of our wet gels, all internal surfaces of the mold were spray-coated with a demolding agent (refer to the Materials and Methods). In case of more complex structures, the PLA mold can be removed by dissolving it away with dichloromethane using Soxhlet extraction.

Adopted from our previous publication on ambient-pressure dried highly stretchable poly(isocyanurate urethane) aerogels,[42] the sol was prepared from an aliphatic isocyanuratebased triisocyanate (Desmodur N3300A) and triethylene glycol (TEG) mixed in their stoichiometric amounts (2:3 mol/mol, respectively) in acetonitrile at room temperature (Scheme 1). Unlike in our previous studies, the urethane forming reaction was catalyzed with anhydrous cupric chloride ($CuCl_2$) in 1:120 mol/mol ratio relative to the triisocyanate. The exact formulations are tabulated in Table 1 of Appendix A in the Supporting Information. The choice of $CuCl_2$ as the catalyst, over the more conventional dibutyltin dilaurate (DBTDL), was based on the fact that it was found to be much more active than the latter for the urethane forming reaction of Scheme 1; in turn, that allowed shortening of the gelation time and facile creation of gels and aerogels with bi-continuous

micro-morphologies that are much stiffer than the spheroidal structures produced by slower gelation with DBTDL.[41] Stiffer materials can store more energy for a given deformation, which was deemed essential for auxetic structures, which, by design, contain less material, because of the tubular voids that render the material auxetic in the first place. For meta-aerogels, stiffer aerogel structures are highly desirable, because, all other factors being equal, at a given strain they can store more energy with less mass. By being less dense by design relative to their simple shape-memory counterparts, meta-aerogels can utilize every bit of extra stored energy for shape recovery.

Scheme 1. Synthesis of the aliphatic PIR-PUR material that comprises the basis for both the regular and the meta-aerogels of this report.

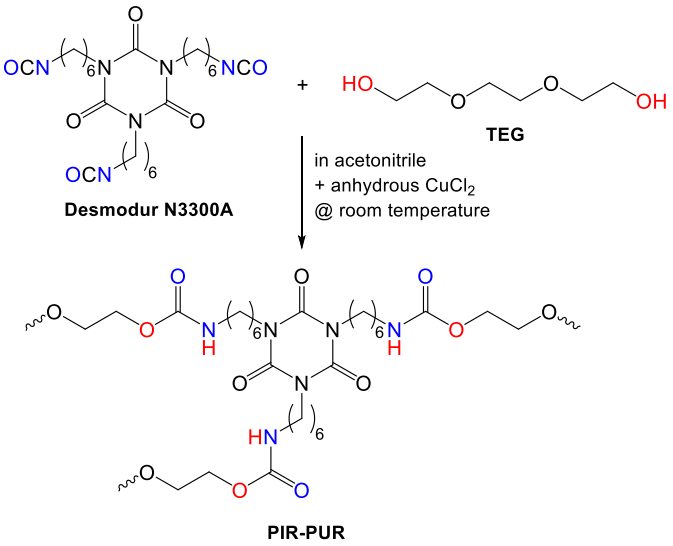

The sol was poured into the molds and the whole assembly was wrapped with parafilm. Gelation took place within 5 min, and the resulting gels were aged in their molds for 1.5 h. Wet gels were then removed from the molds into acetone (Figure 1B). The greenish color was due to the copper catalyst. After four acetone washes and four

pentane washes (24 h each time at room temperature), the pentane-filled wet-gels were let to dry for 24 h at room temperature; drying was completed at 50 °C for 5 h. (Caution! pentane-filled wet gels are a fire/ explosion hazard. Drying from pentane has to be carried out in a well-ventilated fume hood at room temperature.) A dry meta-aerogel is shown in Figure 1C. Sometimes, minor defects introduced during demolding might be observed around the edges of the structure. The auxetic/shape-memory performance, however, as it is described in Section 2.4, remained unaffected.

2.2. MATERIALS CHARACTERIZATION

The PIR−PUR aerogels were chemically characterized using Fourier-transform infrared spectroscopy (FTIR, Figure 2A), and solid-state CPMAS ^{13}C NMR (Figure 2B). The corresponding spectra of PLA are included with red lines, showing no cross-contamination from the molds. The FTIR spectra were dominated by the isocyanurate carbonyl stretch at 1680 cm^{-1} . The 2300−2000 cm^{-1} region was clean of any unreacted N=C=O stretch. The free urethane carbonyl stretch was observed as a 1729 cm^{-1} shoulder to the intense isocyanurate absorption. Possible hydrogen-bonded urethane carbonyl stretches would appear in the 1600−1640 cm^{-1} region, and they were masked by the intense isocyanurate absorption. Methylene (−CH_2−) in-plane bending was observed at 764 cm^{-1} . [62] The urethane N−H stretch was observed as a medium-intensity peak at 3440 cm^{-1} . N−H bending coupled to C−N stretching gave an absorption at 1530 cm^{-1} . [63] The absorptions at 1244, 1120, and 1048 cm^{-1} were attributed to the triethylene glycol and urethane asymmetric and symmetric C−O−C stretches.[63,64] In cross-reference to Scheme 1, the resonances in the 14−44 ppm region of the solid-state ^{13}C NMR spectrum

correspond to the CH_2 carbons coming from Desmodur N3300A. Resonances between 60 and 80 ppm came from the CH_2 groups of TEG. The sharp resonance at 149 ppm corresponds to the carbonyl carbon of the isocyanurate ring. The peak at 156 ppm is attributed to the carbonyl carbons of the urethane groups.[65] In agreement with the FTIR spectrum, no peak corresponding to unreacted N=C=O was detectable.

Microscopically, the PIR−PUR meta-aerogels of this study are classified as bi-continuous materials frozen at an early stage of spherulization along a spinodal-decomposition gelation process (see Figure 2, parts C and D), as the plan was by adopting anhydrous $CuCl_2$ as the catalyst. With a more conventional gelation catalyst like DBTDL, the same sol composition yields similar-density materials with spheroidal morphologies.[42] Bulk material properties of PIR−PUR aerogels and PIR− PUR meta-aerogels are summarized and compared in Table 2.1. Both PIR−PUR aerogels and meta-aerogels undergo similar linear shrinkages relative to their molds (about 25−27%). The entire shrinkage for both types of samples occurred only during their drying process. The skeletal density was common for both types of samples (1.23 ± 0.002 g/cm^3), and their bulk densities were calculated from their weight and physical dimensions. The bulk density of the PIR−PUR aerogels at the current monomer concentration was 0.33 g/cm^3 with porosity equal to 73.5% v/v. As-prepared meta-aerogel samples had a lower density (0.18 g/cm^3) and, correspondingly, a higher porosity (85.4% v/v).

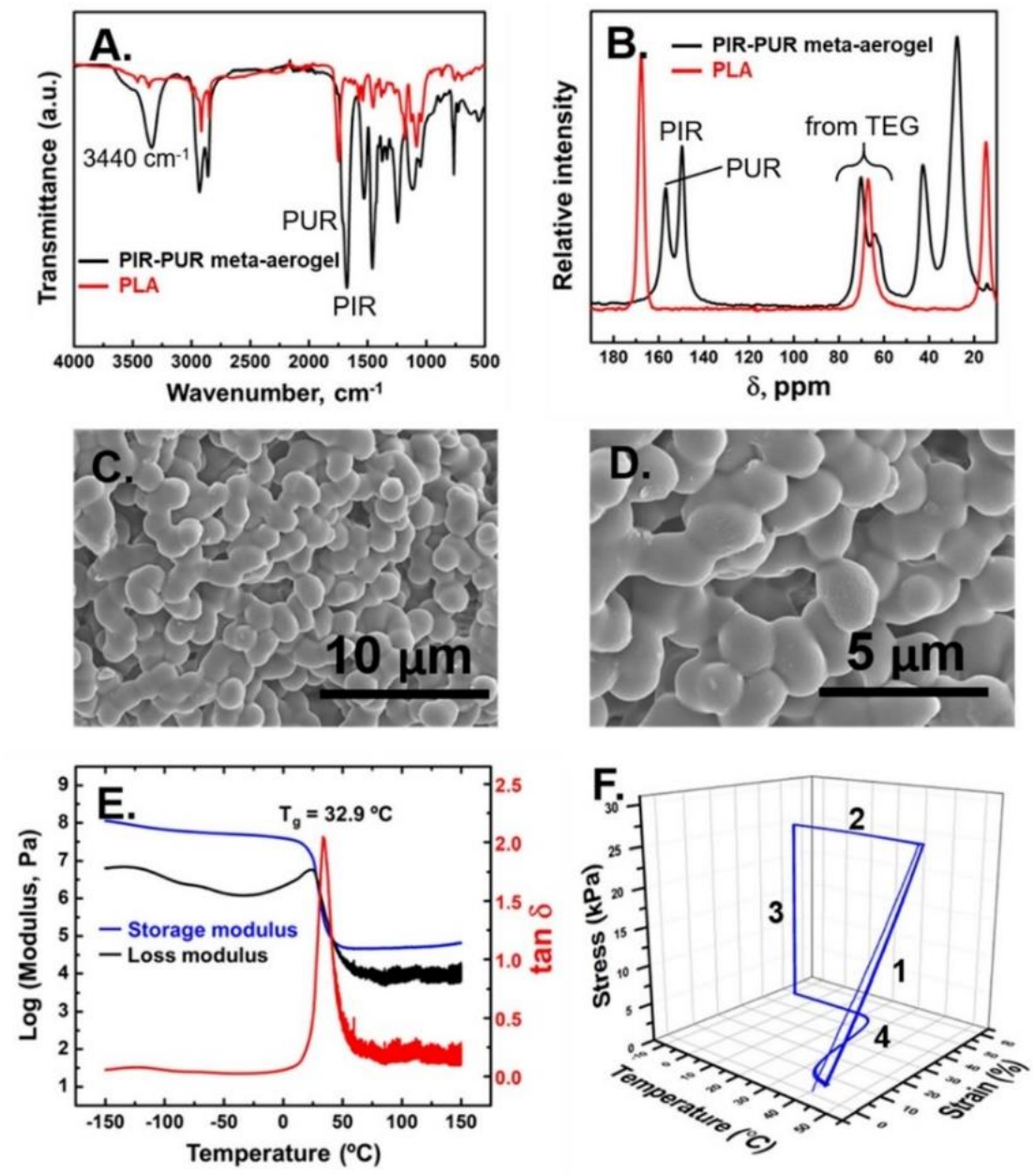

Figure 2. (A) FTIR spectrum of a meta PIR–PUR aerogel. (B) Solid-state CPMAS ^{13}C NMR spectrum of a meta PIR–PUR aerogel. The red-line spectra in frames A and B are those of poly(lactic acid) (PLA, the mold material) showing the absence of cross-contamination. "PIR" refers to features assignable to the isocyanurate ring, and "PUR" to features assignable to urethane. (C, D) SEM image of the PIR–PUR aerogel matrix at two different magnifications showing that the microstructure is bi-continuous. (E) Dynamic mechanical analysis (DMA) at 1 Hz of a PIR–PUR aerogel as a function of the temperature for the determination of the glass-transition temperature (T_g = max tan δ = 32.9 °C). (F) Five thermomechanical cycles of a PIR–PUR aerogel showing the shape-memory effect (see Section 2.2). After the first cycle, the sample became slightly stiffer; the traces from cycles No. 2 to No. 5 coincide.

The glass transition temperature of the PIR−PUR aerogel material was determined with dynamic mechanical analysis (DMA) in tension mode. Figure 2E shows the variation of the storage and loss moduli (G′ and G″, respectively), as well as of tan δ (= G″/G′) of a PIR−PUR aerogel sample at 1 Hz as a function of temperature.

Table 1. Material properties of PIR-PUR aerogel and meta-aerogel samples.

Name	Linear Shrinkage (%)	Porosity (%) [a]	Bulk Density (ρ_b, g/cm^3)	Storage Modulus (kPa) [d]	Loss Modulus (kPa) [d]
PIR-PUR Aerogel	24.5 [b]	73.5	0.33	291.74	79.38
PIR-PUR Meta-aerogel	26.6 [c]	85.4	0.18	11.93	2.74

Skeletal Density (ρ_s) is 1.23 ± 0.002 g/cm^3.
[a] Porosity = 100×[($\rho_s - \rho_b$) / ρ_s].
[b] Linear Shrinkage = 100×[(Mold diagonal – Sample diagonal) / Mold diagonal].
[c] Linear Shrinkage = 100×[(Mold length – Sample length) / Mold length].
[d] DMA in compression at 50 ºC using an excitation frequency of 1 Hz.

At low temperatures, the storage modulus was about 100 times higher than the loss modulus; as the temperature increased, the values of both moduli decreased and crossed one another. Eventually, at the high-temperature plateau, G′ ≈ 10 G″. The glass transition temperature, T_g, of the PIR−PUR aerogel was determined as the peak of tan δ (32.9 °C). This value was used to set the range for the appropriate T_{high} and T_{low} temperatures during the shape-memory thermomechanical cycling. Thus, it was noted that the low-modulus state started to get stabilized at about 40 °C, and Thigh was set equal to that temperature. Correspondingly, T_{low} was set at −10 °C, i.e., about 40 °C lower than T_g. The inherent shape-memory capability of the PIR−PUR aerogels was

confirmed with thermomechanical cycling between T_{high} and T_{low} as shown in Figure 2F. In the beginning, an as prepared (i.e., previously unstretched) sample was first equilibrated at T_{high} = 40 °C for 5 min. Then, in Stage 1 of the curve in Figure 2F, the sample was stretched near its yield strain (60%). At that point (Stage 2 in Figure 2F), the load (stress) was kept constant while the temperature was reduced at 5 °C/min to T_{low}(−10 °C). Subsequently, in Stage 3, the sample was unloaded isothermally (at −10 °C). Finally, in Stage 4, strain recovery was recorded while the temperature was increased to T_{high} (at 1 °C/min). After a 15 min isothermal hold at T_{high}, the cycle was repeated another 4 times. In agreement with our previous findings based on similar aerogels with a spheroidal morphology,[40,41] in the second cycle and beyond the sample settled, becoming stiffer (modulus = 131 kPa), and all thermomechanical curves coincided with one another. Previous stress−relaxation experiments of the same PIR−PUR base material (made with a different catalyst at different morphologies) at T_g + 40 °C, at T_g and at T_g − 40 °C, in conjunction with ATR-FTIR have shown that settling after the first heating-stressing cycle is accompanied by maximization of the H-bonding interactions of the NH group with the carbonyl groups along the backbone and the glycol groups from TEG.[40,41] Various projections of the 3D data of Figure 2F on the planes of the figure are shown in Figure 3 of Appendix A. Those projections allow calculation of the figures of merit of the shape-memory effect (see Table 2 of Appendix A). These figures of merit were found similar to those reported in our previous studies:[40,41] strain fixity ratio ∼99%, strain recovery ratio ∼80%, strain recovery rate ∼5 min^{-1} , and the overall fill factor ∼0.59.

2.3. DEEP RUBBERY-STATE VISCOELASTIC PROPERTIES OF PIR−PUR AND META-PIR-PUR AEROGELS

As a preamble to the thermomechanical testing of the meta-aerogels, we looked at the equivalency of the PIR−PUR aerogels in their regular versus auxetic forms (i.e., perforated with tubes as shown in Figure 1C). For this, we looked at the effect of the auxetic structure on the dynamic behavior in the frequency domain of the meta-aerogels in comparison with regular PIR−PUR aerogels in a deep rubbery state (at 50 °C, i.e., well above Tg) where the short-range interactions of the polymer chains are vanishing. Accordingly, the viscoelastic properties of the PIR−PUR aerogel and the meta-aerogel samples were measured in the compression mode using Dynamic Mechanical Analysis (DMA) carried out with an Instron ElectroPuls E10000 load frame equipped with an environmental chamber as described in the Experimental Section. Using the cyclic displacement control mode, the samples were tested at 1% compressive strain offset with 0.1% oscillatory strain amplitude at different frequencies. Figure 3 compares the viscoelastic properties of the PIR−PUR aerogels and of the meta-aerogel samples at different frequencies. Both samples were held at least for 45 min at the target temperature to reach equilibrium conditions, then the steady-state response (load) to the harmonic excitation (displacement) was measured. The general trends in storage moduli of both aerogel and meta-aerogel samples were similar. The storage modulus increased monotonically with frequency. However, meta-aerogel samples were much softer than the aerogel sample due to the inclusion of the macroscopic tubular voids (e.g., the low-frequency storage modulus of the meta-aerogel was an order of magnitude lower than the aerogel's corresponding value). On the other hand, the loss modulus of both samples was nonmonotonic with respect to frequency. This is in contrary to what is expected for

glassy polymers, in which, typically, the loss modulus decreases monotonically with increasing frequency. It is speculated that in their rubbery state (i.e., above T_g as the case is here), it is more likely to excite high frequency dissipative modes leading to the observed nonmonotonic behavior for the loss modulus spectrum.[66] The loss moduli of both the PIR−PUR aerogel and of the meta-aerogel converged at the high-frequency region (above 10 Hz). This behavior was only seen for the loss modulus, and therefore, the tan δ of the meta-aerogel surpassed the corresponding values for the regular aerogel sample. Such a structure-dependent dynamic behavior points to the need for further studies of the dynamic properties as a function of different meta-structure parameters such as wall thickness and pore size. Those studies fall beyond the scope of this report; however, it can be concluded safely that for the present comparison at the quasistatic frequency domain (frequency → 0), meta-aerogels and regular aerogels are equivalent materials.

At the end, after cyclic loading at 50 °C for approximately 2000 cycles, the meta-aerogel sample was scanned using a Nikon 225 kV X-ray microcomputed tomography (CT) system, in order to investigate the presence of any damage (e.g., development of cracks). No obvious defects were observed in the meta-structure, pointing to the durability and resilience of those samples under these loading conditions. Movie S1 in the original paper Supporting Information shows cross-sectional slices of the CT scanned volumetric image of the meta-aerogel sample.

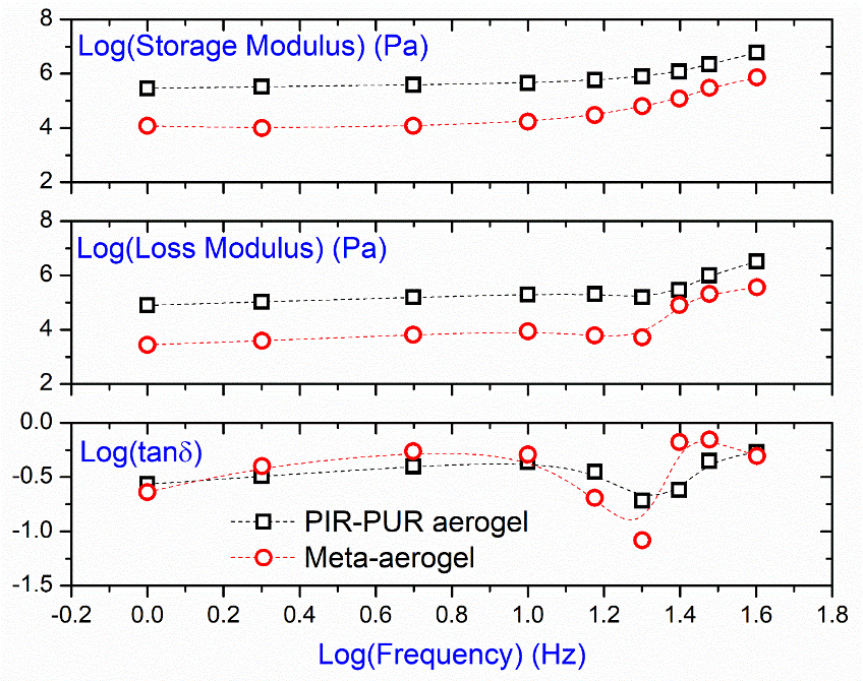

Figure 3. Viscoelastic properties in compression of straight and meta-aerogel PIR-PUR samples in their rubbery state (50 ^{o}C) as indicated.

2.4. AUXETIC BEHAVIOR SUPERIMPOSED WITH THE SHAPE-MEMORY EFFECT

Owing to the specific meta-structure design that was implemented in this work, the auxetic behavior of the resulting PIR−PUR meta-aerogels was visible only in compression. Thereby, the shape-memory characteristics of the meta-aerogel were recorded through a shape-memory thermomechanical cycle analogous to the one of Figure 2F but in the compression mode instead. Testing was carried out with the same Instron Electro-Puls E10000 load system used for the study of the viscoelastic properties in Section 2.3 and a preconditioned meta-aerogel sample, 58.21 mm × 30 mm × 25.4 mm in size, cut from a larger sample similar to the one shown in Figure 1C.

Thermomechanical data are shown in Figure 4A. T_{high} and T_{low} were set to 50 and 5 °C, respectively. In the beginning, the meta-aerogel sample was heated to 50 °C and was equilibrated for 15 min. Then, in Stage 1, the sample was compressed isothermally to −15% strain, showing a strong auxetic behavior exemplified by progressive contraction in the middle as strain increased (see Movie S2 in the original paper Supporting Information). Next, in Stage 2, the stress was kept constant while the temperature was lowered to T_{low} and the sample was equilibrated at that temperature for 30 min. In Stage 3, the meta-aerogel was unloaded, and could remain in the laterally contracted auxetic shape indefinitely (see the first frame on the top of Figure 4B). Finally, in Stage 4 the sample was heated back to Thigh (0.5 °C s^{-1}). Movie S3 of in the original paper Supporting Information shows the recovery of the meta-aerogel from the programmed auxetic shape at −15 % strain to its undeformed configuration at T_{high} = 50 °C. Snapshots of the meta-aerogel during Stage 4 were taken every 5 s, and were used to record the strain during shape recovery. Selected such snapshots during strain recovery are shown in Figure 4B.

The quality of the shape-memory effect of the meta-aerogel was evaluated via the same figures of merit used for the evaluation of that effect in the regular (not auxetic) PIR−PUR aerogels (see Section 2.2). Data analysis used to evaluate these figures of merit for the meta-aerogel are included in Figure 3, and values are listed in Table 2 of Appendix A. The strain fixity ratio of the meta-aerogel (99.3%) was practically equal to that of the regular PIR−PUR aerogels.

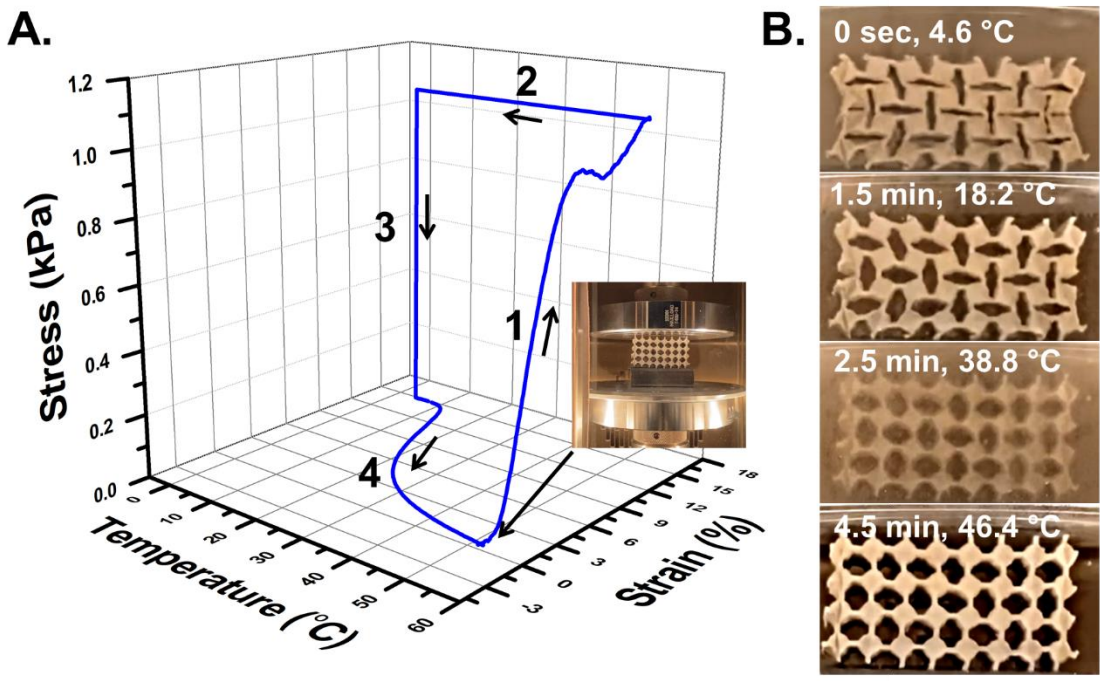

Figure 4. (A) A thermomechanical cycle of a preconditioned meta-aerogel sample. Stage 1: compression to -15% strain at the deformation temperature T_{high} = 50 °C; Stage 2: cooling under stress to fixing temperature T_{low} = 5 °C; Stage 3: stress release at T_{low}; and, Stage 4: shape recovery by heating at 0.5 °C/s back to T_{high}. Inset: experimental set up at the beginning of the cycle. (B) Snapshots along shape recovery (Stage 4).

However, both the strain recovery ratio (~98%) and the strain recovery rate (~15 min^{-1}) of the meta-aerogel were found to be significantly higher than the values calculated for the regular PIR−PUR aerogels (~80% and 5 min^{-1} , respectively), which is reflected in a higher value for the overall figure of merit: fill factor of the meta-aerogel = 0.69, versus 0.59 for the regular PIR−PUR aerogels. From another perspective though, upon closer inspection of the strain recovery versus temperature plots of Figure 4, parts C and D, of the regular versus the meta-aerogels, respectively, one notices that the recovery of the meta-aerogel starts at about 11−12 °C, that is well below the glass transition temperature of the PIR−PUR material, while the regular aerogel samples start recovering

their shape at the vicinity of their glass transition temperature. Furthermore, interestingly, at that lower-temperature range where meta-aerogels start recovering their shape, the strain values move rapidly through the range: (a) in which there is a hump in the stress−strain curve during isothermal compression in Stage 1 (that hump is pointed at with a yellow arrow in Figure 4A) (b) that roughly corresponds to the strain range where all tubes have collapsed under compression (refer to Movie S2 in the original paper Supporting Information). Therefore, the early onset of the meta-aerogel shape recovery must be linked to the meta-structure. In that regard, it is reasonable to assume that at low-temperatures both the short- and the long-range interactions between the polymeric segments are at their lowest energy states. According to the data then, short-range polymeric interactions, which are involved primarily in the material's intrinsic shape memory capability, are activated at higher temperatures−closer to T_g. On the other hand, however, long-range polymer interactions must be activated at temperatures well below the glass transition temperature. During the shape-recovery stage of the meta-aerogels, the long-range polymer interactions are activated first, turning the meta-aerogel from a stress-free state into a stressed one. Thereby the initial recovery is due to the fact that the meta-aerogel sample is first releasing its elastic energy stored in the meta-structure (post hump in Figure 4A), and thus, it reaches a new stress-free state similar to that in the regular PIR−PUR aerogels. By further increasing the temperature, the short-range interactions are coming into play, and finally the meta-aerogel recovers its original shape. Clearly, the initial low-temperature/high-strain spring-back effect in the meta-aerogel recovery process does not exist in the regular PIR−PUR aerogels.

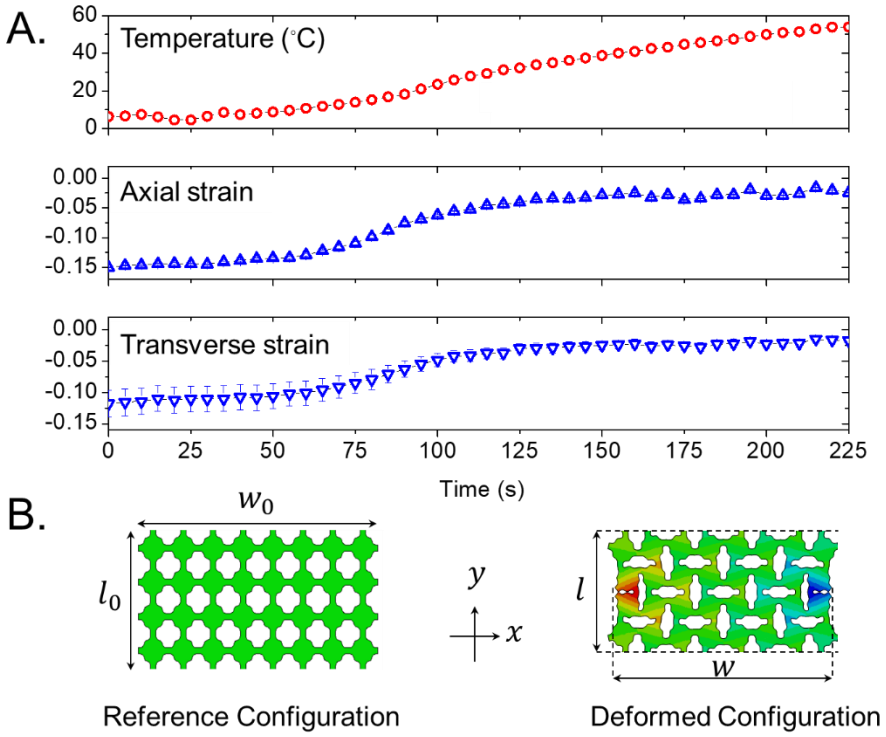

Figure 5. (A) Temperature, axial strain, and transverse strain as a function of time during the last stage (Stage 4) of the shape-memory thermomechanical cycle of Figure 4A; (B) Reference and deformed configurations of the meta-aerogel, and definitions relevant to the determination of the Poisson's ratio (see text).

In terms of quantifying the auxetic effect, at first, Figure 5A takes a closer look at the temperature stimulus applied to the meta-aerogel along with the axial and transverse strains of the meta-aerogel as a function of time during the last stage (Stage 4) of the thermomechanical cycle of Figure 4A. In reference to Figure 5B, the axial strain (ε_y) is defined as $\varepsilon_y = (l - l_0)/l_0$, and the transverse strain (ε_x) is given by $\varepsilon_x = (w - w_0)/w_0$. It is noted that these strain definitions are global and different from their corresponding values at local material points. The axial strain history follows the temperature stimulus almost precisely, thus showing that meta-aerogels are very responsive, which is important for applications in actuation.

Following our global definitions for the axial and transverse strains, the Poisson's ratio then becomes $\nu = -\varepsilon_x/\varepsilon_y$. Figure 6A shows the Poisson's ratio of the meta-aerogel sample as a function of the axial strain during the initial isothermal compression stage at 50 °C (Stage 1) as well as during the shape recovery stage (Stage 4). During Stage 1, the Poisson ratio shows a sigmoidal decay from a value slightly above zero (Poisson's ratio of about 0.05 at strains less than −1%) to a Poisson ratio of approximately −0.8 at −15% compressive axial strain. However, during the shape recovery stage (Stage 4), the Poisson ratio of the meta-aerogel did not recover to a positive value. This is related to the residual strain due to rearrangement of the H-bonding relationships within the PIR−PUR aerogels as discussed in conjunction with the settling observed between the first and the subsequent cycles of the shape-memory experiment of Figure 2F.[40] For reference, the Poisson ratio of the meta-aerogel as a function of temperature during Stage 4 is shown in Figure 6B.

Finally, the fact that the auxetic effect of meta-aerogels originates from their molded meta-structures was further supported by comparing the experimental Poisson's ratio results during Stage 1 (Figure 6A) with simulation results obtained from a 2D linearly elastic finite element method (FEM) using the commercially available finite element code ABAQUS. The effect of viscoelastic properties on Poisson's ratio was not considered in these simulations, thus leaving only the tubes as the only relevant parameter for the auxetic effect. Figure 7 compares the evolution of the experimental and numerical Poisson's ratios as a function of compressive strain.

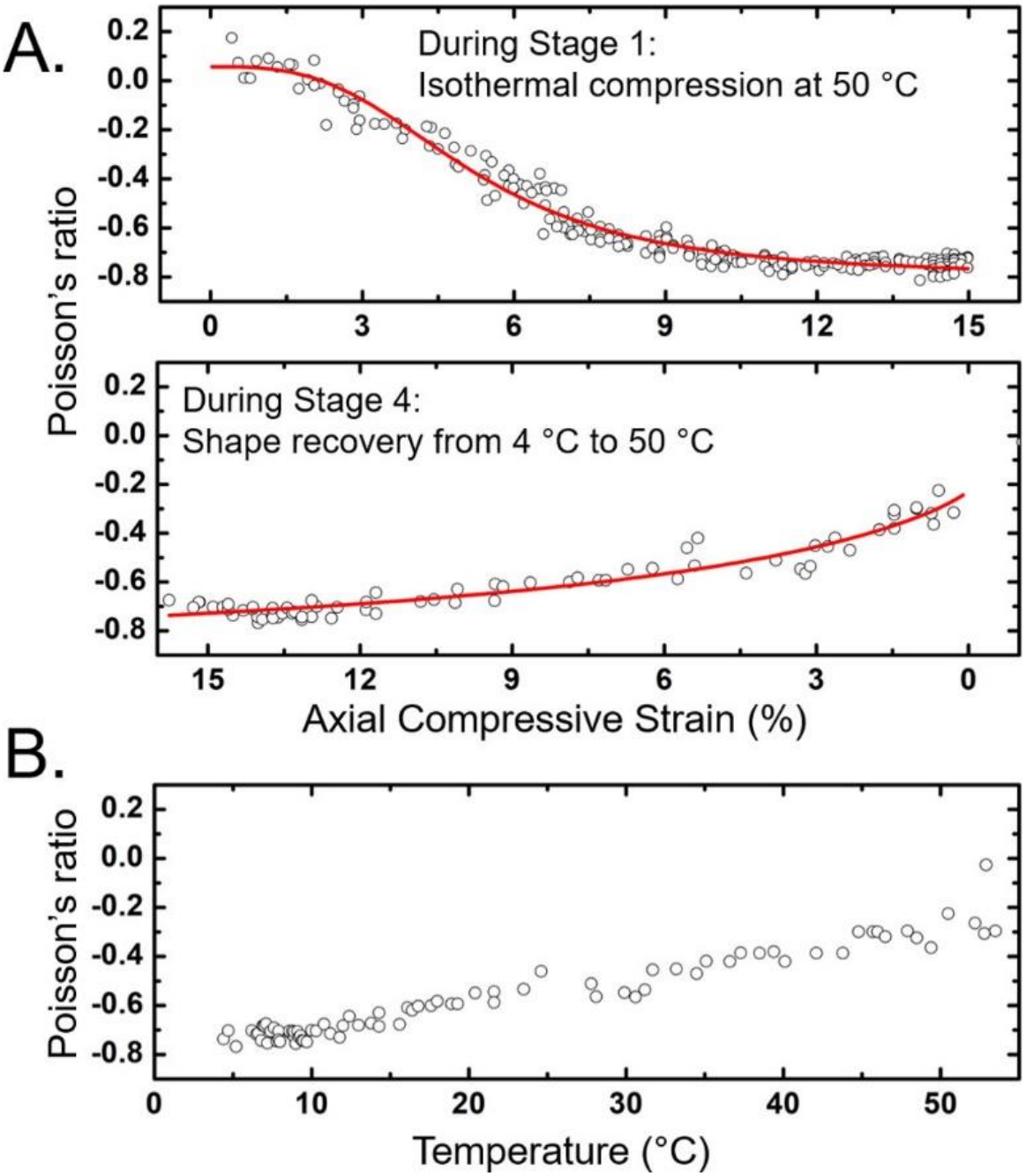

Figure 6. (A) Poisson's ratio of the meta-aerogel sample as a function of compressive axial strain during Stage 1 and Stage 4 of the shape-memory thermomechanical cycle. The solid red line is the best-fit curve. (B) Poisson's ratio of the meta-aerogel sample as a function of temperature during Stage 4 of the shape-memory thermomechanical cycle of Figure 4A.

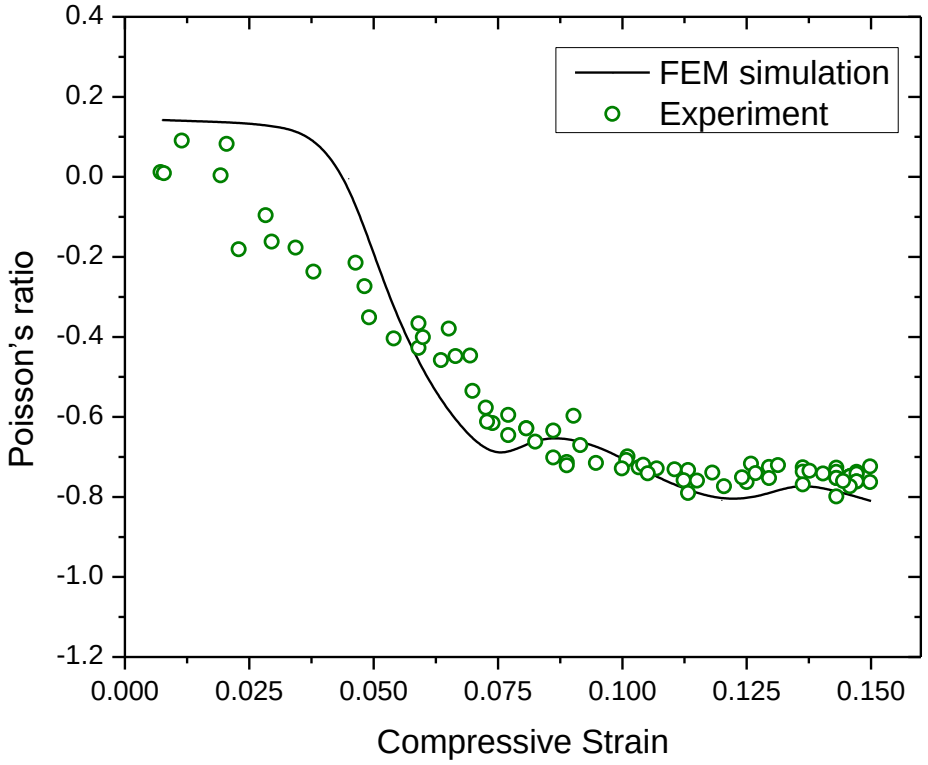

Figure 7. Experimental versus simulated results for the evolution of Poisson's ratio of meta-aerogels as a function of compressive strain.

Despite the lack of any viscoelastic material property considerations, the FEM simulation predicted the experimental results well; in fact, at high strains, i.e., where the auxetic effect is most relevant, the FEM simulations and the experimental results were in excellent agreement. Small deviations between the experimental and simulation results were observed at small strains (less than 0.05). The simulations assume a perfect geometry, but in practice, the presence of small defects introduced during manufacturing process could potentially cause the slight discrepancies. However, their consistent trend at low strains and perfect matching at high strains clearly indicate the major role of the meta-structure on the global behavior of the meta-aerogels.

3. CONCLUSION

Meta-aerogels combine a negative Poisson ratio with a thermos-responsive shape-memory effect, and they are potentially important materials for commercial, aeronautical, and aerospace applications. Upon cooling well below T_g, meta-aerogels maintain the auxetic shape at their shrunk/negative Poisson's ratio state that was imposed on them by compression at a temperature above T_g, and upon heating back above T_g they recover their original configuration. The particular aerogel material that was used for demonstrating those effects was based on a highly cross-linked poly(isocyanurate urethane) polymeric backbone, and the auxetic form was achieved with parallel tubular voids running the length of a macroscopic block of a standard aerogel of that material. The Poisson's ratio reached −0.8 at −15% compressive strain. The shape recovery of those meta-aerogels traced a temperature increase as fast as 0.5 °C/s. These materials comprise a good platform for further exploration of applications of additive manufacturing through molding techniques in the fabrication of functional aerogels. In terms of possible future designs, exploration of tubes with different cross-sectional shapes is a possible route for further study, while totally different 3D designs of shape-memory aerogels perforated with multidimensional tube designs are also possible candidates for further investigation.

4. MATERIALS AND METHODS

4.1. MATERIALS

All materials were commercially sourced and used without further processing. Desmodur N3300A triisocyanate was generously donated in pure form by Covestro LLC (Pittsburgh, PA). Triethylene glycol (TEG), anhydrous acetonitrile, and anhydrous CuCl2 were purchased from Fisher Scientific (Hampton, NH).

4.2. SYNTHESIS OF PIR-PUR REGULAR AND META-AEROGELS

In a typical synthetic procedure, 30 mmol of Desmodur N3300A and 45 mmol of TEG were dissolved in 207.80 mL of anhydrous acetonitrile (refer to Table 1 of Appendix A). The solution was stirred for 10 min at room temperature. A catalyst stock solution was prepared by dissolving 2.789 g of anhydrous $CuCl_2$ in 250 mL of acetonitrile. Then, 5.6 mL of the catalyst stock solution was added to the reaction mixture. The resulting solution was stirred for another 5 min and was poured into the appropriate molds. For regular aerogels the molds were 25 mL plastic vials. For the meta-aerogels, the design of the molds is described in Figures 1 and 2 of the Supporting Information. The meta-aerogel mold design was the negative of the desirable meta-aerogel structure, and it was submitted in the STL (Standard Triangle Language) format to 3D Hubs, an online manufacturing platform 67 to be 3D printed with poly(lactic acid) (PLA) with 100 μm resolution and 30% infill percentage. The spikes of the mold protruded out and were an integral part of a PLA base that eventually played the role of the bottom of the gelation container. The mold was completed by wrapping the outer

spikes around with aluminum tape. The entire inner surface of the mold was sprayed with a mold release spray (Sprayon MR311, Cleveland, OH). Wet gels were aged inside the molds for 1.5 h. After aging, wet gels were removed from the molds and were washed with anhydrous acetone (4 times, 24 h each time), and finally they were washed with pentane (4 times, 24 h each time). In our current two-dimensional meta-aerogel design as shown in Figure 2.1, wet-gels were removed from their molds by lifting the bottom side of the wet-gel and unplugging it from the mold. The amount of solvent used for each washing step was equal to four times the volume of the wet gel. Pentane-washed wet gels were dried under ambient conditions for 24 h. Drying was considered complete after placing the samples in an oven at 40 °C for 3 h.

4.3. CHEMICAL CHARACTERIZATION

Attenuated total reflectance (ATR) FTIR spectroscopy was carried out with a Thermo Scientific Nicolet iS50 FT-IR, equipped with an ATR accessory. Samples were cut to the size of the opening of ATR diamond crystal, and ATR-FTIR spectra were obtained by pressing them against the crystal with the ATR unit's pressure device (gripper). Solid-state CPMAS ^{13}C NMR spectra were obtained with powdered samples on a Bruker Avance III 400 MHz spectrometer with a carbon frequency of 100 MHz using a 7 mm Bruker MAS probe at a magic angle spinning rate of 5 kHz, with broadband proton suppression, and the CP TOSS pulse sequence. The total suppression of spinning sidebands (TOSS) pulse sequence was applied by using a series of four properly timed 180° pulses on the carbon channel at different points of a cycle before acquisition of the FID, after an initial excitation with a 90° pulse on the proton channel. The 90° excitation

pulse on the proton and the 180° excitation pulse on carbon were set to 4.2 and 10 μs, respectively. A contact time of 3 μs was used for cross-polarization. Solid-state ^{13}C NMR spectra were referenced externally to glycine (carbonyl carbon at 176.03 ppm). Chemical shifts are reported versus TMS (0 ppm).

4.4. PHYSICAL CHARACTERIZATION

Bulk densities (ρ_b) were determined from the weight and the physical dimensions of the samples. Skeletal densities (ρ_s) were determined with helium pycnometer using a Micromeritics AccuPyc II 1340 instrument. Porosities (Π) as a percent of empty space were determined from the ρb and ρs values via $\Pi = 100 \times [(\rho_s - \rho_b)/\rho_s]$.

Scanning electron microscopy (SEM) was conducted with Au/Pd (60/40) coated samples on a Hitachi Model S-4700 field emission microscope. The sample was placed on the stub with C-dot. Thin sticky Cu stripes were cut and placed on the edges and top of the sample leaving a small area uncovered for observation.

Microcomputed tomography scans were carried out using a Nikon Microfocus 225 kV X-ray source. The effective pixel resolution was 50 μm/pixel. The X-ray projection images were obtained through rotating the frame around the center of the sample, and using the Nikon computer software, these projection images were converted into a 3D object. The 3D object was later sliced using the free academic-licensed software Dragonfly to reveal the internal structure of the sample.

4.5. THERMOMECHANICAL CHARACTERIZATION

The glass-transition temperature (T_g) of the PIR−PUR aerogel material was determined using a TA Instruments Q800 dynamic mechanical analyzer (DMA) in the tension mode performing a dynamic ramp at 1 Hz from −150 to +150 °C at 3 °C min^{-1} . Thermomechanical cycling of regular PIR−PUR aerogels was conducted under tension using the same DMA instrument in the controlled-force mode as follows: samples were equilibrated at their deformation temperature (T_{high} = 40 °C) for 5 min. Then they were stretched with a small tensile force (0.01 N), and the length of the sample was measured by the instrument and stored. Next, specimens were stretched at a constant force rate of 1 N min^{-1} up to near their break point (typically around 60% strain), and then, while under the final stress, they were cooled at 5 °C min^{-1} to the fixation temperature (T_{low} = −10 °C ≪ T_g). Samples were equilibrated at T_{low} for 5 min, and the tensile force was reduced to 0.01 N. Samples were allowed to relax (fix) for 15 min (always while at T_{low}) while strain was recorded. Finally, samples were heated at 1 °C min^{-1} to their recovery temperature (T_{high} = 40 °C) while strain was still recorded. Samples were held at T_{high} for 15 min, and the cycle was repeated. Five such cycles were run successively for each sample.

Thermomechanical cycling of auxetic meta-aerogels (nominal size of 58.21 mm × 30 mm × 25.4 mm) was performed in the compression mode on an Instron mechanical testing system (Instron Inc., Electropuls E10000 load frame, Norwood, MA) equipped with a 500 N load cell (with an accuracy of 0.5% of the reading), and an Instron Environmental Chamber (Instron, Inc., Model 5969, Norwood, MA). During the first and last step (Figure 2.4A, Stages 1 and 4), the sample was monitored continuously with a Nikon camera (Model D7100) kept at a fixed position normal to the sample (see Movies

S2 and S3, original paper supporting information). During Stage 4, the camera was also recording simultaneously the temperature of the sample by placing the display of our thermal couple next to the Environmental Chamber (see Movie S3). The bottom part of Figure 2.4A (strain versus temperature during shape recovery) was constructed by taking a series of digital images every 5 s from Movie S3 like those shown in Figure 2.4B. The images were analyzed using the open-source image-processing package, ImageJ. For this, the total absolute area of the holes was measured in each digital image, and was divided by the total area of the holes before any compression (from Movie S2 of original paper supporting information). The strain at each time interval/temperature was set equal to the square root of each area ratio. Poisson's ratios were also measured from the digital images using ImageJ by comparing the dimensions of the sample at different stages of deformation with corresponding values for the undeformed sample before compression (see Figure 2.5B). Samples were equilibrated at each target temperature for at least 15 min before moving to the next step. Deep rubbery state DMA measurements in compression were also performed using the same Instron Electropuls E10000 load frame. Cylindrical samples (with nominal outer diameter of 1 cm as well as length of 1 cm) were also equilibrated at each target temperature for at least 45 min before the experiment. In a compression control mode, the steady state response (load) to the harmonic excitation (displacement) was measured. At least 50 cycles were considered at each frequency.

4.6. FINITE ELEMENT ANALYSIS

The topological behavior of the meta-structure was simulated using a 2D linearly elastic finite element formulation by means of the commercial package Abaqus/Standard 6.14 (Dassault Systems). For this purpose, a 2D computational model at similar dimensions of the experimental sample was constructed. Under a displacement control simulation, the bottom of the model was fixed (encastré boundary condition), and the model was subjected to a compressive displacement from the top side. No friction was considered between the loading frame and the top side of the model. The model was compressed up to 15% compressive axial strain.

REFERENCES

[1] Liu, C.; Qin, H.; Mather, P. T. Review of Progress in Shape-Memory Polymers. *J. Mater. Chem.* **2007**, *17*, 1543−1558.

[2] Lendlein, A.; Jiang, H.; Jünger, O.; Langer, R. Light-Induced Shape-Memory Polymers. *Nature* **2005**, *434*, 879−882.

[3] Huang, W. M.; Yang, B.; An, L.; Li, C.; Chan, Y. S. Water-Driven Programmable Polyurethane Shape Memory Polymer: Demonstration and Mechanism. *Appl. Phys. Lett.* **2005**, *86*, 114105.

[4] Han, X.-J.; Dong, Z.-Q.; Fan, M.-M.; Liu, Y.; Li, J.-H.; Wang, Y.- F.; Yuan, Q.-J.; Li, B.-J.; Zhang, S. PH-Induced Shape-Memory Polymers. *Macromol. Rapid Commun.* **2012**, *33*, 1055−1060.

[5] Mohr, R.; Kratz, K.; Weigel, T.; Lucka-Gabor, M.; Moneke, M.; Lendlein, A. Initiation of Shape-Memory Effect by Inductive Heating of Magnetic Nanoparticles in Thermoplastic Polymers. *Proc. Natl. Acad. Sci. U. S. A.* **2006**, *103*, 3540−3545.

[6] Cianchetti, M.; Laschi, C.; Menciassi, A.; Dario, P. Biomedical Applications of Soft Robotics. *Nat. Rev. Mater.* **2018**, *3*, 143− 153.

[7] Roche, E. T.; Horvath, M. A.; Wamala, I.; Alazmani, A.; Song, S. E.; Whyte, W.; Machaidze, Z.; Payne, C. J.; Weaver, J. C.; Fishbein, G.; Kuebler, J.; Vasilyev, N. V.; Mooney, D. J.; Pigula, F. A.; Walsh, C. J. Soft Robotic Sleeve Supports Heart Function. *Sci. Transl. Med.* **2017**, *9*, 3925.

[8] Yu, X.; Xie, Z.; Yu, Y.; Lee, J.; Vazquez-Guardado, A.; Luan, H.; Ruban, J.; Ning, X.; Akhtar, A.; Li, D.; Ji, B.; Liu, Y.; Sun, R.; Cao, J.; Huo, Q.; Zhong, Y.; Lee, C. M.; Kim, S. Y.; Gutruf, P.; Zhang, C.; Xue, Y.; Guo, Q.; Chempakasseril, A.; Tian, P.; Lu, W.; Jeong, J. Y.; Yu, Y. J.; Cornman, J.; Tan, C. S.; Kim, B. H.; Lee, K. H.; Feng, X.; Huang, Y.; Rogers, J. A. Skin-Integrated Wireless Haptic Interfaces for Virtual and Augmented Reality. *Nature* **2019**, *575*, 473−479.

[9] Kanik, M.; Orguc, S.; Varnavides, G.; Kim, J.; Benavides, T.; Gonzalez, D.; Akintilo, T.; Cem Tasan, C.; Chandrakasan, A. P.; Fink, Y.; Anikeeva, P. Strain-Programmable Fiber-Based Artificial Muscle. *Science* **2019**, *365*, 145−150.

[10] Alapan, Y.; Karacakol, A. C.; Guzelhan, S. N.; Isik, I.; Sitti, M. Reprogrammable Shape Morphing of Magnetic Soft Machines. *Sci. Adv.* **2020**, *6*, 6414−6432.

[11] Liu, J. A. C.; Gillen, J. H.; Mishra, S. R.; Evans, B. A.; Tracy, J. B. Photothermally and Magnetically Controlled Reconfiguration of Polymer Composites for Soft Robotics. *Sci. Adv.* **2019**, *5*, 2897.

[12] Hartl, D. J.; Lagoudas, D. C. Aerospace Applications of Shape Memory Alloys. *Proc. Inst. Mech. Eng., Part G* **2007**, *221*, 535− 552.

[13] Santo, L.; Quadrini, F.; Accettura, A.; Villadei, W. Shape Memory Composites for Self-Deployable Structures in Aerospace Applications. *Procedia Eng.* **2014**, *88*, 42−47.

[14] Gall, K.; Yakacki, C. M.; Liu, Y.; Shandas, R.; Willett, N.; Anseth, K. S. Thermomechanics of the Shape Memory Effect in Polymers for Biomedical Applications. *J. Biomed. Mater. Res., Part A* **2005**, *73*, 339−348.

[15] Safranski, D. L.; Smith, K. E.; Gall, K. Mechanical Requirements of Shape-Memory Polymers in Biomedical Devices. *Polym. Rev.* **2013**, *53*, 76−91.

[16] Hearon, K.; Wierzbicki, M. A.; Nash, L. D.; Landsman, T. L.; Laramy, C.; Lonnecker, A. T.; Gibbons, M. C.; Ur, S.; Cardinal, K. O.; Wilson, T. S.; Wooley, K. L.; Maitland, D. J. A Processable Shape Memory Polymer System for Biomedical Applications. *Adv. Healthcare Mater.* **2015**, *4*, 1386−1398.

[17] Soutis, C.; Irving, P. *Polymer Composites in the Aerospace Industry*; Elsevier Inc., 2014; DOI: 10.1016/C2013-0-16303-9. (18) Lendlein, A.; Gould, O. E. C. Reprogrammable Recovery and Actuation Behaviour of Shape-Memory Polymers. *Nat. Rev. Mater.* **2019**, *4*, 116−133.

[18] Behl, M.; Kratz, K.; Zotzmann, J.; Nöchel, U.; Lendlein, A. Reversible Bidirectional Shape-Memory Polymers. *Adv. Mater.* **2013**, *25*, 4466−4469.

[19] Pierre, A. C. History of Aerogels. In *Aerogels Handbook*; Springer New York: New York, 2011; pp 3−18; DOI: 10.1007/978- 1-4419-7589-8_1.

[20] Koebel, M. M.; Rigacci, A.; Achard, P. Aerogels for Superinsulation: A Synoptic View. In *Aerogels Handbook*; Springer New York: New York, 2011; pp 607−633; DOI: 10.1007/978-1- 4419-7589-8_26.

[21] Lee, J. K.; Gould, G. L.; Rhine, W. Polyurea Based Aerogel for a High Performance Thermal Insulation Material. *J. Sol-Gel Sci. Technol.* **2009**, *49*, 209−220.

[22] Pierre, A. C.; Rigacci, A. SiO2 Aerogels. In *Aerogels Handbook*; Springer New York: New York, 2011; pp 21−45; DOI: 10.1007/978- 1-4419-7589-8_2.

[23] Mandal, C.; Donthula, S.; Rewatkar, P. M.; Sotiriou-Leventis, C.; Leventis, N. Experimental Deconvolution of Depressurization from Capillary Shrinkage during Drying of Silica Wet-Gels with SCF CO_2 Why Aerogels Shrink? *J. Sol-Gel Sci. Technol.* **2019**, *92*, 662− 680.

[24] Leventis, N.; Lu, H. Polymer-Crosslinked Aerogels. In *Aerogels Handbook*; Springer New York: New York, 2011; pp 251−285; DOI: 10.1007/978-1-4419-7589-8_13.

[25] Leventis, N.; Sotiriou-Leventis, C.; Zhang, G.; Rawashdeh, A. M. M. Nanoengineering Strong Silica Aerogels. *Nano Lett.* **2002**, *2*, 957−960.

[26] Leventis, N. Three-Dimensional Core-Shell Superstructures: Mechanically Strong Aerogels. *Acc. Chem. Res.* **2007**, *40*, 874−884.

[27] Mandal, C.; Donthula, S.; Far, H. M.; Saeed, A. M.; SotiriouLeventis, C.; Leventis, N. Transparent, Mechanically Strong, Thermally Insulating Cross-Linked Silica Aerogels for Energy Efficient Windows. *J. Sol-Gel Sci. Technol.* **2019**, *92*, 84−100.

[28] Meador, M. A. B. Improving Elastic Properties of Polymer Reinforced Aerogels. In *Aerogels Handbook*; Springer New York: New York, 2011; pp 315−334; DOI: 10.1007/978-1-4419-7589-8_15.

[29] Meador, M. A. B.; Capadona, L. A.; McCorkle, L.; Papadopoulos, D. S.; Leventis, N. Structure-Property Relationships in Porous 3D Nanostructures as a Function of Preparation Conditions: Isocyanate Cross-Linked Silica Aerogels. *Chem. Mater.* **2007**, *19*, 2247−2260.

[30] Lu, H.; Luo, H.; Leventis, N. Mechanical Characterization of Aerogels. In *Aerogels Handbook*; Springer New York: New York, 2011; pp 499−535. DOI: 10.1007/978-1-4419-7589-8_22.

[31] Sadekar, A. G.; Mahadik, S. S.; Bang, A. N.; Larimore, Z. J.; Wisner, C. A.; Bertino, M. F.; Kalkan, A. K.; Mang, J. T.; SotiriouLeventis, C.; Leventis, N. From 'Green' Aerogels to Porous Graphite by Emulsion Gelation of Acrylonitrile. *Chem. Mater.* **2012**, *24*, 26−47.

[32] Malakooti, S.; Qin, G.; Mandal, C.; Soni, R.; Taghvaee, T.; Ren, Y.; Chen, H.; Tsao, N.; Shiao, J.; Kulkarni, S. S.; Sotiriou-Leventis, C.; Leventis, N.; Lu, H. Low-Cost, Ambient-Dried, Superhydrophobic, High Strength, Thermally Insulating, and Thermally Resilient Polybenzoxazine Aerogels. *ACS Appl. Polym. Mater.* **2019**, *1*, 2322−2333.

[33] Mahadik-Khanolkar, S.; Donthula, S.; SotiriouLeventis, C.; Leventis, N. Polybenzoxazine Aerogels. 1. High-Yield Room-Temperature Acid-Catalyzed Synthesis of Robust Monoliths, Oxidative Aromatization, and Conversion to Microporous Carbons. *Chem. Mater.* **2014**, *26*, 1303−1317.

[34] Mulik, S.; SotiriouLeventis, C.; Leventis, L. N. Time-Efficient Acid-Catalyzed Synthesis of Resorcinol-Formaldehyde Aerogels. *Chem. Mater.* **2007**, *19*, 6138−6144.

[35] Meador, M. A. B.; Malow, E. J.; Silva, R.; Wright, S.; Quade, D.; Vivod, S. L.; Guo, H.; Guo, J.; Cakmak, M. Mechanically Strong, Flexible Polyimide Aerogels Cross-Linked with Aromatic Triamine. *ACS Appl. Mater. Interfaces* **2012**, *4*, 536−544.

[36] Guo, H.; Meador, M. A. B.; McCorkle, L.; Quade, D. J.; Guo, J.; Hamilton, B.; Cakmak, M.; Sprowl, G. Polyimide Aerogels Cross-Linked through Amine Functionalized Polyoligomeric Silsesquioxane. *ACS Appl. Mater. Interfaces* **2011**, *3*, 546−552.

[37] Taghvaee, T.; Donthula, S.; Rewatkar, P. M.; Majedi Far, H.; Sotiriou-Leventis, C.; Leventis, N. K -Index: A Descriptor, Predictor, and Correlator of Complex Nanomorphology to Other Material Properties. *ACS Nano* **2019**, *13*, 3677−3690.

[38] Bang, A.; Buback, C.; Sotiriou-Leventis, C.; Leventis, N. Flexible Aerogels from Hyperbranched Polyurethanes: Probing the Role of Molecular Rigidity with Poly(Urethane Acrylates) Versus Poly(Urethane Norbornenes). *Chem. Mater.* **2014**, *26*, 6979− 6993.

[39] Chidambareswarapattar, C.; McCarver, P. M.; Luo, H.; Lu, H.; Sotiriou-Leventis, C.; Leventis, N. Fractal Multiscale Nanoporous Polyurethanes: Flexible to Extremely Rigid Aerogels from Multifunctional Small Molecules. *Chem. Mater.* **2013**, *25*, 3205−3224.

[40] Kanellou, A.; Anyfantis, G.; Chriti, D.; Raptopoulos, G.; Pitsikalis, M.; Paraskevopoulou, P. Poly(Urethane-Norbornene) Aerogels via Ring Opening Metathesis Polymerization of Dendritic Urethane-Norbornene Monomers: Structure-Property Relationships as a Function of an Aliphatic Versus an Aromatic Core and the Number of Peripheral Norbornene Moieties. *Molecules* **2018**, *23*, 1007.

[41] Donthula, S.; Mandal, C.; Leventis, T.; Schisler, J.; Saeed, A. M.; Sotiriou-Leventis, C.; Leventis, N. Shape Memory Superelastic Poly(Isocyanurate-Urethane) Aerogels (PIR-PUR) for Deployable Panels and Biomimetic Applications. *Chem. Mater.* **2017**, *29*, 4461−4477.

[42] Donthula, S.; Mandal, C.; Schisler, J.; Leventis, T.; Meador, M. A. B.; Sotiriou-Leventis, C.; Leventis, N. Nanostructure-Dependent Marcus-Type Correlation of the Shape Recovery Rate and the Young's Modulus in Shape Memory Polymer Aerogels. *ACS Appl. Mater. Interfaces* **2018**, *10*, 23321−23334.

[43] Malakooti, S.; Rostami, S.; Churu, H. G.; Luo, H.; Clark, J.; Casarez, F.; Rettenmaier, O.; Daryadel, S.; Minary-Jolandan, M.; Sotiriou-Leventis, C.; Leventis, N.; Lu, H. Scalable, Hydrophobic and Highly-Stretchable Poly(Isocyanurate-Urethane) Aerogels. *RSC Adv.* **2018**, *8*, 21214−21223.

[44] Bertoldi, K.; Vitelli, V.; Christensen, J.; Van Hecke, M. Flexible Mechanical Metamaterials. *Nat. Rev. Mater.* **2017**, *2*, 1−11.

[45] Zheng, X.; Lee, H.; Weisgraber, T. H.; Shusteff, M.; DeOtte, J.; Duoss, E. B.; Kuntz, J. D.; Biener, M. M.; Ge, Q.; Jackson, J. A.; Kucheyev, S. O.; Fang, N. X.; Spadaccini, C. M. Ultralight, Ultra stiff Mechanical Metamaterials. *Science* **2014**, *344*, 1373−1377.

[46] Lakes, R. S. Negative-Poisson's-Ratio Materials: Auxetic Solids. Annu. Rev. Mater. Res. 2017, 47, 63−81. (46) Evans, K. E.; Alderson, A. Auxetic Materials: Functional Materials and Structures from Lateral Thinking! Adv. Mater. 2000, 12 (9), 617−628.

[47] Liu, Q. Literature Review: Materials with Negative Poisson's Ratios and Potential Applications to Aerospace and Defense; Defence Science and Technology Organization: 2006; ADA460791.

[48] Li, T.; Chen, Y.; Hu, X.; Li, Y.; Wang, L. Exploiting Negative Poisson's Ratio to Design 3D-Printed Composites with Enhanced Mechanical Properties. *Mater. Des.* **2018**, *142*, 247−258.

[49] Overvelde, J. T. B.; Shan, S.; Bertoldi, K. Compaction through Buckling in 2D Periodic, Soft and Porous Structures: Effect of Pore Shape. *Adv. Mater.* **2012**, *24*, 2337−2342.

[50] Babaee, S.; Shim, J.; Weaver, J. C.; Chen, E. R.; Patel, N.; Bertoldi, K. 3D Soft Metamaterials with Negative Poisson's Ratio. *Adv. Mater.* **2013**, *25*, 5044−5049.

[51] SOLIDWORKS 3D CAD | SOLIDWORKS https://www.solidworks.com/product/solidworks-3d-cad (accessed May 4, 2021).

[52] Choong, Y. Y. C.; Tan, H. W.; Patel, D. C.; Choong, W. T. N.; Chen, C. H.; Low, H. Y.; Tan, M. J.; Patel, C. D.; Chua, C. K. The Global Rise of 3D Printing during the COVID-19 Pandemic. *Nat. Rev. Mater.* **2020**, *5*, 637−639.

[53] Chua, C. K.; Leong, K. F. *3D Printing and Additive Manufacturing: Principles and Applications: The 5th ed. of Rapid Prototyping: Principles and Applications*; World Scientific Publishing Co., 2017; DOI: 10.1142/10200.

[54] Zhu, C.; Han, T. Y. J.; Duoss, E. B.; Golobic, A. M.; Kuntz, J. D.; Spadaccini, C. M.; Worsley, M. A. Highly Compressible 3D Periodic Graphene Aerogel Microlattices. *Nat. Commun.* **2015**, *6*, 1−8.

[55] Zhang, Q.; Zhang, F.; Medarametla, S. P.; Li, H.; Zhou, C.; Lin, D. 3D Printing of Graphene Aerogels. *Small* **2016**, *12*, 1702− 1708.

[56] Saeed, S.; Al Soubaihi, R. M.; White, L. S.; Bertino, M. F.; Saoud, K. M. Rapid Fabrication of Cross-Linked Silica Aerogel by Laser Induced Gelation. *Microporous Mesoporous Mater.* **2016**, *221*, 245−252.

[57] Zhao, S.; Siqueira, G.; Drdova, S.; Norris, D.; Ubert, C.; Bonnin, A.; Galmarini, S.; Ganobjak, M.; Pan, Z.; Brunner, S.; Nyström, G.; Wang, J.; Koebel, M. M.; Malfait, W. J. Additive Manufacturing of Silica Aerogels. *Nature* **2020**, *584*, 387−392.

[58] Che, K.; Yuan, C.; Qi, H. J.; Meaud, J. Viscoelastic Multistable Architected Materials with Temperature-Dependent Snapping Sequence. *Soft Matter* **2018**, *14*, 2492.

[59] Joo, P.; Yao, Y.; Teo, N.; Jana, S. C. Modular Aerogel Brick Fabrication via 3D-Printed Molds. *Addit. Manuf.* **2021**, *46*, 102059.

[60] Turner, B. N.; Strong, R.; Gold, S. A. A Review of Melt Extrusion Additive Manufacturing Processes: I. Process Design and Modeling. *Rapid Prototyp. J.* **2014**, *20*, 192−204.

[61] Tanikella, N. G.; Wittbrodt, B.; Pearce, J. M. Tensile Strength of Commercial Polymer Materials for Fused Filament Fabrication 3D Printing. *Addit. Manuf.* **2017**, *15*, 40−47.

[62] Defeyt, C.; Langenbacher, J.; Rivenc, R. Polyurethane Coatings Used in Twentieth Century Outdoor Painted Sculptures. Part I: Comparative Study of Various Systems by Means of ATR-FTIR Spectroscopy. *Heritage Sci.* **2017**, *5*, 11.

[63] Silverstein, R. M.; Webster, F. X.; Kiemle, D. J. *Spectrometric Identification of Organic Compounds*; John Wiley & Sons: 2005.

II. USING CATALYSIS TO CONTROL THE MORPHOLOGY AND STIFFNESS OF SHAPE-MEMORY POLY(ISOCYANURATE-URETHANE) (PIR-PUR) AEROGELS

A B M Shaheen ud Doulah, Chandana Mandal, Hojat M. Far, Vaibhav A. Edlabadkar, Rushi U. Soni, Stephen Y. Owusu, Nicholas Leventis, and Chariklia Sotiriou-Leventis*

Department of Mechanical and Aerospace Engineering, Missouri University of Science and Technology, Rolla, MO 65409

ABSTRACT

A large array of anhydrous metal ions were tested as catalysts in the preparation of shape-memory poly(isocyanurate-urethane) (PIR-PUR) aerogels from the reaction of 1,3,5-tris(6-isocyanatohexyl)-1,3,5-triazinane-2,4,6-trione (Desmodur N3300A: a well-known isocyanurate-based triisocyanate) and triethylene glycol (TEG) in anhydrous acetonitrile. The reaction yielded wet gels that were dried into aerogels with supercritical fluid CO_2 in an autoclave. Catalytic activity was mostly identified among CH_3CN-soluble salts (mainly chlorides) of third-row d-block elements from iron to zinc, group 13 elements from aluminum to thallium, as well as cadmium, bismuth and tin. Tin (^{119}Sn) NMR indicated that the metal ion complexes with TEG followed by reaction with the isocyanate. By using a fixed monomer concentration (20% w/w) and varying only the chemical identity and concentration of the catalysts it was possible to demonstrate that the micromorphology of the resulting aerogels depended only on the gelation time. That is, for equal gelation times, the morphology was approximately the same, irrespective of the catalyst. For short gelation times (around 5 min or less) the aerogel frameworks were bicontinuous, changing to small spheroidal at around 20 min and to large microspheres

for gelation times around 75 min or more. Having obtained practical control over micromorphology leaving other material properties such as density, and porosity unaffected, it was possible to demonstrate that bicontinuous structures of PIR-PUR aerogels can be up to 4 times stiffer and up to two times better thermal conductors than structures consisting of spheres. This finding was attributed to the different widths of the neck zones between particles, noting that in bicontinuous morphologies the neck diameters are almost equal to the particle diameters.

1. INTRODUCTION

A hard-to-miss property of aerogels derived from isocyanates,[1] including polymer-crosslinked aerogels,[2] and pristine polyurea,[3] polyurethane,[4] polyimide,[5] and polyamide aerogels[6] is their remarkable mechanical strength.[7] Amongst those materials, aliphatic polyurea aerogels obtained from the reaction of water with an isocyanate,[8] specifically a isocyanurate-based triisocyanate trimer of hexamethylene triisocyanate (Desmodur N3300A), demonstrate a quite broad array of nanostructures,[9,10,11] and a significant recent finding was that their mechanical properties not only depend on the nanostructure, but most importantly their strength is not a single-valued function of their nanomorphology.[11] It was speculated that the latter was determined mainly by the mode of the phase separation of the polymer:[12] Phase separation of solid nanoparticles gives nanoparticulate networks where individual nanoparticles may be either randomly distributed, or organized in caterpillar-like structures of various aspect ratios. On the other hand, if the developing polymer is phase-separated as a liquid that gets solidified

later, the morphology can be quite diverse, ranging from thin nanofilaments to small solid microspheres embedded in nanofibers, to larger solid microspheres with some fibers emanating from their surface. The appearance of those nano/micromorphologies showed a correlation with increasing gelation time, in the order just mentioned.[11]

Aliphatic polyurethane aerogels made with the same aliphatic triisocyanate as the polyureas above reacting with short aliphatic diol derivatives of ethylene glycol, display also diverse skeletal morphologies, yet quite different from those of polyurea.[13,14,15] The common morphological denominator with the corresponding polyureas can be considered the presence of large, albeit bald microspheres. A completely different structural feature in these aliphatic polyurethane aerogels, not observed in the corresponding polyurea, was the occasional appearance of bicontinuous morphologies in which the solid and porous networks looked fairly similar. It was proposed that all these microstructures arise from the phase separation of an immiscible liquid polymer followed by solidification at a later time.[12]

This type of aliphatic polyurethane aerogels are superelastic materials with glass transition temperatures in the range of 30 ^{o}C to 80 ^{o}C depending on the diol, ranging from ethylene glycol to tetraethylene glycol, and demonstrate a strong shape-memory effect.[13,14,15] According to that effect,[16,17] these aerogels can be heated above their glass-transition temperature (Tg), and stretched to a temporary shape; they can retain that shape indefinitely if they are cooled, under the stretching load, to temperatures well below the glass transition temperature; finally, they can return to their original shape if their temperature is increased back above Tg. Along these lines it was discovered that the shape-recovery rate had a direct relationship with the elastic modulus (stiffness) via a

Markus-type expression.[14] Fast shape-recovery rates is a desirable property for many practical applications, for example in all sorts of actuation.[13,18] Upon further inspection, it was noted the highest elastic moduli were exhibited by bicontinuous microstructures, and the question became whether the higher stiffness of bicontinuous structures was due to that morphology, or to other material properties associated with the particular aerogels that displayed that morphology. In our initial studies of those materials bicontinuous micromorphologies were rather rare and were produced seemingly by chance; their presence could be a function of any of the independent system variables as they were varied according to a statistical design-of-experiments model. Those system variables included the type and ratio of the diols in any particular formulation, the total monomer concentration in the sol, and the chemical identity of the solvent. All formulations used the same catalyst, dibutyltin dilaurate (DBTDL), and its mol ratio to the monomers (e.g., the triisocyanate) was kept constant. Further along the line, although bicontinuous morphologies were rare, it was noted that they resulted from formulations with higher monomer concentrations, and therefore they were associated with faster gelling sols yielding higher density aerogels. The higher stiffness of those materials might have been associated with their higher density.[19] The most common skeletal frameworks consisted of spheroidal particles. Frameworks consisting of larger spherical particles were associated with lower monomer concentrations, and therefore slower gelling sols yielding lower density aerogels. The lower stiffness of those materials might have been associated with their lower density.[19] Clearly, although the higher stiffness of samples with bicontinuous morphologies could be attributed to that morphology, it could also very well

be associated with the higher densities of those samples, or even with the different mixtures of diols used in their formulation.

At this point it was reasoned that if bicontinuous morphologies are related only to the gelation time, then in order to deconvolute the role of morphology from other material properties, and therefore confirm or reject its relationship to stiffness, all other systems variables, like for example the sol concentration, should remain constant and the only parameter that should be allowed to vary is the gelation time. The latter is related to the rate of polymerization, and therefore it should be controllable through the catalyst: more active catalysts should bring about faster polymerization, and therefore faster solidification of the phase separated liquid polymer, thus capturing the structural evolution at or closer to an ideal bicontinuous morphology; then if those aerogels are stiffer, their higher moduli would be associated only with their morphology. Along this line of reasoning, a second way to control the rate of polymerization was by varying the catalyst concentration. According to the logic set forth here, irrespective of the catalyst and its concentration, the morphology (and stiffness) of the resulting aerogels should be similar to one another as long as they come from sols with similar gelation times. In other words, gelation time becomes a numerical proxy for the morphology of the polyurethane aerogels of this study, in the same conceptual context as the K-index previously for the aliphatic polyurea aerogels derived from the same triisocynate.[11]

Typical catalysts for urethane formation are based on metal ions, tertiary amines (e.g., 1,4-diazobicyclo[2,2,2]octane, abbreviated as DABCO) and selected organic acids. Among metal based catalysts the most common one has been DBTDL, which has been effective in the reaction of isocyanates with polyether diols.[20] Therefore, as mentioned

above, DBTDL was the catalyst of choice for the synthesis of shape-memory polyurethane aerogels from Desmodur N3300A triisocyanate and short-chain glycols.[13,14,15] Non-tin based metal catalysts include acetyl acetonate complexes of Cr^{+3}, Fe^{+3}, Cu^{+2}, Sn^{+2}, Mn^{+2}, Zr^{+4}, Hf^{+4}, In^{+3}, and Zn^{+2},[21] and they have been also effective with polyester diols.[20] In this study we used anhydrous metal salts, mostly chlorides, and the criterion for their selection was their solubility in the gelation solvent (acetonitrile). Study of metal-ion catalysis of the isocyanate-butanol reaction dates back in the mid-1960s.[22] It was reported that their effect varied based on steric factors of the isocyanate, and it was proposed that metal ions increased the electrophilic character of the isocyanate by coordinating with its oxygen or nitrogen. This mechanistic route does not seem to be in operation with the glycols of this study.

Based on the above, the triisocyanate (isocyanurate-based Desmodur N3300A triisocyanate), the diol (triethylene glycol, TEG) and their concentration (20% w/w) were kept constant throughout this study. The reaction rate, and thereby the gelation time, was varied from minutes to hours, both with the chemical identity of the metal ion catalyst and its concentration. The catalyst-to-isocyanate mol ratio of DBTDL (1:120) in our previous studies with related materials[13,14,15] was used as a point of reference. All other catalyst concentrations are referenced as multiples of that ratio. The resulting polymeric aerogels were classified as a special type of polyisocyanurate-polyurethane (PIR-PUR) materials (Scheme 1), in which the isocyanurate ring was introduced as part of the isocyanate rather than formed in situ. In support of the view that gelation follows a phase-separation of a liquid-oligomer path leading first to smaller spherules that coalesce to larger ones at longer gelation times,[23] it was confirmed that irrespective of the catalyst

and its concentration, aerogels from similar gelation times had similar microstructures (e.g., consisting of similar size spherical particles). Bicontinuous morphologies were observed only in aerogels from very fast gelling sols (<10 min), supporting that these morphologies lie along the same sequence of events, comprising spherule precursors. With a reliable supply of bicontinuous morphologies, it was possible to confirm that all bicontinuous structures are stiffer than those consisting of spherical microparticles, and since the gelation time became a predictor of morphology, it was also possible to correlate stiffness with gelation time.

Scheme 1. Preparation of PIR-PUR aerogel for this study.

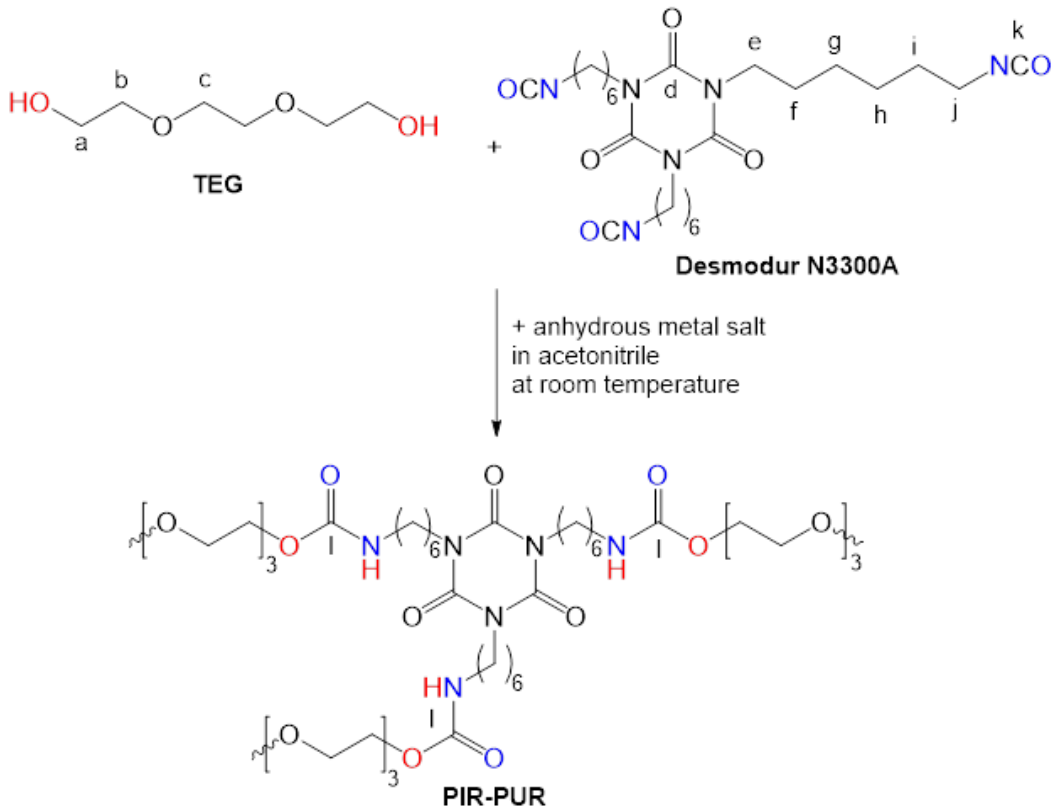

2. RESULTS AND DISCUSSION

2.1. PREPARATION OF PIR-PUR AEROGELS USING ANHYDROUS METAL SALTS AS CATALYSTS

The polyurethane aerogels for this study were obtained by drying polyurethane wet gels in an autoclave by first extracting the pore filling solvent with liquid CO_2 that was then converted to a supercritical fluid, and was vented off like a gas, according to well-established procedures.[24] Referring to Scheme 1, Desmodur N3300A and TEG were introduced into the gelation process at their stoichiometric mol ratio of 2:3. The gelation solvent was acetonitrile and the total monomer concentration (N300A + TEG) was set at 20% w/w for all samples – all experiments. Thus the only variables amongst all samples were the chemical identity and the concentration of the catalyst, as designed (refer to the Introduction). Figure 1A shows the elements whose ions were tested as catalysts.

With the exception of $Cd(NO_3)_2$, $Tl(NO_3)_3$, and $Ni(OTf)_2$ (TfO: triflate), all other metallic ions were introduced as the chloride salts. Stock solutions of these metal salts were prepared in anhydrous acetonitrile. TEG and N3300A were dissolved in acetonitrile separately. Predetermined amounts of each catalyst stock solution were added to each TEG solution. Then the TEG/catalyst solutions were mixed with the triisocyanate solutions to form the sols as described in the Experimental section. Color-coding in Figure 1A designates elements whose salts were insoluble in acetonitrile (yellow), elements whose salts were soluble but did not induce gelation (red) and elements whose salts did induce gelation (blue).

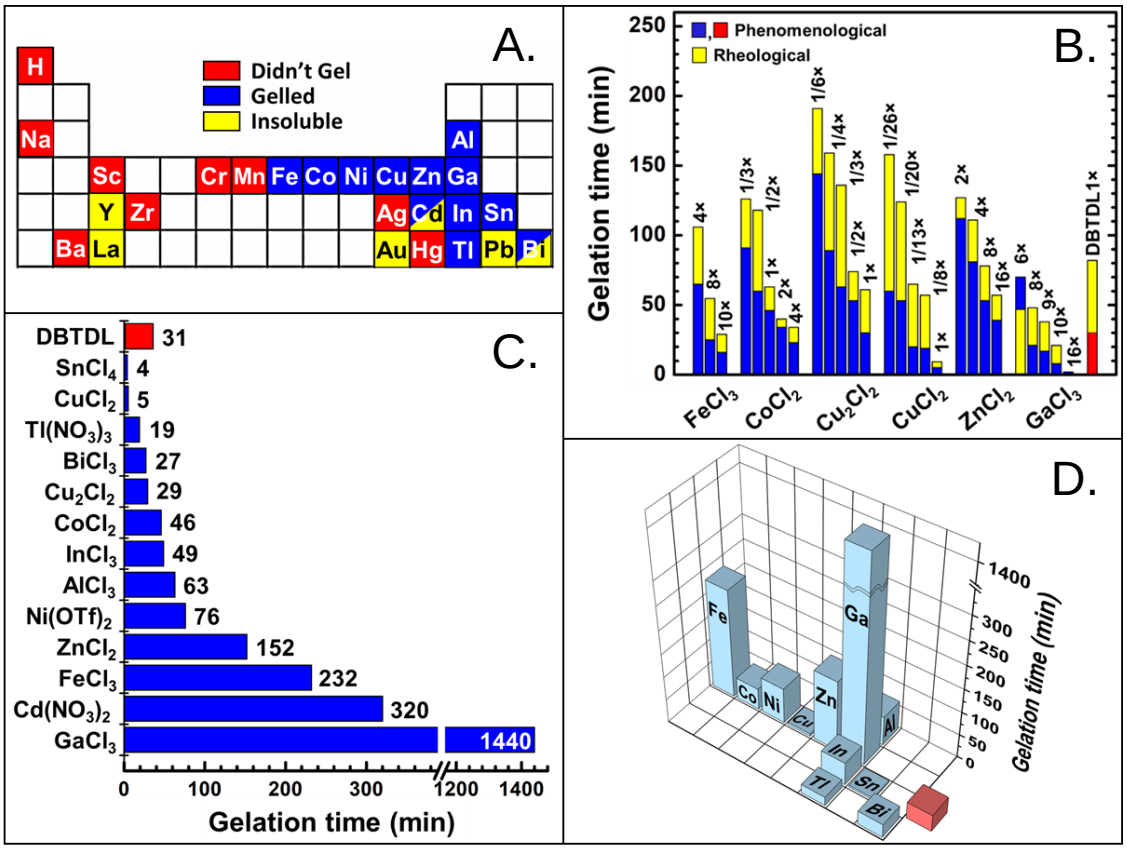

Figure 1. (A) Metals whose metal salts were tested for catalytic activity in the reaction of Scheme 1. (B) Comparison of rheological versus phenomenological gelation times for selected salts at various concentrations, which are expressed as multiples for the reference concentration (1×) of DBTDL – see text. (C) Comparison of the phenomenological gelation time of all catalysts at the reference concentration (1×). (D) Data from frame (C) plotted relative to the position of the elements in the periodic table. DBTDL is shown as a red box outside the frame.

$Cd(NO_3)_2$ and $BiCl_3$ were not fully soluble in acetonitrile, but they did dissolve in the presence of TEG. That posed experimental difficulties, so for comparison purposes (refer to Figure 1C, below) only one concentration of those salts was tested, the one equal to DBTDL (1×).

The catalytic activity as a function of the metal ion and its concentration was assessed by the gelation time, t_{gel}, measured from the time the triisocyanate solution was

added to the TEG/metal ion solution. There are two ways to obtain t_{gel}. Using rheology in the oscillatory mode, tgel is defined as the common crossing point of all tanδ (= loss modulus / storage modulus) for all oscillatory frequencies employed in the experiment.[25,26,27] On the other hand, the phenomenological gelation time is taken as the point when the solution stops flowing. Figure 1B shows that in general, whenever both types of t_{gel} values were obtained, the phenomenological t_{gel} values were shorter than their rheological counterparts, but followed the same pattern both within the same catalyst as a function of its concentration, and also across catalysts. The ensuing discussion is based on the phenomenological t_{gel} values. For the purposes of Figure 1B, the different molar concentrations of each catalyst are referred to as multiples of the standard concentration of DBTDL ([DBTDL] = 1.94 mM, referred to as 1×, see Table B.1 in Supporting Information), which was its concentration in the same monomer-concentration sols (20% w/w) in our previous studies that became the impetus of this work.[13,14,15] In turn, Figure 1C shows the relative catalytic activity of all viable metal ions from Figure 1A, by comparing the gelation time of the common 20% w/w acetonitrile sol used in this study with all metal ions at the same concentration (1×). According to Figure 1C, the most active catalyst was $SnCl_4$ (t_{gel} = 4 min), followed by $CuCl_2$ (t_{gel} = 5 min). The least active catalyst was GaCl3 (t_{gel} = 24 h). Near-DBTDL catalytic activity at 1× (t_{gel} = 31 min) was displayed by Cu_2Cl_2 (t_{gel} = 29 min) and $BiCl_3$ (t_{gel} = 27 min). Finally, Figure 1D relates catalytic activity to the position of the corresponding elements in the periodic table. Catalytic activity is concentrated mainly across the first row of the d-block elements and the first group (number 13) of the p-block elements. Within the third-row d-block elements, t_{gel} decreased, and therefore catalytic activity increased from Fe^{3+} to

Cu^{2+}, and then t_{gel} increased and catalytic activity decreased with Zn^{2+}. Then activity decreased even further by moving toward the group [13], p-block element gallium; in fact $GaCl_3$ defined the global minimum of catalytic activity (t_{gel} = 24 h). Along group 13, and across $GaCl_3$, $AlCl_3$ (t_{gel} = 63 min) showed an activity between $CoCl_2$ (t_{gel} = 46 min) and $Ni(OTf)_2$ (t_{gel} = 76 min), while on the other side of $GaCl_3$, $InCl_3$ (t_{gel} = 49 min) was more active than both $AlCl_3$ and $GaCl_3$, and catalytic activity was increased further by moving toward $Tl(NO_3)_3$, which was the third most active catalyst of all the metal salts tested (t_{gel} = 19 min), behind only of $SnCl_4$ and $CuCl_2$.

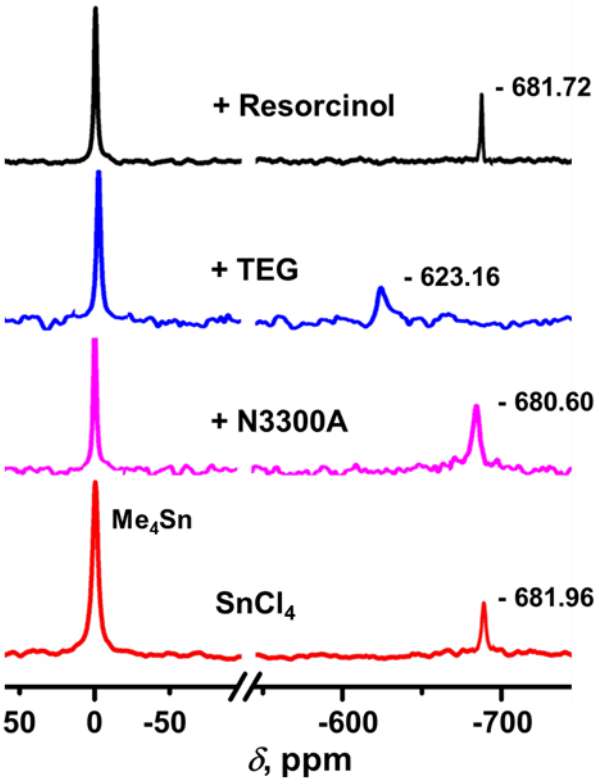

Figure 2. Liquid ^{119}Sn NMR of $SnCl_4$ in CD_3CN with several separate additives in 1:1 mol:mol ratio. Spectra were referenced externally to pure tetramethyltin using a coaxial tube.

The increase in catalytic activity from ferric chloride to $CuCl_2$ and the subsequent decrease with $ZnCl_2$ parallels the Irvin-Williams series of thermodynamic stability of the complexes of the corresponding ions.[28] That implies some sort of association of the starting materials with the catalyst. Using $SnCl_4$ as a proxy for all metal salt catalysts, and its diamagnetic NMR-active nucleus as a probe, we conducted an ^{119}Sn NMR study of the interaction of the reactants shown in Scheme 1 with $SnCl_4$ in CD_3CN – see Figure 2. A resonance from $SnCl_4$ was observed at -681.96 ppm versus external neat $Sn(CH_3)_4$. The chemical shift of $SnCl_4$ in pure form or in weakly interacting solvents (e.g., CS_2 or CH_2Cl_2) has been reported at around -150 ppm.[29] The large negative chemical shift of $SnCl_4$ in acetonitrile implies strong interaction (complexation) with the solvent. When isocyanate was added in the $SnCl_4$ solution in a 1:1 mol:mol ratio, only a slight downfield change in the chemical shift was observed (to -680.60 ppm). On the other hand, when TEG was added to the $SnCl_4$ solution, in the same 1:1 mol:mol ratio, the ^{119}Sn resonance shifted significantly downfield (to -623.16 ppm) that is towards the area of its value in pure diethylether (-606 ppm), as well as in weakly interacting CH_2Cl_2 containing either a 5-molar excess of diethyl ether (-599.4 ppm), or an equimolar amount of chelating dimethoxyethane (-550.0 ppm),[29] clearly indicating that TEG interacts strongly with $SnCl_4$. On the other hand, an aromatic alcohol (resorcinol) did not cause any noteworthy shift of the ^{119}Sn resonance in acetonitrile (with resorcinol at 1:1 mol:mol ratio in solution: -681.72 ppm). Reasonably then, in analogy to chelating dimethoxyether,[29] the interaction of $SnCl_4$ with TEG was assisted by its ability to chelate via a 5-membered ring. Assuming that TEG interacts with the other metal salts in the same general fashion provides a reasonable explanation for the assistance offered by TEG

in dissolving the metal salts in acetonitrile, most remarkably noted with $Cd(NO_3)_2$ and $BiCl_3$. Complexation of the metal ions with TEG in the primary step puts the interaction with the isocyanate second in the sequence of events, thereby, without going into further speculation, the mechanism of urethane formation catalyzed with the metal ions of Figure 1A resembles the insertion mechanism of the DBTDL-catalyzed urethane formation,[30] and explains adequately well the trend in the d-block elements of the third raw, including the higher activity of harder Cu^{2+} than softer Cu^{+}. However, the behavior down group 13 of the p-block elements is more perplexing. Here the softer metal ions (indium, thallium) were the most active catalysts, but the behavior of $GaCl_3$, being globally the least active catalyst, was surprising. Ga^{3+} is a hard Lewis acid, definitely harder than Zn^{2+}, and following the logic of the Irvin-Williams series $GaCl_3$ would be expected to be more active than $ZnCl_2$. Its behavior indicates that the interaction of the Ga(III) metal center with TEG is hindered, which in turn means either that $GaCl_3$ (in itself a soft acid) or its associative complex with acetonitrile does not interact strongly with TEG. Overall, in spite of differences in their interaction with TEG or the isocyanate, the salts of the elements of Figure 1 comprise a set of catalysts with a widely variable activity toward the reaction of Scheme 1, with all other parameters remaining constant, as designed.

2.2. CHEMICAL AND GENERAL MATERIALS CHARACTERIZATION OF THE PIR-PUR AEROGELS

All PIR-PUR aerogels of this study were expected to have the same chemical composition, and that was supported within the resolution of FTIR and solid-state CPMAS ^{13}C NMR spectroscopy.

The FTIR spectra of all materials of this study (Figure 3A) were dominated by the isocyanurate carbonyl stretch near 1680 cm^{-1}. The 2300−2000 cm^{-1} region was clean of any unreacted N=C=O stretch. The free urethane carbonyl stretch was observed as a 1729 cm^{-1} shoulder of the intense isocyanurate absorption. H-bonded urethane carbonyl groups would appear at 1600-1640 cm^{-1}, but they were masked by the intense isocyanurate absorption. Other important absorptions at lower energies than the carbonyl include a band at 1530 cm-1 that is assigned to N−H bending coupled to C−N stretching,[31] and the bands at 1244, 1120, and 1048 cm^{-1} attributed to the tri-ethylene glycol and urethane asymmetric and symmetric C−O−C stretches.[31,32] The methylene (–CH2–) in-plane bending was observed at 764 cm^{-1}.[33] At higher energies than the carbonyl, all C-H stretches appeared at lower energies than 3000 cm^{-1} as two bands at 2900 cm^{-1} and 2850 cm^{-1} consistent with their aliphatic character. The N-H stretch was broad extending the region from 3100 to 3800 cm^{-1}, and could be deconvoluted (data not shown) into a band assigned to free N-H stretch in the 3423−3545 cm^{-1} range; into a second band assigned to N-H stretch of NH H-bonded to carbonyl (NH···O=C) in the 3331−3341 cm^{-1} range; and a third, lower intensity band assigned to N-H stretch of NH H-bonded to glycol groups (NH···$O(CH_2)_2$) in the 3204−3234 cm^{-1} range.[34] The relative intensities of the deconvoluted bands were about 3.0-to-7.0-to-0.2 for all materials, suggesting no significance differences in the chemical environment around the urethane NH groups amongst the different metal-salt catalyzed PIR-PUR aerogels. The ATR-FTIR spectra of some samples were also obtained after thermomechanical cycling (see below), and the ratio of the three bands was in general modified in slight favor of the NH···O=C hydrogen-bonded groups at the expense of the free N-H stretch.[35]

Similarly, the solid-state ^{13}C NMR spectra of the various samples were practically identical irrespective of catalyst (Figure 3B). Resonances in the 15-45 ppm range were assigned to the CH_2 carbons coming from the triisocyanate. The resonances in the 60-80 ppm range correspond to the CH_2 carbons from TEG. A sharp resonance at approximately 149 ppm was due to the carbonyl carbon of the isocyanurate ring of the triisocyanate. The resonance at 156 ppm corresponds to the carbonyl carbon of the urethane groups. The relative band intensities were the same among materials obtained with the various catalysts.

Albeit being chemically similar and having been formulated at the same 20% w/w concentration of monomers in the sol, the PIR-PUR aerogels of this study showed some small variations in their basic material properties (see Table B.2 in Appendix B of the Supporting Information). All samples shrunk linearly between 21.9 – 31.8%. The general, trend was that as the catalyst concentration decreased, i.e., at longer gelation times, shrinkage decreased. The differential shrinkage led to a slight variation in bulk densities (ρb), which span the range from 0.309 g cm-3 to 0.379 g cm-3. The skeletal densities (ρs) of all the PIR-PUR samples were between 1.203 g cm-3 and 1.240 g cm-3, and the porosities (Π) calculated from the bulk and skeletal density data via $\Pi = 100\times(\rho_s-\rho_b)/\rho_s$, were in the range of 69-75% v/v. BET surface areas were about 1 $m^2\ g^{-1}$ or less, (Table B.2) consistent with a lack of fine nanostructure. The later was investigated with SEM. Representative microstructures are shown in Figure 4. Consistent with the conclusion from the BET surface area data, samples lacked fine nanostructure.

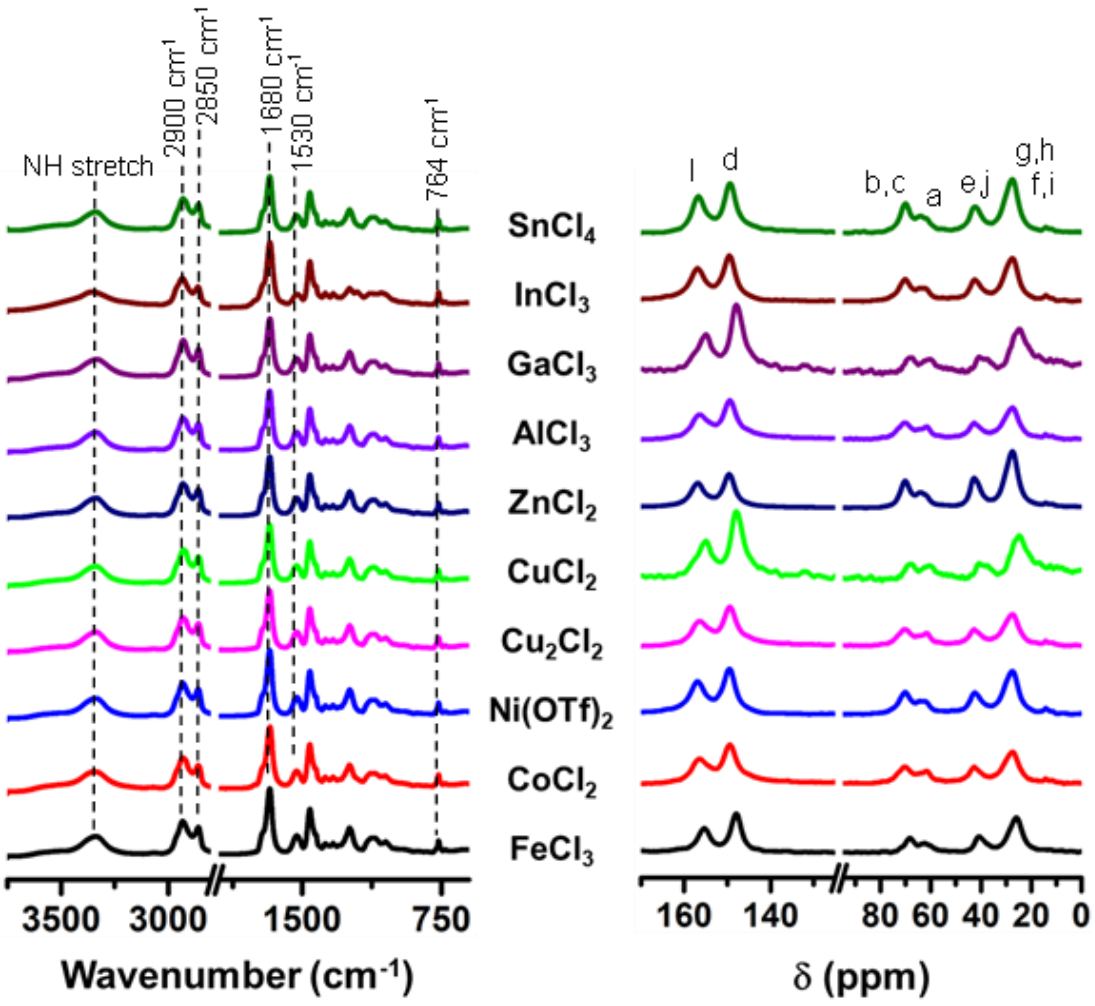

Figure 3. ATR-FTIR (left) and solid-state CPMAS ^{13}C NMR spectra (right) of polyurethane aerogels prepared according to Scheme 1, and catalyzed with the metal salts indicated in the figure.

2.3. MICROMORPHOLOGY OF PIR-PUR AEROGELS AND ITS EFFECT ON PROPERTIES

Representative microstructures are shown in Figure 4. Consistent with the conclusion from the BET surface area data, samples lacked fine nanostructure. Throughout the sample range, the smallest features were in the micron-size regime.

However, one consistent theme was that at short gelation times (around 5 min or less), which could be achieved either with very active catalysts (Figure 1C) or with high concentrations of even the less active ones (e.g., Figure 1B), the microstructures were bicontinuous, meaning that the solid and the pore networks looked similar, and in fact they could be conceptually interchanged. Interestingly, particles could still be discerned on bicontinuous frameworks, but the diameters of the interparticle connecting necks were similar to the diameters of the particles themselves. As the gelation time increased (to 20-30 min or so), the network consisted of small microspheres interconnected with necks narrower than their diameters. Eventually, at long gelation times (75 min or more), achievable either with about the standard (1x) concentration of the less active catalysts of Figure 1C or with low concentrations of the more active catalysts (Figure 1B), smaller spheres seem to have coalesced into larger spherical particles. Polyurethane formation (Scheme 1) is a well-defined step growth process.[30,36]

The microstructural evolution as a function of the gelation time adds another element into that process as it bears the signature of an early separation of a liquid phase of oligomers; within that phase the metal-salt catalyzed step-growth polymerization process continues until the phase gets solidified. Depending on the catalyst and its concentration, solidification may happen fast, freezing (chemically) the network into a bicontinuous morphology, or slower, allowing time for coalescence of the liquid phase of oligomers into small droplets in the beginning and larger ones later on.[12,23] The overarching conclusion at this point is that use of different catalysts has allowed full control over the morphology of this class of aliphatic polyurethane gels, and leaves no room for doubt that the only factor that controls nanomorphology is the gelation time.

Extracting particle diameters from SEM data for small and large spherical particles is straightforward. However, since particles are still discernible on bicontinuous frameworks (see for example "4 ± 2" column in Figure 4), using the ImageJ software package,[37] every concave curve along bicontinuous frameworks could be fitted to a circle whose diameter was associated with the diameter of a particle, albeit fused with its neighbors as described above. Choosing aerogels produced with $CuCl_2$ as an example, Figure 5A shows a strong correlation of particle diameters with the corresponding gelation times. Subsequently, because all samples of this study were made with the same amount of material (recall that the monomer concentration was fixed at 20% w/w throughout this study) it was reasoned that large well-separated spheres leave the least amount of material in the interparticle neck zones, while at the opposite end, small, merged skeletal particles with neck diameters close to the particle diameters place the maximum amount of material in the neck zones.

If this hypothesis is correct, properties like the solid thermal conduction are expected to be higher through bicontinuous materials obtained at short gelation times. Indeed, Figures 5B and 5C show inverse relationships for both the total thermal conductivity (λ_{Total} – primary data) and the through-the-solid thermal conductivity (λ_s – calculated via $\lambda_s = \lambda_{Total} - \lambda_g$) of the various $CuCl_2$-derived aerogels as a function of either the gelation time or the skeletal particle diameter. Owing to the similar porosities and pore sizes of the various samples of this study the correction for the gaseous thermal conductivity (λ_g) upon λ_{Total} is similar for all samples, and therefore both λ_{Total} and λ_s follow the same trend with both the gelation time and the particle diameter – only the correlation improves when considering λ_s (see legend of Figure 5).

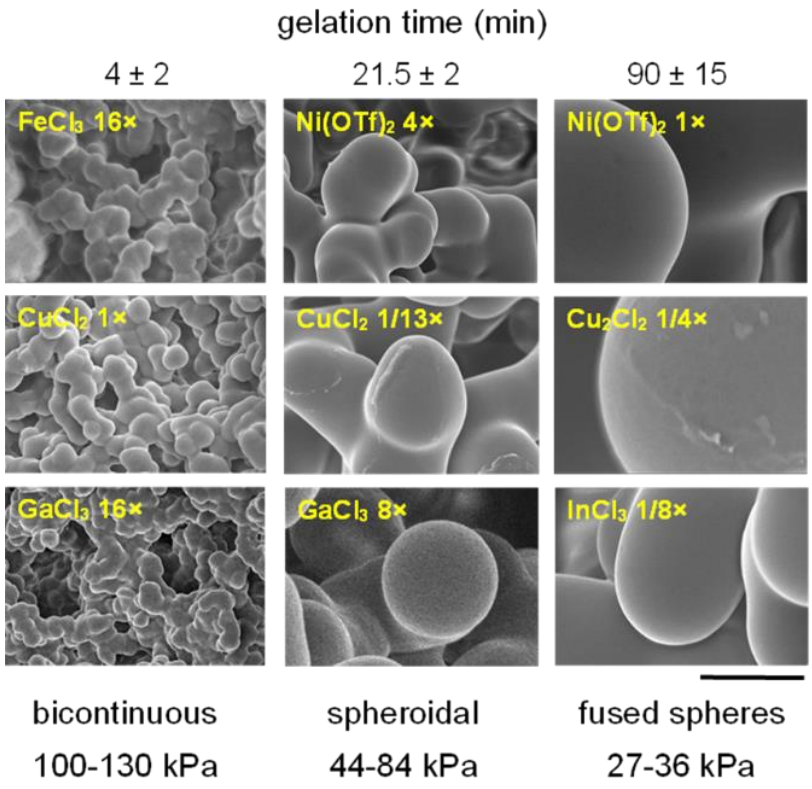

Figure 4. Scanning electron microscopy of representative samples across the domain of the catalysts and their concentrations. Images are segregated in columns according to the gelation time. Magnification: 10,000×. Common scale bar: 5 μm.

The λ_{Total} data of Figure 5 were collected using the hot plate method as described in the Experimental section. All λ_{Total} data and the data needed for the calculation of the λ_g correction toward λ_s are presented in Table B.3 of Appendix.

Further support for the role of the bicontinuous versus the spheroidal morphologies on macroscopic properties that depend on the interparticle neck zones is found through the mechanical characterization of the PIR-PUR aerogels of this study.

2.4. MECHANICAL PROPERTIES AS A FUNCTION OF THE MORPHOLOGY OF THE PIR-PUR AEROGELS OF THIS STUDY

2.4.1. Thermomechanical Analysis and the Shape Memory Effect. The study of the mechanical properties of the PIR-PUR aerogels of this work was guided by the shape-memory effect expected from this kind of materials,[13,14,15] and was carried out using Dynamic Mechanical Analysis (DMA) in the tension mode as a function of the temperature (see Experimental section). For this, first, it was investigated whether the glass transition temperatures (Tg) were in line with what it was expected from this type of materials.[13,14,15] At temperatures lower than their Tg's, all samples displayed storage moduli (E') approximately 10× higher than their loss moduli (E''). Tg was defined as the temperature of the maximum value of the energy dissipation parameter, tan $\delta = E''/E'$. The Tg values of all samples of this study were found close to one another, in the 30-34.5 ^{o}C range, as expected for materials with the same chemical composition.

Once Tg had been determined, fresh, as-prepared samples were heated to and equilibrated at their deformation temperature, $T_d = T_g + 10\ ^{o}C$. Subsequently, they were stretched to near their break point (about 60% strain, determined previously with other samples), and the stress-strain curve was recorded (Figure 6A, segment 1). While under the constant stress at their maximum elongation (strain), samples were cooled to their fixation temperature, T_f (= T_g - 20 ^{o}C) – see Figure 6A, segment 2. At T_f stress was removed (Figure 6A, segment 3) and samples were allowed to equilibrate at T_f at the foot of segments 3 for 15 min. As noted in Figure 6A, segment 3, samples retained most of the strain even though stress had been removed. Finally, samples were heated back up to their recovery temperature ($T_r = T_d = T_g + 10\ ^{o}C$ – see Figure 6A, segment 4). Strain was

recorded and is reported throughout all four phases of the experiment of Figure 6A. In general, during this first thermomechanical cycle strain recovery was not complete; a small amount of residual strain was retained within the samples due to molecular settling phenomena.[13,14,15] The stretch-cool/fix-recover cycle was repeated another four times. Post-settling the stress-strain-temperature curves of Figure 6A practically coincided with one another and the strain recovery after each cycle was complete.

The shape-memory effect of the samples of this study is assessed via three figures of merit: the strain fixity and the strain recovery ratios, and the fill factor. Of interest is also the elastic modulus. The figures of merit of all samples for all five cycles are given in Tables B.4-B.6 of Appendix B in Supporting Information. Elastic modulus data along Figure 6, segment 1 are provided in Table B.7 of Appendix V in Supporting Information.

Quantitatively, the strain fixity ratio, $R_f(N)$, quantifies how well a sample retains its temporary (stretched) shape at the foot of segment 3 of Figure 6A, i.e., at temperatures sufficiently lower than T_g after stress is removed and samples are given time to equilibrate. $R_f(N)$ was calculated for each cycle, N, via equation 1:

$$R_f(N) = \frac{\varepsilon_u(N)}{\varepsilon_m(N)} \times 10 \quad (1)$$

where $\varepsilon_u(N)$ is the equilibrium strain in the sample at the bottom of segment 3 of the curve of Figure 6A, and $\varepsilon_m(N)$ is the maximum strain imposed on a sample at T_d of each cycle. In general, for PIR-PUR shape-memory aerogels Rf(N) is near 100%.[13,14,15]

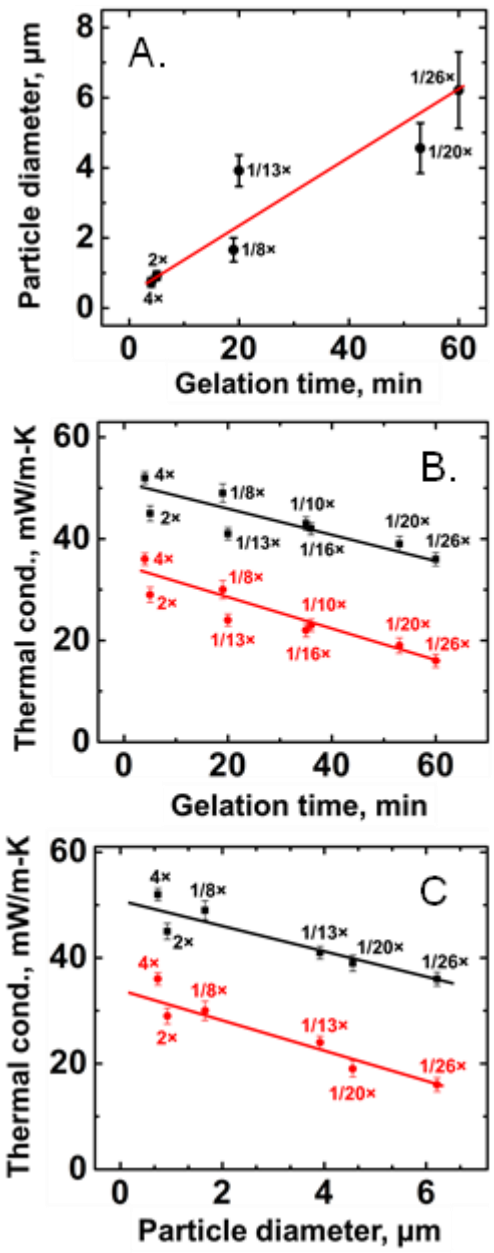

Figure 5. (A) Correlation of particle diameters calculated from SEM images via the ImageJ software, and phenomenological gelation times of $CuCl_2$-catalyzed PIR-PUR aerogels at the concentrations shown ($R^2 = 0.83$). (B) Total thermal conductivity (λ_{Total}, black line, $R^2 = 0.66$) and through-the-solid thermal conductivity (λ_s, red line, $R^2 = 0.83$) of $CuCl_2$-catalyzed samples as a function of the gelation time. (C) Total thermal conductivity (λ_{Total}, black line, $R^2 = 0.82$) and through-the-solid thermal conductivity (λ_s, red line, $R^2 = 0.89$) of $CuCl_2$-catalyzed samples as a function of the particle diameter.

Indeed, the strain fixity ratio of all samples from all catalysts of this study was around 99% (Figure 6B).

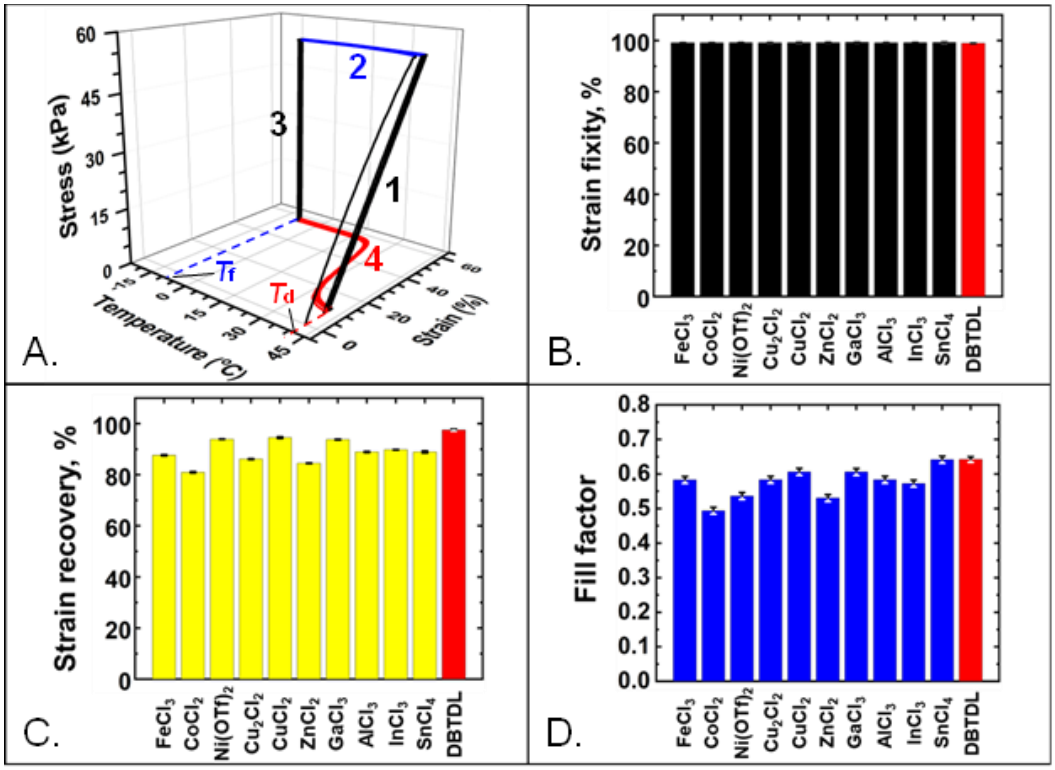

Figure 6. (A) Typical five-cycle thermomechanical experiment between deformation temperature (T_d) and fixing temperature (T_f - see text). (B)-(D) Average values of the three figures of merit (strain fixity, strain recovery and fill factor) over cycles 2-5, for each catalyst over all their formulations and therefore gelation times and morphologies. (Note the negligible variability within each catalyst, but the non-insignificant variation across catalysts).

The strain recovery ratio, $R_r(N)$ quantifies the ability of the samples to recover their initial dimensions (shape) after each thermomechanical cycle. $R_r(N)$ was calculated for each cycle, N, via equation 2:

$$R_r(N) = \frac{\varepsilon_m(N) - \varepsilon_p(N)}{\varepsilon_m(N)} \times 100 \quad (2)$$

where $\varepsilon_p(N)$ is the residual strain at the end of segment 4 of the curve of Figure 6A. All $R_r(N)$ values of all the different samples of this study are summarized in Figure 6C in bar graph form as averages of post—settling cycles 2-5 of all samples within each catalyst, as shown. Judging from the small standard deviations it was concluded that there was no significant variation in strain recovery among samples from various concentrations of the same catalyst, therefore at different gelation times and morphologies, but there was some variability between the various catalysts. The lowest average Rr(N) value was noted for the samples prepared with $ZnCl_2$ (85%) and the highest values were obtained with $GaCl_3$ (93%) and $CuCl_2$(94%).

Finally, the Fill Factor, FF(N), the overall performance assessor for the shape-memory effect, was calculated as the ratio of the area under the strain versus temperature curve over the projection of the entire 3D thermomechanical curves like those of Figure 6A on the Temperature / Strain plain. The FF(N) values depend on the recovery rate, namely on the sharpness of the sigmoidal part of the recovery curve on the Temperature / Strain plain. Just like $R_r(N)$, there was no significant variation in the average FF(N) values for $2 \leq N \leq 5$ among samples from various concentrations of the same catalyst, which clearly includes samples with different morphologies, but there was variability between samples obtained with different catalysts. And, although the differences in the average post-settling values of $R_r(2 \leq N \leq 5)$ and $FF(2 \leq N \leq 5)$ among aerogels from different catalysts were small, nevertheless they were not statistically insignificant, and yet hard to speculate upon. That variability among catalysts notwithstanding, for most samples the average FF(N) values were over 0.55, which makes for a strong shape-memory effect.

2.4.2. Stiffness and Morphology. The elastic modulus, E, of the various PIR-PUR samples was determined from the slopes of the stress-strain curves at Td (Figure 6A, segment 1) and all values for all samples are provided in Table B.7 of Appendix B in Supporting Information.

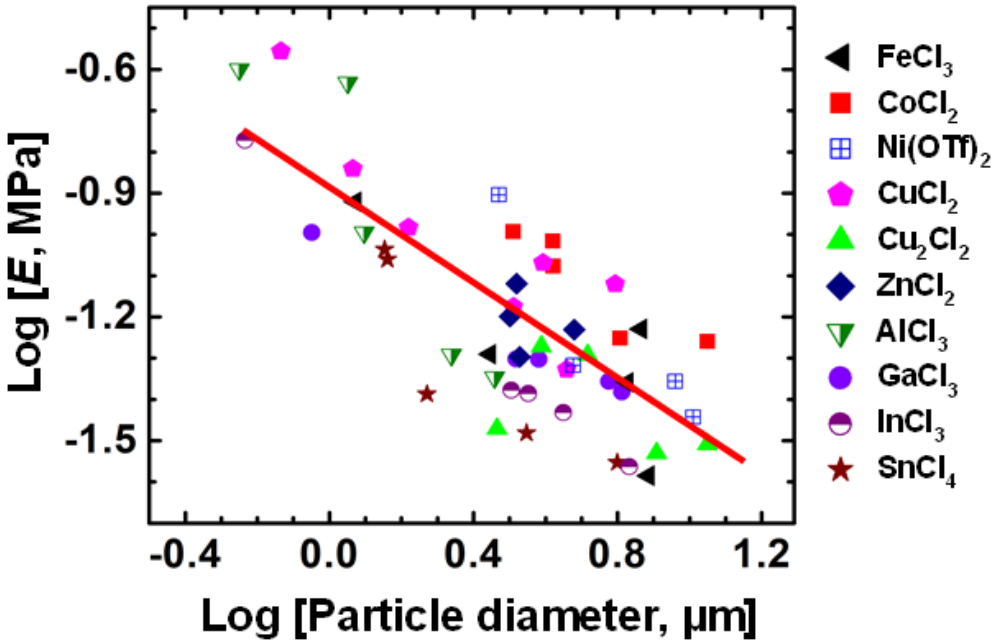

Figure 7. Double logarithmic plot of the average (over cycles 2-5) elastic moduli, E, of all samples prepared with all catalysts at all concentrations, versus the particle diameter of each sample. Particle diameters (from Table B.2) were calculated from the SEM data using the ImageJ software. Referring to Figure B.1 in Appendix V of the Supporting Information, the correlation coefficient of this plot (0.59) is improved slightly by normalizing the E values with the average fill factors of the catalysts (see Figure 6D) and the bulk densities of the samples (from Table B.2).

The average values of the post-settling moduli (cycles 2-5) decreased with increasing gelation time; that is, samples consisting of bicontinuous networks, coming from the shortest-gelling sols, were stiffer than samples consisting of spheroidal networks from longer-gelling sols, which in turn were stiffer than samples consisting of larger

spheres from the longest gelling sols. For typical values of the elastic moduli together with the images of the corresponding morphologies refer to Figure 4. Since the gelation time and the skeletal particle size are related directly (see for example Figure 5A), it was found that all E values of all samples with all catalysts at all concentrations are cumulatively related via an inverse exponential relationship to the skeletal particle diameters (Figure 7). If the E values get normalized for tractable (e.g., small variations in bulk density) and intractable factors (small variations in fill factors) the relationship of Figure 7 is improved even further (see Figure S.1 in Appendix V of the Supporting Information). The conclusion from Figures 7 and B.1 is that stiffness increases as the particle size decreases, the limit of course being when skeletal particles merge into a bicontinuous network.

3. CONCLUSION

Using aliphatic PIR-PUR gels and aerogels as our model system, it has been shown that catalysis can be used as a tool to control morphology. In fact, through the catalytic efficiency, the gelation time is the single most important factor that controls morphology. All other parameters remaining constant (sol concentration, solvent), more active catalysts, or higher concentrations of less active ones brought about fast gelation and the corresponding gels had a bicontinuous morphology. As the gelation time increased, bicontinuous structures underwent spherulization first into smaller and then larger microspheres. This sequence is consistent with phase separation of the developing polymer as a liquid that gets solidified later. Having deconvoluted micromorphology

from other material properties like density and porosity, it was possible to show experimentally that the elastic modulus and the thermal conduction through the solid were directly related to the morphology: bicontinuous structures were stiffer and better thermal conductors than structures consisting of small and then of larger microspheres. This was attributed to the size of the interparticle neck zones, which in the bicontinuous morphologies are almost as wide as the diameters of the skeletal particles.

4. EXPERIMENTAL

4.1. SOURCING OF MATERIALS

All reagents and solvents were used as received unless noted otherwise. The aliphatic triisocyanate is available as a pure chemical under the trade name Desmodur N3300A, and was donated generously by Covestro LLC (Pittsburg, PA). Triethyleneglycol (TEG), dibutyltindilaurate (DBTDL), and anhydrous cupric chloride ($CuCl_2$), cuprous chloride (Cu_2Cl_2), ferric chloride ($FeCl_3$), zinc chloride ($ZnCl_2$), aluminum chloride ($AlCl_3$), nickel triflate ($Ni(OTf)_2$), cobalt chloride ($CoCl_2$), tin chloride ($SnCl_4$), gallium chloride ($GaCl_3$), indium chloride ($InCl_3$), thallium nitrate ($Tl(NO_3)_3$), bismuth chloride ($BiCl_3$), cadmium nitrate ($Cd(NO_3)_2$) and anhydrous acetonitrile were purchased from Sigma-Aldrich. Deuterated acetonitrile (CD_3CN), (99.5% atom D) were purchased from Cambridge Isotope Laboratories, Inc. (Tewksbury, MA). Siphon-grade CO_2, N_2 (99.999%) and CO_2 (99.999%) were purchased from Air Gas Co (St. Louis, MO).

4.2. SOL-FORMULATION AND PREPARATION OF SHAPE MEMORY PIR-PUR AEROGELS

The synthesis of the PIR-PUR aerogels of this study was carried out at room temperature in anhydrous acetonitrile. The triisocyanate (Desmodur N3300A) to diol (triethylene glycol, TEG) ratio was set equal to 2:3 mol:mol, and the total weight percent of the two monomers in the sol remained constant at 20% w/w throughout. The only variable amongst the various sol formulations was the chemical identity of the catalyst and its concentration. All catalyst concentrations are referred to as multiples (e.g., 1×, 2×, 1/2×, 1/4× etc.) of a reference concentration (designated as 1×), which was the concentration of dibutyltindilaurate (DBTDL) used in our previous studies of the shape-memory properties of a similar type of PIR-PUR aerogels.[13,14,15] To set that standard concentration, the amount of DBTDL had been set equal to the 1/120 mol:mol of Desmodur N3300A, and in turn that amount had been decided based on the fact it gave reasonable gelation times; for example at 20% w/w sol concentration the gelation time was about 30 min. Thus, in a typical gelation using the standard (or 1×) concentration of DBTDL as catalyst, 2.520 g (5.00 mmol) of Desmodur N3300A was weighted in a vial and 8.55 mL of acetonitrile was added. Meanwhile, 1.125 g (7.50 mmol) of TEG was weighted in a 50 mL round bottom flask, and 10 mL of anhydrous acetonitrile was added. As soon as TEG was dissolved, 25.0 μL (0.0266 g, 0.0422 mmol) of neat DBTDL was added directly into the TEG solution. A few seconds later, after DBTDL had been dissolved, the isocyanate solution was added, using a syringe, to the round bottom flask containing the solution of TEG and DBTDL; the mixture was stirred for about a minute

and then it was poured in plastic syringes (Plastic Norm-Ject Syringes, 20 mL, Fisher Scientific Catalogue No. 14-817-32, 2.53 cm inner diameter) used as molds.

This procedure was adapted to most of the anhydrous metal salts used as catalysts in this study. For this, stock solutions of the metal salts were prepared in a glove box using anhydrous acetonitrile as solvent and at concentrations that depend on their catalytic activity. All sol formulations with all salts at all concentrations are presented in Table B.1 of Appendix I in Supporting Information. The volume of the stock solution that was transferred for each sol was subtracted from the volume of acetonitrile used to dissolve the triisocyanate and the diol, so that the total volume of the sol, and thereby the total monomer concentration in the sol would remain constant. For example, for making a $CuCl_2$ stock solution, anhydrous $CuCl_2$ (2.789 g, 0.0207 mol) was weighted inside a glove box, and was dissolved in 250 mL of acetonitrile in a volumetric flask ($[CuCl_2]_{in\_stock\_solution}$ = 0.0828 M). In order to prepare a sol with about the same concentration of catalyst as in the standard DBTDL sol above, referred to as $CuCl_2$-1× sol, we used 500 μL of this $CuCl_2$ stock solution (containing 0.0414 mmol of $CuCl_2$). Thus, for making that sol, Desmodur N3300A (2.520 g, 5.00 mmol), was weighted in a vial and was dissolved with 8.55 mL of anhydrous acetonitrile; meanwhile, TEG (1.125 g, 7.50 mmol), was weighed directly in a 50 mL three-neck round-bottom flask and was dissolved under N_2 with 9.50 mL of anhydrous acetonitrile at 23 °C. The 500 μL of the stock $CuCl_2$ solution was added to the TEG solution, the mixture was stirred for 1 min, followed by addition of the isocyanate solution. The resulting sol was stirred for another minute and was poured into plastic syringes used as molds (see above). The molds were covered with ParafilmTM and were stored at room temperature for gelation and aging.

The gelation time varied from about 1 min to around 24 h depending on the metal catalyst and its concentration. All gelation times along with other material properties of the resulting aerogels are presented in Table B.2 of Appendix II in Supporting Information. The aging time was kept at about 16 h for all samples. This procedure was repeated several times by varying only the volume of the $CuCl_2$ stock solution that was mixed with the TEG solution, which in turn was always made with 10 mL of anhydrous acetonitrile minus the volume of the $CuCl_2$ stock catalyst solution that was transferred into it, so that the total volume of the TEG/catalyst solution was always equal to 10 mL. As it was mentioned above, the resulting sols are referred to as 4×, 2×, 1×, 1/2×, 1/4× etc. depending on the concentration of the catalyst with respect to the concentration of DBTDL used in the reference sol as described above. Stock solutions of $SnCl_4$, $Tl(NO_3)_3$, Cu_2Cl_2, $CoCl_2$, $InCl_3$, $AlCl_3$, $Ni(OTf)_2$, $ZnCl_2$, $FeCl_3$, and $GaCl_3$ were prepared in a similar manner as just described for $CuCl_2$, and are referred to similarly (see Table B.1 of Appendix I in Supporting Information). Sometimes sonication of the volumetric flask after it was taken out of the glove box helped in the dissolution. The cases of $BiCl_3$ and $Cd(NO_3)_2$ were somewhat different. Those two salts were sparingly soluble in pure anhydrous acetonitrile, but the solubility improved dramatically in the presence of TEG. Thus, with these two salts only the 1× formulation was attempted, by weighing and adding the correct amounts of the solid salts in the TEG solution, following closely the procedure used with DBTDL.

After aging, wet gels were removed from the molds, they were washed first with acetonitrile twice, and then with acetone six times. Each wash lasted for 8 h and the volume of the solvent used was 4× the volume of each wet gel. Finally, acetone-

exchanged wet gels were dried with supercritical fluid (SCF) CO_2 as described in the next section. The resulting aerogels are referred to according to the metal salt used as the catalyst and its relative concentration, (2×, 1×, 1/2×, 1/4× etc.) just like the corresponding sols.

4.3. METHODS

4.3.1. The Gelation Process. The rheological behavior of several sols was monitored during gelation with a TA Instruments AR 2000ex Rheometer using a cone (60 mm diameter, 2º angle) and a Peltier plate geometry with a 500 μm gap between them. The instrument was operated in the oscillation mode and time sweep experiments were performed with a fixed-strain amplitude from the moment of adding the Desmodur N3300A solution into the TEG/catalyst solution. The gel point was determined using a dynamic multiwave method with five superimposed harmonics with frequencies 1, 2, 4, 8 and 16 rad s^{-1}. The strain of the fundamental oscillation (1 rad s^{-1}) was set at 5%.

4.3.2. Drying. Drying of wet gels was carried out in an autoclave (SPIDRY Jumbo Supercritical Point Dryer, SPI Supplies, Inc. West Chester, PA, or a Spe-edSFE system, Applied Separations, Allentown, PA). Samples were loaded into the autoclave at room temperature submerged in fresh acetone filling the sample boat. The pressure vessel was closed, and liquid CO_2 was allowed in at room temperature. Acetone was drained out from the pressure vessel while more liquid CO_2 was allowed in. Samples were kept under liquid CO_2 for 30 min under 80-90 bar pressure at 14 ºC. Then liquid CO_2 was drained out while more liquid CO_2 was allowed in the vessel. The 30 min stay/drain cycle was repeated several times until all acetone was extracted from the pores of the samples; at

that point CO_2 coming out from drain formed a stream of dry ice. Subsequently, the temperature of the autoclave was raised to 40 °C (well above the critical temperature of CO_2), and that condition was maintained for 1 h. Finally, the supercritical fluid (SCF) CO_2 was vented off the autoclave slowly, behaving like a gas.

4.3.3. Chemical Characterization. Liquid-phase ^{119}Sn NMR spectra were recorded with a 400 MHz Varian Unity Inova NMR instrument (^{119}Sn frequency of 149 MHz). Liquid-phase ^{119}Sn NMR spectra were referenced externally using a coaxial tube to tetramethyltin (0 ppm). Solid-state CP TOSS ^{13}C NMR spectra were obtained with a Bruker Avance III 400 MHz spectrometer (^{13}C frequency of 100 MHz), using a 7 mm Bruker MAS probe at a magic-angle spinning rate of 5 kHz, with broadband proton suppression. For this, the aerogel samples were cut in small chunks and were pressed in the rotor. The relaxation delay was set at 5 s. Solid-state ^{13}C NMR spectra were referenced externally to glycine (carbonyl carbon at 176.03 ppm). Chemical shifts are reported versus tetramethylsilane (0 ppm).

Attenuated total reflectance (ATR) FTIR spectroscopy was carried out with a Nicolet iS50 FT-IR, equipped with a ATR accessory model 0012-3XXT. Samples were cut to small chunks that were placed on the diamond crystal (2.8 mm in diameter, with a sampling zone of 2 mm), and ATR-FTIR spectra were obtained by pressing the samples against the crystal with the ATR unit's pressure device (gripper). Maximum throughput of the infrared beam to the detector was achieved via optical alignment that was performed with no sample on the crystal. Data were collected at an incident beam angle of 45° using 32 scans with a resolution of 2 cm^{-1}. In the ATR mode, the penetration depth (pd) and thereby the effective path length (=number of reflections × pd) of the

infrared beam are directly proportional to the wavelength. Thus, an ATR correction was applied by the software of the instrument to the raw data by multiplying the spectra with a wavelength-dependent factor (roughly $\lambda/5$) that adjusted the relative peak intensities. The ν(N−H) bands of several randomly selected spectra were deconvoluted into three Gaussian-shaped peaks using the Origin 9.7 software package.

4.3.4. Physical Characterization. Bulk densities (ρ_b) were calculated from the weight and the physical dimensions of the samples. Skeletal densities (ρ_s) were determined with helium pycnometry using a Micromeritics AccuPyc II 1340 instrument. Porosities (Π), as percent of empty space, were calculated from the ρ_b and ρ_s values via $\Pi = 100\times[(\rho_s-\rho_b)/\rho_s]$. Samples were outgassed for 24 h, at 40 °C, under vacuum, before skeletal density determinations.

4.3.5. Structural Characterization. Structural characterization was carried out with scanning electron microscopy (SEM) with Au/Pd (60/40) coated samples on a Hitachi field-emission microscope Model S-4700. Samples were placed on the stub using C-dot. Thin sticky copper strips were cut and placed on the edges and top of the sample, leaving a small area uncovered for observation.

4.3.6. Thermomechanical Characterization. Thermomechanical characterization was carried out in the tension mode with a TA Instruments Q800 Dynamic Mechanical Analyzer (DMA) equipped with a tension clamp (TA Instruments part no. 984016.901, load cell 18N). All specimens for testing had a rectangular geometry (length 20 mm; width 15 mm; thickness 4−5 mm) in the spirit of ASTM D790-10 and ASTM D4065. Samples were cut off with a knife from larger cylindrical samples dipped

in liquid N2 and were sanded with a 3M sandpaper (320 grit, part no. 98401) while still at cryogenic temperature.

For the determination of glass transition temperatures (T_g), specimens were placed in the load cell at room temperature, and a small tensile force (0.01 N) prevented them from bending. The temperature was stepped to the initial testing temperature, and samples were equilibrated at that temperature for 5 min. Glass transition temperatures (T_g) were extracted from the viscoelastic properties of the samples, which were measured by applying a continuous sinusoidal oscillation (1 Hz) with a strain amplitude equal to 0.3%, while the temperature was ramped from −150 °C to 150 °C at 3 °C min-1. During this time, the loss and storage moduli (E", and E', respectively) were recorded as functions of temperature. Tg was identified as the maximum of the tanδ (= E"/E') plot as a function of temperature.

The shape-memory behavior was studied in the controlled force mode. Sample were fixed in the load cell at room temperature, and then they were equilibrated at their deformation temperature ($T_d = T_g + 10$ °C) for 5 min. Subsequently, samples were stretched with a small tensile force (0.01 N), their length was measured by the instrument and was stored as the starting point. Next, specimens were stretched at a constant force rate of 1 N min^{-1} up to near their break point (typically around 60% strain, which was determined previously with an independent test and another sample), and then they were cooled at 5 °C min^{-1}, while under the final stress, to their fixation temperature ($T_f \ll T_g$, typically $T_f = T_g - 20$ °C). At that point (T_f), samples were equilibrated for 5 min, and the tensile force was reduced to 0.01 N. Samples were allowed to relax (fix) under the new stress condition for 15 min (always at T_f) while strain was recorded continuously. Finally,

samples were heated at 1 °C min−1 to their recovery temperature ($T_r = T_d$) while strain was still recorded. Samples were held at T_d for 15 min, and the cycle was repeated. Five such cycles were run successively for each sample, and data were analyzed to extract the elastic moduli and the figures of merit of the shape memory effect (strain fixity, strain recovery, and fill factors) in each cycle. Fill Factors (FF(N)) were obtained for each thermomechanical cycle (N) using the ImageJ software package[37] to calculate the ratio of the area underneath the Temperature/Strain curves over the area under the projection of the entire 3D thermomechanical curve on to the Temperature/Strain plane.[13,14]

4.3.7. Thermal Conductivity. The total thermal conductivities, λ_{Total}, of the $CuCl_2$ catalyzed PIR-PUR aerogels were measured using a custom-made heat flowmeter that includes in sequence from top to bottom:[14] a 10 cm × 10 cm hotplate (at 37.5 °C, bottom), the PIR-PUR aerogel sample, a NIST-calibrated reference sample,[40] and a cold surface (an ice–water bucket). The PIR-PUR aerogel samples used in that configuration were casted as large panels (10 cm × 10 cm × 1 cm) by scaling up proportionally the formulations of Table B.1 in Supporting Information. Those panels were used to cover the 10 cm × 10 cm stage of the hotplate. Solid thermal conductivities, λ_s, were calculated via $\lambda_s = \lambda_{Total} - \lambda_g$, whereas gaseous thermal conductivities, λ_g, were calculated using the Knudsen equation,[41] and assuming negligible heat transfer by radiation ($\lambda_{irr} \approx 0$).

REFERENCES

[1] Leventis, N.; Sotiriou-Leventis, C.; Chandrasekaran, N.; Mulik, S.; Chidambareswarapattar, C.; Sadekar, A.; Mohite, D.; Mahadik, S. S.; Larimore, Z. J.; Lu, H.; Churu, G. Isocyanate-derived Organic Aerogels: Polyureas, Polyimides, Polyamides. *Mater. Res. Soc. Symp. Proc. Mater. Res. Soc.* **2011**, *1306*, mrsf10-1306-bb03-01.

[2] Leventis, N.; Sotiriou-Leventis, C.; Zhang, G.; Rawashdeh, A.-M. M. Nano Engineering Strong Silica Aerogels. *Nano Letters* **2002**, *2*, 957–960.

[3] Lee, J. K.; Gould, G. L.; Rhine, W. Polyurea Based Aerogels for a High Performance Thermal Insulation Material. *J. Sol-Gel Sci. Technol.* **2009**, *49*, 209–220.

[4] Chidambareswarapattar, C.; McCarver, P.M.; Luo, H.; Lu, H.; Sotiriou-Leventis, C.; Leventis, N. Fractal Multiscale Nanoporous Polyurethanes: Flexible to Extremely Rigid Aerogels from Multifunctional Small Molecules. *Chem. Mater.* **2013**, *25*, 3205–3224.

[5] Chidambareswarapattar, C.; Larimore, Z.; Sotiriou-Leventis, C.; Mang, J. T.; Leventis, N. One-step Room-temperature Synthesis of Fibrous Polyimide Aerogels from Anhydrides and Isocyanates and Conversion to Isomorphic Carbons. *J. Mater. Chem.* **2010**, *20*, 9666–9678.

[6] Leventis, N.; Chidambareswarapattar, C.; Mohite, D. P.; Larimore, Z. J.; Lu, H.; Sotiriou-Leventis, C. Multifunctional Porous Aramids (Aerogels) by Efficient Reaction of Carboxylic Acids and Isocyanates. *J. Mater. Chem.* **2011**, *21*, 11981–11986.

[7] Leventis, N. Three Dimensional Core-Shell Superstructures: Mechanically Strong Aerogels. *Acc. Chem. Res.* **2007**, *40*, 874–884.

[8] Odian, G. Principle of Polymerization; Wiley-Interscience: New York, NY (2004).

[9] Weigold, L.; Mohite, D.P.; Mahadik-Khanolkar, S.; Leventis, N.; Reichenauer, G. Correlation of Microstructure and Thermal Conductivity in Nanoporous Solids: The Case of Polyurea Aerogels Synthesized from an Aliphatic Tri-isocyanate and Water. *J. Non-Cryst. Solids* **2013**, *368*, 105–111.

[10] Leventis, N.; Chidambareswarapattar, C.; Bang, A.; Sotiriou-Leventis, C. Cocoon-in-web-like Superhydrophobic Aerogels from Hydrophilic Polyurea and Use in Environmental Remediation. *ACS Appl. Mater. Interfaces* **2014**, *6*, 6872–6882.

[11] Taghvaee, T.; Donthula, S.; Rewatkar, P. M.; Far, H. M.; Sotiriou-Leventis, C.; Leventis, N. K-Index: A Descriptor, Predictor, and Correlator of Complex Nanomorphology to Other Material Properties. *ACS Nano*, **2019**, *13*, 3677–3690.

[12] Leventis, N. Polyurea Aerogels: Synthesis, Material Properties, and Applications. *Polymers* **2022**, *14*, 969.

[13] Donthula, S.; Mandal, C.; Leventis, T.; Schisler, J.; Saeed, A. M.; Sotiriou-Leventis, C.; Leventis, N. Shape Memory Superelastic Poly(isocyanurate-urethane) Aerogels (PIR-PUR) for Deployable Panels and Biomimetic Applications. *Chem. Mater.* **2017**, *29*, 4461–4477.

[14] Donthula, S.; Mandal, C.; Schisler, J.; Leventis, T.; Meador, M. A. B.; Sotiriou-Leventis, C.; Leventis, N. Nanostructure-Dependent Marcus-Type Correlation of the Shape Recovery Rate and the Young's Modulus in Shape Memory Polymer Aerogels. *ACS Appl. Mater. Interf.* **2018**, *10*, 23321–23334.

[15] Malakooti, S.; ud Doulah, A. B. M. S.; Ren, Y.; Kulkarni, V. N.; Soni, R. U.; Edlabadkar, V. A.; Zhang, R.; Vivod, S. L.; Sotiriou-Leventis, C.; Leventis, N.; Lu, H. Meta-Aerogels: Auxetic Shape-Memory Polyurethane Aerogels. *ACS Appl. Polym. Mater.* **2021**, *3*, 5727−5738.

[16] Liu, C; Qin, H; Mather, P. T. Review of Progress in Shape-memory Polymers. *J. Mater. Chem.* **2007**, *17*, 1543–1558.

[17] Zhuo, H. T.; Hu, J. L.; Chen, S. J. Electrospun Polyurethane Nanofibres Having Shape Memory Effect. *Mater. Lett.* **2008**, *62*, 2074–2076.

[18] Lendlein, A.; Gould, O. E. C. Reprogrammable Recovery and Actuation Behaviour of Shape-Memory Polymers. *Nat. Rev. Mater.* **2019**, *4*, 116−133.

[19] Ashby, M. F. The Properties of Foams and Lattices. *Philos. Trans. R. Soc., A* **2006**, *364*, 15−30.

[20] Lima, V.; Pelissoli, N. S. Dullius, J.; Ligabue, R.; Einloft, S. Kinetic Study of Polyurethane Synthesis Using Different Catalytic Systems of Fe, Cu, Sn, and Cr. *J. Appl. Poly. Sci.* **2010**, *115*, 1797-1802.

[21] Schellekens, Y.; Trimpont, B. V.; Goelen, P. J.; Binnemans, K.; Smet, M.; Persoons, M. A. Vos, D. D. Tin-free Catalysts for the Production of Aliphatic Thermoplastic Polyurethanes. *Green Chem*. **2014**, *16,* 4401-4407.

[22] Robins, J. Structural Effects in Metal Ion Catalysis of Isocyanate-Hydroxyl Reactions. *J. Appl. Poly. Sci.* **1965**, *9,* 821-838.

[23] Nakanishi, K.; Tanaka, N. Sol-Gel with Phase Separation Hierarchically Porous Materials Optimized for High-Performance Liquid Chromatography Separations. *Acc. Chem. Res.* **2007**, *40*, 863−873.

[24] Leventis, N.; Elder, I. A.; Rolison, D. R.; Anderson, M. L.; Merzbacher, C. I. Durable Modification of Silica Aerogel Monoliths with Fluorescent 2,7-Diazapyrenium Moieties – Sensing Oxygen near the Speed of Open-Air Diffusion. *Chem. Mater.* **1999**, *11*, 2837–2845.

[25] Winter, H. H. Can the Gel Point of a Cross-linking Polymer Be Detected by the G'-G" Crossover? *Polym. Eng. Sci.* **1987**, *27*, 1698–1702.

[26] Kim, S.-Y.; Choi, D.-G.; Yang, S.-M. Rheological Analysis of the Gelation Behavior of tetraethylorthosilane/vinyltriethoxysilane Hybrid Solutions. *Korean J. Chem. Eng.* **2002**, *19,* 190–196.

[27] Muthukumar, M. Screening Effect on Viscoelasticity Near the Gel Point. *Macromolecules* **1989**, *22*, 4656–4658.

[28] Irving, H.; Williams, R. J. P. The Stability of Transition-metal Complexes. J. Chem. Soc. **1953**, 3192–3210.

[29] Fărcaşiu, D.; Leu, R.; Ream, P. J. The 1 : 1 and 2 : 1 Complexes of Diethyl Ether with Tin Tetrachloride and Their Stability, Studied by ^{119}Sn NMR Spectroscopy. *J. Chem. Soc., Perkin Trans.* **2001**, *2*, 427–431.

[30] Dodge, J. Polyurethanes and Polyureas. In Synthetic Methods in Step-Growth Polymers; Rogers, M.E., Long, T.E., Eds.; Wiley: New York, NY, USA, 2003; pp. 197–263.

[31] Silverstein, R. M.; Bassler, G. C.; Morrill, T. C. Spectroscopic Identification of Organic Compounds, 5th Ed.; John Wiley & Sons, Inc.: New York, **1991**, pp 32-33.

[32] McCarthy, S. J.; Meijs, G. F.; Mitchell, N.; Gunatillake, P. A.; Heath, G.; Brandwood, A.; Schindhelm, K. In-vivo Degradation of Polyurethanes: Transmission-FTIR Microscopic Characterization of Polyurethanes Sectioned by Cryomicrotomy. *Biomaterials* **1997**, *18*, 1387−1409.

[33] Defeyt, C.; Langenbacher, J.; Rivenc, R. Polyurethane coatings used in twentieth century outdoor painted sculptures. Part I: comparative study of various systems by means of ATR-FTIR spectroscopy. *Herit. Sci.* **2017**, *5*, 11.

[34] Mattia, J.; Painter, P. A Comparison of Hydrogen Bonding and Order in a Polyurethane and Poly(Urethane-Urea) and Their Blends with Poly(Ethylene Glycol). *Macromolecules* **2007**, *40,* 1546–1554.

[35] Teo, L. S.; Chen, C. Y.; Kuo, J. F. Fourier Transform Infrared Spectroscopy Study on Effects of Temperature on Hydrogen Bonding in Amine-Containing Polyurethanes and Poly(Urethane-Urea). *Macromolecules* **1997**, *30,* 1793–1799.

[36] Stille, J. K. Step-Growth Polymerization. *J. Chem. Educ*. **1981**, *58,* 862.

[37] https://imagej.nih.gov/

[38] Mulik, S.; Sotiriou-Leventis, C.; Churu, G.; Lu, H.; Leventis, N. Cross-Linking 3D Assemblies of Nanoparticles into Mechanically Strong Aerogels by Surface-Initiated Free-Radical Polymerization. *Chem. Mater*. **2008**, *20*, 5035-5046.

[39] Ratke, L.; Rege, A.; Aney, S. The Effect of Particle Necks on the Mechanical Properties of Aerogels. *Materials* **2023**, *16*, 230.

[40] Zarr, R. R.; Pintar, A. L. Standard Reference Materials: SRM 1453, Expanded Polystyrene Board, for Thermal Conductivity from 281 K to 313K. *NIST Special Publication* **2012**, 260–175, DOI: 10.6028/NIST.SP.260-175.

[41] Lu, X.; Arduini-Schuster, M. C.; Kuhn, J.; Nilsson, O.; Fricke, J.; Pekala, R. W. Thermal Conductivity of Monolithic Organic Aerogels. *Science* **1992**, *255*, 971–972.

SECTION

2. CONCLUSIONS

The mechanical and thermal characteristics of variously designed and synthesized shape memory aerogels were investigated, including those with large pores that were incorporated using 3D printed designs, by external pressure, and by modifying morphology. Incorporation of large voids using a 3D-printed template design gave metamaterial-like behavior, e.g. materials with auxetic properties. Different catalysts were used to create shape memory aerogels with various morphologies, and the impact of the type and catalyst concentration on morphology was investigated. Additionally, the thermal and mechanical properties of shape memory aerogels, which depended on nanomorphology were investigated.

In paper I, we synthesized meta-aerogels, which are potentially significant materials for industrial, aeronautical, and aerospace applications because they combine a negative Poisson's ratio with a thermoresponsive shape-memory effect. Meta-aerogels experience volume contraction upon compression at a temperature above the glass transition temperature of the base polymer ($T_g \approx 30$ °C), and they can be stowed indefinitely in that temporary shape by cooling below T_g. By heating back above T_g, the compressed/shrunk form expands back to their original shape/ size. The particular aerogel material that was used for demonstrating those effects was based on a highly cross-linked poly(isocyanurate urethane) polymeric backbone, and the auxetic form was achieved with parallel tubular voids running the length of a macroscopic block of a standard aerogel of

that material. The Poisson's ratio reached −0.8 at −15% compressive strain. The shape recovery of those meta-aerogels traced a temperature increase as fast as 0.5 °C/s. These materials provide a good platform for further investigation of additive manufacturing applications using molding processes to create useful aerogels.

In paper II, the use of different metal catalysts to control the nanomorphology of aliphatic PIR-PUR aerogels is discussed, with gelation time being the key factor. When more active catalysts or higher concentrations of less-active catalysts are used, faster gelation occurs, resulting in bicontinuous morphologies in the resulting gels. As gelation time increases, the bicontinuous structures undergo a sequence of spherulization, forming smaller and then larger microspheres. This is consistent with phase separation of the polymer as a liquid that solidifies later.

By deconvoluting micromorphology from other material properties such as density and porosity, it has been experimentally shown that the elastic modulus and thermal conductivity of the gels are directly related to their morphology. Bicontinuous structures are stiffer and exhibit better thermal conductivity compared to structures composed of smaller and larger microspheres. This is attributed to the size of the interparticle neck zones, which are almost as wide as the diameters of the skeletal particles in the bicontinuous morphologies.

APPENDIX A.

SUPPORTING INFORMATION OF PAPER I

The meta-structure is described by a group of 5 parameters (ϕ, c_1, c_2, L_0, N), where ϕ is porosity, c_1 and c_2 are the parameters of a parametric function defined as

$$r(\theta) = r_0[1 + c_1\cos(4\theta) + c_2\cos(8\theta)],$$

in which

$$r_0 = \frac{L_0\sqrt{2\phi}}{\sqrt{\pi\left(2+c_1^2+c_2^2\right)}},$$

that describes the repeating unit cell in polar coordinates. Also, L_0 is the center-to-center distance between neighboring unit cells and N is the number of unit cells repetition. In this work, the five parameters were set to (0.47, 0.11, -0.05, 10 mm, 8) according to Bertoldi's work [SIR-1]. The cross section of the meta-structure is shown in Figure 1.

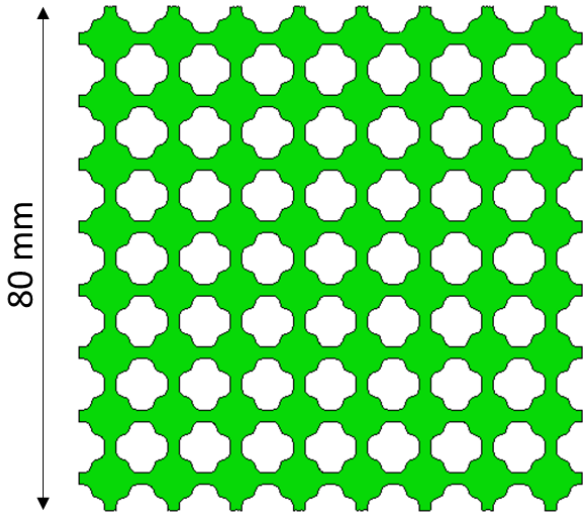

Figure 1. Geometrical details of the meta-structure.

Step 1

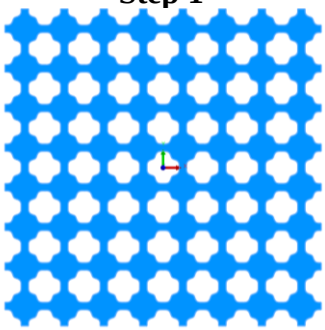

The meta-structure pattern is centered around its midpoint. Dimensions are 80 mm × 80 mm.

Step 2

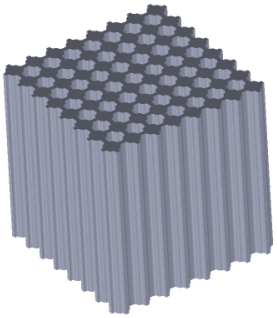

The meta-structure pattern of Step 1 is then expanded in the z-direction by 80 mm.

Step 3

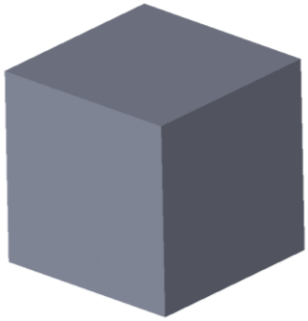

A solid 3D object with dimmesions of 80 mm × 80 mm × 85 mm is formed around the expanded meta-structure of Step 2.

Step 4

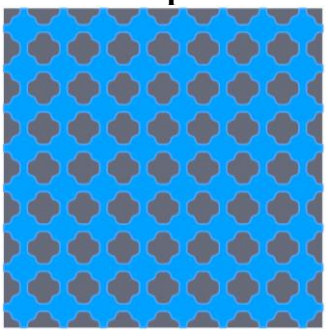

The meta-structure is then selected and subtracted from the volume within the 3D object of Step 3.

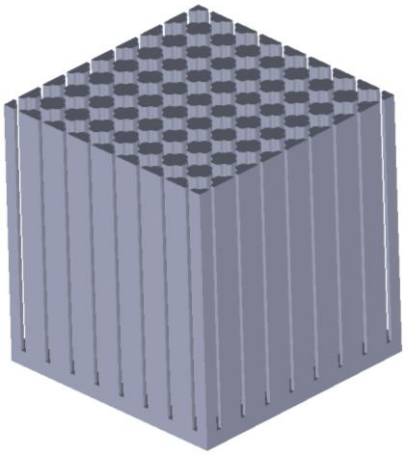

Once the expanded structure of Step 2 is subtracted from the volume of the 3D object of Step 3, we are left with the final mold design that is obviously the negative of the desirable structure of Steps 1 and 2. This mold design is implemented using 3D printing with polylactic acid (PLA).

Figure 2**.** Design steps for the 3D-printed mold.

Table 1. Formulation of PIR-PUR wet gels and aerogels.

Material	Amount
Desmodur N3300A	28.23 g
triethylene glycol (TEG)	13.72 g
acetonitrile (CH_3CN)	207.80 mL
anhydrous $CuCl_2$	5.6 mL from a stock solution consisting of 2.789 g $CuCl_2$ in 250 mL acetonitrile

Total volume of the sol: 250 mL

Density information provided by the suppliers: Desmodur N3300A (Covestro LLC): 1.17 g/cm^3; Triethylene glycol (TEG, Fisher Scientific): 1.10 g/cm^3; Acetonitrile (CH_3CN, Fisher Scientific): 0.79 g/cm^3.

2 Figures of merit of the shape-memory effect of straight and meta PIR-PUR aerogels.

The figures of merit of the shape memory effect include the strain fixity ratio, Rf , a measure of how well a sample retains its temporary shape at a temperature sufficiently lower than Tg, the strain recovery ratio, Rr , a measure that shows a sample's capability to recover its shape by heating from Tlow to Thigh, the recovery rate, Rt, a measure of how fast a sample recovers its shape by heating from Tlow to Thigh, and the fill factor, FF, an evaluator of the overall shape memory capability of a sample. FF depends on all three Rf, Rr and Rt. Rf, Rr and Rt are extracted from the strain-time projections of the 3D plots of Figure 2.2F and Figure 2.4A for the straight and the meta PIR-PUR aerogels, respectively, according to well-established procedures. Those projections are shown in Figures B.3A and B.3B. FFs are extracted from the strain-temperature projections of the 3D plots of Figure 2F and Figure 2.4A for the straight and the meta PIR-PUR aerogels, respectively. Those projections are shown in Figures 3C and 3D. FFs were calculated as

the ratios of the shaded areas underneath the S-shaped strain-versus-temperature curves of Figures 3C and 3D over to the total areas of the rectangles shown around the S-curves.

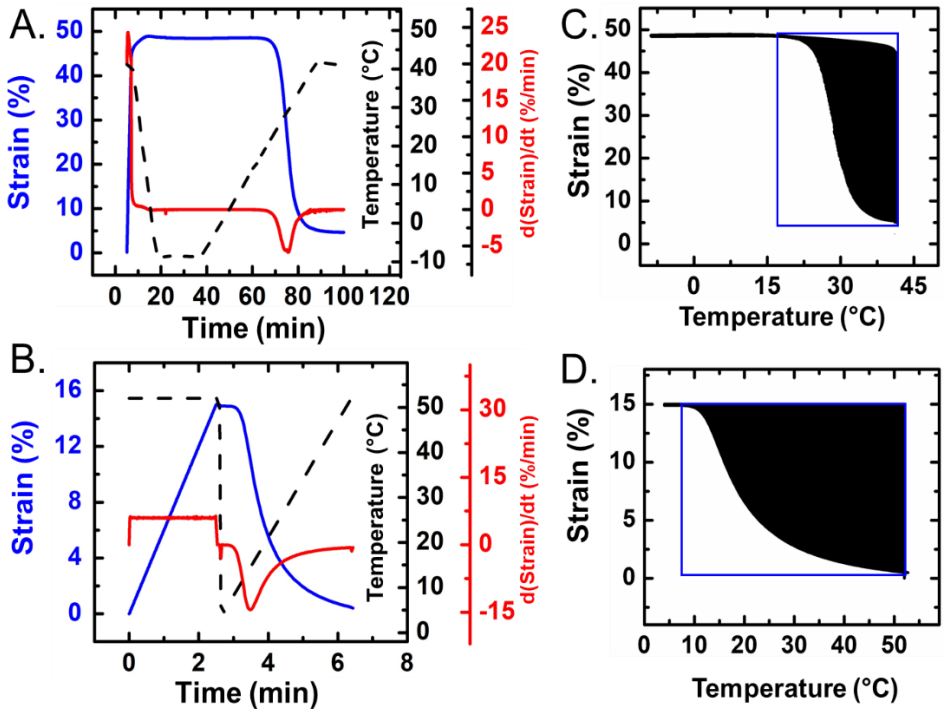

Figure 3. (A) and (B) Strain-temperature projections from 3D plots in Figures 2F (last cycle) and 4A, respectively, followed by unfolding temperature into time. Temperature cycle is shown by a dotted line. Also, the first derivatives of strain vs. time are plotted. (C) and (D) Direct strain-temperature projections from 3D plots in Figures 2.2F (last cycle) and 2.4A, respectively. Fill factors of the PIR-PUR aerogel and meta-aerogel samples were calculated from the ratios of the shaded areas over the entire areas of the surrounding squares and are provided in Table 2.

Table 2. Figures of merit for the evaluation of shape memory capabilities of PIR-PUR aerogel and meta-aerogel samples.

	Strain fixity ratio (%)		**Strain recovery ratio (%)**		**Fill factor**	
Sample (mode)	**Aerogel (tension)**	**Meta-aerogel (compression)**	**Aerogel (tension)**	**Meta-aerogel (compression)**	**Aerogel (tension)**	**Meta-aerogel (compression)**
Cycle 1	98.8	99.3	82.9	97.7	0.58	0.69
Cycle 2	98.8		81.0		0.59	
Cycle 3	98.6		80.2		0.59	
Cycle 4	98.8		79.6		0.59	
Cycle 5	98.8		79.4		0.59	

APPENDIX B.

SUPPORTING INFORMATION OF PAPER II

Appendix B.1: Formulations of all PIR-PUR aerogels with all catalysts and catalyst concentrations.

Table 1. Formulation of TEG and Desmodur N3300A based PIR-PUR aerogels using DBTDL as catalyst.

catalyst formulation	**Desmodur N3300A (g [mmol])**	**TEG (g [mmol])**	**DBTDL used in the reaction**			**acetonitrile used to make the sol**	**total volume of sol[c]**	**[DBTDL] in the sol**	**percent of monomers in the sol[d]**
			volume (μL)	mass[a] (g)	mmol[b]	mL	mL	M	w/w
1×	2.520 [5.00]	1.125 [7.50]	25.0	0.0266	0.0422	18.550	21.719	0.001944	20.00

[a] Calculated using the density of DBTDL (1.066 g cm^{-3}).

[b] Calculated using the molar mass of DBTDL (631.56 g mol^{-1}).

[c] Total volume of the sol = volume of CH_3CN (18.550 mL) + volume of catalyst (0.025 mL) + volume of Desmodur N3300A (2.1428 mL) + volume of TEG (1.0009 mL). The volume of Desmodur N3300A (2.1428 mL) was calculated from its mass (2.250 g) and its density (1.176 g cm^{-3}). The volume of TEG (1.0009 mL) was calculated from its mass (1.125 g) and its density (1.124 g cm^{-3}).

[d] Weight percent of monomers in the sol = 100 × (mass of Desmodur N3300A + mass of TEG)/(mass of Desmodur N3300A + mass of TEG + mass of DBTDL + mass of acetonitrile used to make the sol).

Table 1. Formulation of TEG and Desmodur N3300A based PIR-PUR aerogels using $AlCl_3$ as catalyst (cont.).

catalyst formulation	**Desmodur N3300A (g [mmol])**	**TEG (g [mmol])**	**stock solution of $AlCl_3$ in acetonitrile**				**catalyst stock solution used in the reaction**		**volume of acetonitrile used to make the sol**	**total volume of sol[a]**	**[$AlCl_3$] in the sol**	**percent of monomers in the sol[b]**
			mass of salt (g)	mol of salt	volume of solvent (mL)	[$AlCl_3$] (M)	volume (µL)	mmol	mL	mL	M	w/w
$AlCl_3$												
1/4×	2.520 [5.00]	1.125 [7.50]	2.766	0.0207	250	0.0828	125	0.0104	18.425	21.6938	0.000477	20.00
1/2×	2.520 [5.00]	1.125 [7.50]	2.766	0.0207	250	0.0828	250	0.0207	18.300	21.6938	0.000954	20.00
1×	2.520 [5.00]	1.125 [7.50]	2.766	0.0207	250	0.0828	500	0.0414	18.050	21.6938	0.001908	19.99
2×	2.520 [5.00]	1.125 [7.50]	2.766	0.0207	250	0.0828	1000	0.0828	17.550	21.6938	0.003816	19.99
4×	2.520 [5.00]	1.125 [7.50]	2.766	0.0207	250	0.0828	2000	0.1656	16.550	21.6938	0.007633	19.98

[a] Total volume of the sol = volume of acetonitrile + volume of catalyst stock solution + volume of Desmodur N3300A + volume of TEG. The volume of Desmodur N3300A (2.1428 mL) was calculated from its mass (2.250 g) and its density (1.176 g cm^{-3}). The volume of TEG (1.0009 mL) was calculated from its mass (1.125 g) and its density (1.124 g cm^{-3}).[b] Weight percent of monomers in the sol = 100 × (mass of Desmodur N3300A + mass of TEG)/(mass of Desmodur N3300A + mass of TEG + mass of acetonitrile used in stock solution + mass of acetonitrile used to make the sol + mass of the catalyst in the volume of the stock solution). The density of acetonitrile is 0.786 g cm^{-3}.

Table 1. Formulation of TEG and Desmodur N3300A based PIR-PUR aerogels using $BICl_3$ as catalyst (cont.).

catalyst formulation	**Desmodur N3300A (g [mmol])**	**TEG (g [mmol])**	**Solution of $BiCl_3$ in acetonitrile[a]**				**catalyst stock solution used in the reaction**		**volume of acetonitrile used to make the sol**	**total volume of sol[b]**	**[$BiCl_3$] in the sol**	**percent of monomers in the sol[c]**
			mass of salt (g)	mol of salt	volume of solvent (mL)	[$BiCl_3$] (M)	volume (µL)	mmol	mL	mL	M	w/w
$BiCl_3$												
1×	2.520 [5.00]	1.125 [7.50]	0.6543	0.0021	100	0.0207	2000	0.0414	16.550	21.6938	0.001908	20.00

[a] Weighted together with TEG is the same flask and was dissolved together with TEG in the same portion of acetonitrile.

[b] Total volume of the sol = volume of acetonitrile + volume of catalyst stock solution + volume of Desmodur N3300A + volume of TEG. The volume of Desmodur N3300A (2.1428 mL) was calculated from its mass (2.250 g) and its density (1.176 g cm^{-3}). The volume of TEG (1.0009 mL) was calculated from its mass (1.125 g) and its density (1.124 g cm^{-3}).

[c] Weight percent of monomers in the sol = 100 × (mass of Desmodur N3300A + mass of TEG)/(mass of Desmodur N3300A + mass of TEG + mass of acetonitrile used in stock solution + mass of acetonitrile used to make the sol + mass of the catalyst in the volume of the stock solution). The density of acetonitrile is 0.786 g cm^{-3}.

Table 1. Formulation of TEG and Desmodur N3300A based PIR-PUR aerogels using $Cd(NO_3)_2$ as catalyst (cont.).

catalyst formulation	**Desmodur N3300A (g [mmol])**	**TEG (g [mmol])**	**solution of $Cd(NO_3)_2$ in acetonitrile[a]**				**catalyst stock solution used in the reaction**		**volume of acetonitrile used to make the sol**	**total volume of sol[b]**	**$[Cd(NO_3)_2]$ in the sol**	**percent of monomers in the sol[c]**
			mass of salt (g)	mol of salt	volume of solvent (mL)	$[Cd(NO_3)_2]$ (M)	volume (µL)	mmol	mL	mL	M	w/w
$Cd(NO_3)_2$												
1×	2.520 [5.00]	1.125 [7.50]	0.64	0.0021	100	0.0207	2000	0.0414	16.550	21.6938	0.001908	20.00

[a] Weighted together with TEG is the same flask and was dissolved together with TEG in the same portion of acetonitrile. [b] Total volume of the sol = volume of acetonitrile + volume of catalyst stock solution + volume of Desmodur N3300A + volume of TEG. The volume of Desmodur N3300A (2.1428 mL) was calculated from its mass (2.250 g) and its density (1.176 g cm^{-3}). The volume of TEG (1.0009 mL) was calculated from its mass (1.125 g) and its density (1.124 g cm^{-3}). [c] Weight percent of monomers in the sol = 100 × (mass of Desmodur N3300A + mass of TEG)/(mass of Desmodur N3300A + mass of TEG + mass of acetonitrile used in stock solution + mass of acetonitrile used to make the sol + mass of the catalyst in the volume of the stock solution). The density of acetonitrile is 0.78 gcm^{-3}.

Table 1. Formulation of TEG and Desmodur N3300A based PIR-PUR aerogels using $CoCl_2$ as catalyst (cont.).

catalyst formulation	**Desmodur N3300A (g [mmol])**	**TEG (g [mmol])**	**stock solution of $CoCl_2$ in acetonitrile**				**catalyst stock solution used in the reaction**		**volume of acetonitrile used to make the sol**	**total volume of sol[a]**	**[$CoCl_2$] in the sol**	**percent of monomers in the sol[b]**
			mass of salt (g)	mol of salt	volume of solvent (mL)	[$CoCl_2$] (M)	volume (µL)	mmol	mL	mL	M	w/w
$CoCl_2$												
1/3×	2.520 [5.00]	1.125 [7.50]	3.429	0.0207	250	0.0828	167	0.0138	18.383	21.6938	0.000636	20.00
1/2×	2.520 [5.00]	1.125 [7.50]	3.429	0.0207	250	0.0828	250	0.0207	18.300	21.6938	0.000954	20.00
1×	2.520 [5.00]	1.125 [7.50]	3.429	0.0207	250	0.0828	500	0.0414	18.050	21.6938	0.001908	19.99
2×	2.520 [5.00]	1.125 [7.50]	3.429	0.0207	250	0.0828	1000	0.0828	17.550	21.6938	0.003816	19.99
4×	2.520 [5.00]	1.125 [7.50]	3.429	0.0207	250	0.0828	2000	0.1656	16.550	21.6938	0.007633	19.98

[a] Total volume of the sol = volume of acetonitrile + volume of catalyst stock solution + volume of Desmodur N3300A + volume of TEG. The volume of Desmodur N3300A (2.1428 mL) was calculated from its mass (2.250 g) and its density (1.176 g cm^{-3}). The volume of TEG (1.0009 mL) was calculated from its mass (1.125 g) and its density (1.124 g cm^{-3}). [b] Weight percent of monomers in the sol = 100 × (mass of Desmodur N3300A + mass of TEG)/(mass of Desmodur N3300A + mass of TEG + mass of acetonitrile used in stock solution + mass of acetonitrile used to make the sol + mass of the catalyst in the volume of the stock solution). The density of acetonitrile is 0.786 g cm^{-3}.

Table 1. Formulation of TEG and Desmodur N3300A based PIR-PUR aerogels using Cu_2Cl_2 as catalyst (cont.).

catalyst formulation	**Desmodur N3300A (g [mmol])**	**TEG (g [mmol])**	**stock solution of Cu_2Cl_2 in acetonitrile**				**catalyst stock solution used in the reaction**		**volume of acetonitrile used to make the sol**	**total volume of sol[a]**	**$[Cu_2Cl_2]$ in the sol**	**percent of monomers in the sol[b]**
			mass of salt (g)	mol of salt	volume of solvent (mL)	$[Cu_2Cl_2]$ (M)	volume (µL)	mmol	mL	mL	M	w/w
Cu_2Cl_2												
1/8×	2.520 [5.00]	1.125 [7.50]	4.108	0.0207	250	0.0828	63	0.0052	18.488	21.6938	0.000239	20.00
1/6×	2.520 [5.00]	1.125 [7.50]	4.108	0.0207	250	0.0828	83	0.0069	18.467	21.6938	0.000318	20.00
1/4×	2.520 [5.00]	1.125 [7.50]	4.108	0.0207	250	0.0828	125	0.0103	18.425	21.6938	0.000477	20.00
1/3×	2.520 [5.00]	1.125 [7.50]	4.108	0.0207	250	0.0828	167	0.0138	18.383	21.6938	0.000636	20.00
1/2×	2.520 [5.00]	1.125 [7.50]	4.108	0.0207	250	0.0828	250	0.0207	18.300	21.6938	0.000954	20.00
1×	2.520 [5.00]	1.125 [7.50]	4.108	0.0207	250	0.0828	500	0.0414	18.050	21.6938	0.001908	20.00
4×	2.520 [5.00]	1.125 [7.50]	4.108	0.0207	250	0.0828	2000	0.1656	16.550	21.6938	0.007633	19.98

[a] Total volume of the sol = volume of acetonitrile + volume of catalyst stock solution + volume of Desmodur N3300A + volume of TEG. The volume of Desmodur N3300A (2.1428 mL) was calculated from its mass (2.250 g) and its density (1.176 g cm^{-3}). The volume of TEG (1.0009 mL) was calculated from its mass (1.125 g) and its density (1.124 g cm^{-3}).[b] Weight percent of monomers in the sol = 100 × (mass of Desmodur N3300A + mass of TEG)/(mass of Desmodur N3300A + mass of TEG + mass of acetonitrile used in stock solution + mass of acetonitrile used to make the sol + mass of the catalyst in the volume of the stock solution). The density of acetonitrile is 0.786 g cm^{-3}.

Table 1. Formulation of TEG and Desmodur N3300A based PIR-PUR aerogels using $CuCl_2$ as catalyst (cont.).

catalyst formulation	**Desmodur N3300A (g [mmol])**	**TEG (g [mmol])**	**stock solution of $CuCl_2$ in acetonitrile**				**catalyst stock solution used in the reaction**		**volume of acetonitrile used to make the sol**	**total volume of sol[a]**	**[$CuCl_2$] in the sol**	**percent of monomers in the sol[b]**
			mass of salt (g)	mol of salt	volume of solvent (mL)	[$CuCl_2$] (M)	volume (µL)	mmol	mL	mL	M	mass of salt (g)
$CuCl_2$												
6×	2.520 [5.00]	1.125 [7.50]	2.789	0.0207	250	0.0828	4000	0.2484	14.550	21.6938	0.011450	19.96
4×	2.520 [5.00]	1.125 [7.50]	2.789	0.0207	250	0.0828	2000	0.1656	16.550	21.6938	0.007633	19.98
2×	2.520 [5.00]	1.125 [7.50]	2.789	0.0207	250	0.0828	1000	0.0207	17.550	21.6938	0.000954	20.00
1×	2.520 [5.00]	1.125 [7.50]	2.789	0.0207	250	0.0828	500	0.0414	18.050	21.6938	0.001908	19.99
1/8×	2.520 [5.00]	1.125 [7.50]	2.789	0.0207	250	0.0828	62.5	0.0052	18.488	21.6938	0.000239	20.00

[a] Total volume of the sol = volume of acetonitrile + volume of catalyst stock solution + volume of Desmodur N3300A + volume of TEG. The volume of Desmodur N3300A (2.1428 mL) was calculated from its mass (2.250 g) and its density (1.176 g cm^{-3}). The volume of TEG (1.0009 mL) was calculated from its mass (1.125 g) and its density (1.124 g cm^{-3}).[b] Weight percent of monomers in the sol = 100 × (mass of Desmodur N3300A + mass of TEG)/(mass of Desmodur N3300A + mass of TEG + mass of acetonitrile used in stock solution + mass of acetonitrile used to make the sol + mass of the catalyst in the volume of the stock solution). The density of acetonitrile is 0.786 g cm^{-3}.

Table 1. Formulation of TEG and Desmodur N3300A based PIR-PUR aerogels using $CuCl_2$ as catalyst (cont.).

catalyst formulation	**Desmodur N3300A (g [mmol])**	**TEG (g [mmol])**	**stock solution of $CuCl_2$ in acetonitrile**				**catalyst stock solution used in the reaction**		**volume of acetonitrile used to make the sol**	**total volume of sol[a]**	**[$CuCl_2$] in the sol**	**percent of monomers in the sol[b]**
			mass of salt (g)	mol of salt	volume of solvent (mL)	[$CuCl_2$] (M)	volume (µL)	mmol	mL	mL	M	mass of salt (g)
$CuCl_2$												
1/10×	2.520 [5.00]	1.125 [7.50]	1.395	0.0104	250	0.0414	100.0	0.0041	18.455	21.6938	0.000190	20.00
1/13×	2.520 [5.00]	1.125 [7.50]	1.395	0.0104	250	0.0414	76.9	0.0032	18.473	21.6938	0.000147	20.00
1/16×	2.520 [5.00]	1.125 [7.50]	1.395	0.0104	250	0.0414	62.5	0.0026	18.488	21.6938	0.000119	20.00
1/20×	2.520 [5.00]	1.125 [7.50]	1.395	0.0104	250	0.0414	50.0	0.0021	18.500	21.6938	0.000095	20.00
1/26×	2.520 [5.00]	1.125 [7.50]	1.395	0.0104	250	0.0414	76.9	0.0016	18.473	21.6938	0.000073	20.00
1/32×	2.520 [5.00]	1.125 [7.50]	1.395	0.0104	250	0.0414	38.5	0.0013	18.512	21.6938	0.000059	20.00

[a] Total volume of the sol = volume of acetonitrile + volume of catalyst stock solution + volume of Desmodur N3300A + volume of TEG. The volume of Desmodur N3300A (2.1428 mL) was calculated from its mass (2.250 g) and its density (1.176 g cm^{-3}). The volume of TEG (1.0009 mL) was calculated from its mass (1.125 g) and its density (1.124 g cm^{-3}).

[b] Weight percent of monomers in the sol = 100 × (mass of Desmodur N3300A + mass of TEG)/(mass of Desmodur N3300A + mass of TEG + mass of acetonitrile used in stock solution + mass of acetonitrile used to make the sol + mass of the catalyst in the volume of the stock solution). The density of acetonitrile is 0.786 g cm^{-3}.

Table 1. Formulation of TEG and Desmodur N3300A based PIR-PUR aerogels using $FeCl_3$ as catalyst (cont.).

catalyst formulation	**Desmodur N3300A (g [mmol])**	**TEG (g [mmol])**	**stock solution of $FeCl_3$ in acetonitrile**				**catalyst stock solution used in the reaction**		**volume of acetonitrile used to make the sol**	**total volume of sol[a]**	**[$FeCl_3$] in the sol**	**percent of monomers in the sol[b]**
			mass of salt (g)	mol of salt	volume of solvent (mL)	[$FeCl_3$] (M)	volume (µL)	mmol	mL	mL	M	w/w
$FeCl_3$												
1×	2.520 [5.00]	1.125 [7.50]	3.366	0.0207	250	0.0828	500	0.0414	18.050	21.6938	0.001908	19.99
2×	2.520 [5.00]	1.125 [7.50]	3.366	0.0207	250	0.0828	1000	0.0828	17.550	21.6938	0.003817	19.98
4×	2.520 [5.00]	1.125 [7.50]	3.366	0.0207	250	0.0828	2000	0.1656	16.550	21.6938	0.007634	19.97
5×	2.520 [5.00]	1.125 [7.50]	3.366	0.0207	250	0.0828	2500	0.2070	16.050	21.6938	0.009542	19.96
8×	2.520 [5.00]	1.125 [7.50]	3.366	0.0207	250	0.0828	4000	0.3312	14.550	21.6938	0.015267	19.94
10×	2.520 [5.00]	1.125 [7.50]	6.732	0.0415	100	0.4140	1000	0.4140	17.550	21.6938	0.019084	19.93
16×	2.520 [5.00]	1.125 [7.50]	6.732	0.0415	100	0.4140	1600	0.6624	16.950	21.6938	0.030534	19.88

[a] Total volume of the sol = volume of acetonitrile + volume of catalyst stock solution + volume of Desmodur N3300A + volume of TEG. The volume of Desmodur N3300A (2.1428 mL) was calculated from its mass (2.250 g) and its density (1.176 g cm^{-3}). The volume of TEG (1.0009 mL) was calculated from its mass (1.125 g) and its density (1.124 g cm^{-3}).[b] Weight percent of monomers in the sol = 100 × (mass of Desmodur N3300A + mass of TEG)/(mass of Desmodur N3300A + mass of TEG + mass of acetonitrile used in stock solution + mass of acetonitrile used to make the sol + mass of the catalyst in the volume of the stock solution). The density of acetonitrile is 0.786 g cm^{-3}.

Table 1. Formulation of TEG and Desmodur N3300A based PIR-PUR aerogels using $GaCl_3$ as catalyst (cont.).

catalyst formulation	**Desmodur N3300A (g [mmol])**	**TEG (g [mmol])**	**stock solution of $GaCl_3$ in acetonitrile**				**catalyst stock solution used in the reaction**		**volume of acetonitrile used to make the sol**	**total volume of sol[a]**	**[$GaCl_3$] in the sol**	**percent of monomers in the sol[b]**
			mass of salt (g)	mol of salt	volume of solvent (mL)	[$GaCl_3$] (M)	volume (μL)	mmol	mL	mL	M	w/w
$GaCl_3$												
1×	2.520 [5.00]	1.125 [7.50]	1.461	0.0083	100	0.0829	500	0.0414	18.050	21.6938	0.001908	20.00
6×	2.520 [5.00]	1.125 [7.50]	1.461	0.0083	100	0.0829	3000	0.2484	15.550	21.6938	0.011450	20.00
8×	2.520 [5.00]	1.125 [7.50]	1.461	0.0083	100	0.0829	4000	0.3312	14.550	21.6938	0.015267	20.00
9×	2.520 [5.00]	1.125 [7.50]	1.461	0.0083	100	0.0829	4500	0.3726	14.050	21.6938	0.017175	20.00
10×	2.520 [5.00]	1.125 [7.50]	1.461	0.0083	100	0.0829	5000	0.4140	13.550	21.6938	0.019084	20.00
16×	2.520 [5.00]	1.125 [7.50]	1.461	0.0083	100	0.0829	8000	0.6624	10.550	21.6938	0.030534	20.00

[a] Total volume of the sol = volume of acetonitrile + volume of catalyst stock solution + volume of Desmodur N3300A + volume of TEG. The volume of Desmodur N3300A (2.1428 mL) was calculated from its mass (2.250 g) and its density (1.176 g cm^{-3}). The volume of TEG (1.0009 mL) was calculated from its mass (1.125 g) and its density (1.124 g cm^{-3}). [b] Weight percent of monomers in the sol = 100 × (mass of Desmodur N3300A + mass of TEG)/(mass of Desmodur N3300A + mass of TEG + mass of acetonitrile used in stock solution + mass of acetonitrile used to make the sol + mass of the catalyst in the volume of the stock solution). The density of acetonitrile is 0.786 g cm^{-3}.

Table 1. Formulation of TEG and Desmodur N3300A based PIR-PUR aerogels using $InCl_3$ as catalyst (cont.).

catalyst formulation	**Desmodur N3300A (g [mmol])**	**TEG (g [mmol])**	**stock solution of $InCl_3$ in acetonitrile**				**catalyst stock solution used in the reaction**		**volume of acetonitrile used to make the sol**	**total volume of sol[a]**	**[$InCl_3$] in the sol**	**percent of monomers in the sol[b]**
			mass of salt (g)	mol of salt	volume of solvent (mL)	[$InCl_3$] (M)	volume (µL)	mmol	mL	mL	M	w/w
$InCl_3$												
1/8×	2.520 [5.00]	1.125 [7.50]	4.589	0.0207	250	0.0828	62.5	0.0052	18.488	21.6938	0.000239	20.00
1/4×	2.520 [5.00]	1.125 [7.50]	4.589	0.0207	250	0.0828	125	0.0104	18.425	21.6938	0.000477	20.00
1/2×	2.520 [5.00]	1.125 [7.50]	4.589	0.0207	250	0.0828	250	0.0207	18.300	21.6938	0.000954	19.99
1×	2.520 [5.00]	1.125 [7.50]	4.589	0.0207	250	0.0828	500	0.0414	18.050	21.6938	0.001908	19.99
2×	2.520 [5.00]	1.125 [7.50]	4.589	0.0207	250	0.0828	1000	0.0828	17.550	21.6938	0.003817	19.98

[a] Total volume of the sol = volume of acetonitrile + volume of catalyst stock solution + volume of Desmodur N3300A + volume of TEG. The volume of Desmodur N3300A (2.1428 mL) was calculated from its mass (2.250 g) and its density (1.176 g cm^{-3}). The volume of TEG (1.0009 mL) was calculated from its mass (1.125 g) and its density (1.124 g cm^{-3}). [b] Weight percent monomers in the sol = 100 × (mass of Desmodur N3300A + mass of TEG)/(mass of Desmodur N3300A + mass of TEG + mass of acetonitrile used in stock solution + mass of acetonitrile used to make the sol + mass of the catalyst in the volume of the stock solution). The density of acetonitrile is 0.786 g cm^{-3}.

Table 1. Formulation of TEG and Desmodur N3300A based PIR-PUR aerogels using $Ni(OTf)_2$ as catalyst (cont.).

catalyst formulation	**Desmodur N3300A (g [mmol])**	**TEG (g [mmol])**	**stock solution of $Ni(OTf)_2$ in acetonitrile**				**catalyst stock solution used in the reaction**		**volume of acetonitrile used to make the sol**	**total volume of sol[a]**	**$[Ni(OTf)_2]$ in the sol**	**percent of monomers in the sol[b]**
			mass of salt (g)	mol of salt	volume of solvent (mL)	$[Ni(OTf)_2]$ (M)	volume (µL)	mmol	mL	mL	M	w/w
$Ni(OTf)_2$												
1×	2.520 [5.00]	1.125 [7.50]	7.404	0.0207	250	0.0828	500	0.0414	18.050	21.6938	0.001908	19.98
2×	2.520 [5.00]	1.125 [7.50]	7.404	0.0207	250	0.0828	1000	0.0828	17.550	21.6938	0.003817	19.97
4×	2.520 [5.00]	1.125 [7.50]	7.404	0.0207	250	0.0828	2000	0.1656	16.550	21.6938	0.007634	19.94
16×	2.520 [5.00]	1.125 [7.50]	7.404	0.0207	250	0.0828	4000	0.6624	14.550	21.6938	0.030534	19.74

[a] Total volume of the sol = volume of acetonitrile + volume of catalyst stock solution + volume of Desmodur N3300A + volume of TEG. The volume of Desmodur N3300A (2.1428 mL) was calculated from its mass (2.250 g) and its density (1.176 g cm^{-3}). The volume of TEG (1.0009 mL) was calculated from its mass (1.125 g) and its density (1.124 g cm^{-3}).[b] Weight percent of monomers in the sol = 100 × (mass of Desmodur N3300A + mass of TEG)/(mass of Desmodur N3300A + mass of TEG + mass of acetonitrile used in stock solution + mass of acetonitrile used to make the sol + mass of the catalyst in the volume of the stock solution). The density of acetonitrile is 0.786 g cm^{-3}.

Table 1. Formulation of TEG and Desmodur N3300A based PIR-PUR aerogels using $SnCl_4$ as catalyst (cont.).

catalyst formulation	**Desmodur N3300A (g [mmol])**	**TEG (g [mmol])**	**stock solution of $SnCl_4$ in acetonitrile**				**catalyst stock solution used in the reaction**		**volume of acetonitrile used to make the sol**	**total volume of sol[a]**	**[$SnCl_4$] in the sol**	**percent of monomers in the sol[b]**
			mass of salt (g)	mol of salt	volume of solvent (mL)	[$SnCl_4$] (M)	volume (µL)	mmol	mL	mL	M	w/w
$SnCl_4$												
1/4×	2.520 [5.00]	1.125 [7.50]	5.405	0.0207	250	0.0828	125	0.0104	18.425	21.6938	0.000478	20.00
1/2×	2.520 [5.00]	1.125 [7.50]	5.405	0.0207	250	0.0828	250	0.0207	18.300	21.6938	0.000954	19.99
1×	2.520 [5.00]	1.125 [7.50]	5.405	0.0207	250	0.0828	500	0.0414	18.050	21.6938	0.001908	19.99
2×	2.520 [5.00]	1.125 [7.50]	5.405	0.0207	250	0.0828	1000	0.0828	17.550	21.6938	0.003817	19.98
4×	2.520 [5.00]	1.125 [7.50]	5.405	0.0207	250	0.0828	2000	0.1656	16.550	21.6938	0.007633	19.95

[a] Total volume of the sol = volume of acetonitrile + volume of catalyst stock solution + volume of Desmodur N3300A + volume of TEG. The volume of Desmodur N3300A (2.1428 mL) was calculated from its mass (2.250 g) and its density (1.176 g cm^{-3}). The volume of TEG (1.0009 mL) was calculated from its mass (1.125 g) and its density (1.124 g cm^{-3}).[b] Weight percent of monomers in the sol = 100 × (mass of Desmodur N3300A + mass of TEG)/(mass of Desmodur N3300A + mass of TEG + mass of acetonitrile used in stock solution + mass of acetonitrile used to make the sol + mass of the catalyst in the volume of the stock solution). The density of acetonitrile is 0.786 g cm^{-3}.

Table 1. Formulation of TEG and Desmodur N3300A based PIR-PUR aerogels using $Tl(NO_3)_3$ as catalyst (cont.).

catalyst formulation	**Desmodur N3300A (g [mmol])**	**TEG (g [mmol])**	**solution of $Tl(NO_3)_3$ in acetonitrile[a]**				**catalyst stock solution used in the reaction**		**volume of acetonitrile used to make the sol**	**total volume of sol[b]**	**$[Tl(NO_3)_3]$ in the sol**	**percent of monomers in the sol[c]**
			mass of salt (g)	mol of salt	volume of solvent (mL)	$[Tl(NO_3)_3]$ (M)	volume (μL)	mmol	mL	mL	M	w/w
$Tl(NO_3)_3$												
1×	2.520 [5.00]	1.125 [7.50]	0.2774	0.001	25	0.041	1000	0.0414	17.550	21.6938	0.001908	20.00

[a] Weighted together with TEG is the same flask and was dissolved together with TEG in the same portion of acetonitrile.

[b] Total volume of the sol = volume of acetonitrile + volume of catalyst stock solution + volume of Desmodur N3300A + volume of TEG. The volume of Desmodur N3300A (2.1428 mL) was calculated from its mass (2.250 g) and its density (1.176 g cm^{-3}). The volume of TEG (1.0009 mL) was calculated from its mass (1.125 g) and its density (1.124 g cm^{-3}).

[c] Weight percent of monomers in the sol = 100 × (mass of Desmodur N3300A + mass of TEG)/(mass of Desmodur N3300A + mass of TEG + mass of acetonitrile used in stock solution + mass of acetonitrile used to make the sol + mass of the catalyst in the volume of the stock solution). The density of acetonitrile is 0.786 g cm^{-3}.

Table 1. Formulation of TEG and Desmodur N3300A based PIR-PUR aerogels using $ZnCl_2$ as catalyst (cont.).

catalyst formulation	**Desmodur N3300A (g [mmol])**	**TEG (g [mmol])**	**stock solution of $ZnCl_2$ in acetonitrile**				**catalyst stock solution used in the reaction**		**volume of acetonitrile used to make the sol**	**total volume of sol[a]**	**[$ZnCl_2$] in the sol**	**percent of monomers in the sol[b]**
			mass of salt (g)	mol of salt	volume of solvent (mL)	[$ZnCl_2$] (M)	volume (µL)	mmol	mL	mL	M	w/w
$ZnCl_2$												
1×	2.520 [5.00]	1.125 [7.50]	2.828	0.0207	250	0.0828	500	0.0414	18.050	21.6938	0.001908	19.99
2×	2.520 [5.00]	1.125 [7.50]	2.828	0.0207	250	0.0828	1000	0.0828	17.550	21.6938	0.003817	19.99
4×	2.520 [5.00]	1.125 [7.50]	2.828	0.0207	250	0.0828	2000	0.1656	16.550	21.6938	0.007634	19.97
8×	2.520 [5.00]	1.125 [7.50]	2.828	0.0207	250	0.0828	4000	0.3312	14.550	21.6938	0.015267	19.95
16×	2.520 [5.00]	1.125 [7.50]	2.828	0.0207	250	0.0828	8000	0.6624	10.550	21.6938	0.030534	19.90

[a] Total volume of the sol = volume of acetonitrile + volume of catalyst stock solution + volume of Desmodur N3300A + volume of TEG. The volume of Desmodur N3300A (2.1428 mL) was calculated from its mass (2.250 g) and its density (1.176 g cm^{-3}). The volume of TEG (1.0009 mL) was calculated from its mass (1.125 g) and its density (1.124 g cm^{-3}).[b] Weight percent of monomers in the sol = 100 × (mass of Desmodur N3300A + mass of TEG)/(mass of Desmodur N3300A + mass of TEG + mass of acetonitrile used in stock solution + mass of acetonitrile used to make the sol + mass of the catalyst in the volume of the stock solution). The density of acetonitrile is 0.786 g cm^{-3}.

Appendix B.2: General Properties of PIR-PUR aerogels with all catalysts and their concentrations.

Table 1. General material properties and gelation times of metal catalyzed PIR-PUR aerogels.

catalyst formulation	gelation time (min)		linear shrinkage (%)[a,b]	bulk density, ρ_b (g cm^{-3})[a]	skeletal density, ρ_s (g cm^{-3})[c]	porosity, Π (% v/v)[d]	BET surface area, σ (m^2 g^{-1})	skeletal particle diameter (μm)[e]
	phenomenological	rheological						
DBTDL								
1×	31 ± 1	82	23.9 ± 0.5	0.325 ± 0.003	1.208 ± 0.001	73.1	0.281 ± 0.015	*f*
$AlCl_3$								
4×	4 ± 1	*f*	35.4 ± 0.7	0.392 ± 0.044	1.240 ± 0.004	68.4	*f*	0.563 ± 0.069
1×	63 ± 3	*f*	34.1 ± 0.9	0.332 ± 0.009	1.226 ± 0.003	72.9	*f*	1.250 ± 0.098
1/2×	120 ± 3	*f*	23.3 ± 1.4	0.291 ± 0.011	1.220 ± 0.004	76.1	*f*	2.180 ± 0.147
1/4×	160 ± 9	*f*	22.2 ± 0.98	0.286 ± 0.023	1.216 ± 0.001	76.4	*f*	2.875 ± 0.189
$CoCl_2$								
16×	10 ± 0.6	19	37.2 ± 0.7	0.377 ± 0.010	1.249 ± 0.001	69.8	f	*f*
4×	23 ± 0.5	34	31.8 ± 1.3	0.353 ± 0.027	1.226 ± 0.001	71.2	f	3.242 ± 0.287
2×	34 ± 1	40	27.7 ± 0.7	0.338 ± 0.011	1.222 ± 0.001	72.3	0.009 ± 0.005	4.176 ± 0.305
1×	46 ± 1	63	30.4 ± 0.5	0.379 ± 0.004	1.218 ± 0.001	68.9	*f*	
1/2×	60 ± 1	100	26.5 ± 2.1	0.337 ± 0.019	1.220 ± 0.000$_4$	72.4	0.175 ± 0.032	6.415 ± 0.926
1/3×	91 ± 1	140	28.9 ± 1.2	0.355 ± 0.020	1.213 ± 0.001	70.7	0.144 ± 0.011	11.208 ± 2.425
Cu_2Cl_2								
4×	19 ± 2	*f*	29.4 ± 0.1	0.391 ± 0.004	1.229 ± 0.001	68.2	*f*	*f*
1/2×	53 ± 8	74	26.5 ± 1.3	0.341 ± 0.028	1.207 ± 0.001	71.7	*f*	5.206 ± 1.090
1/3×	63 ± 3	136	26.2 ± 0.8	0.334 ± 0.021	1.206 ± 0.001	72.3	*f*	2.919 ± 0.146
1/4×	89 ± 4	159	25.3 ± 1.2	0.333 ± 0.009	1.205 ± 0.001	72.4	*f*	11.209 ± 3.552
1/6×	144 ± 12	191	23.9 ± 0.6	0.326 ± 0.004	1.205 ± 0.001	72.9	*f*	8.090 ± 2.382
8×	217	*f*	23.6 ± 0.5	0.323 ± 0.004	1.203 ± 0.001	73.2	*f*	*f*

Table 1. General material properties and gelation times of metal catalyzed PIR-PUR aerogels (cont.).

catalyst formulation	gelation time (min)		linear shrinkage (%)[a,b]	bulk density, ρ_b (g cm^{-3})[a]	skeletal density, r_s (g cm^{-3})[c]	porosity, P (% v/v)[d]	BET surface area, σ (m^2 g^{-1})	skeletal particle diameter (μm)[e]
	phenomenological[a]	rheological						
$CuCl_2$								
6×	4 ± 0.8	[f]	20.2 ± 1.3	0.381 ± 0.061	1.253 ± 0.003	69.6	[f]	[f]
4×	4 ± 0.5	[f]	31.3 ± 0.7	0.422 ± 0.008	1.219 ± 0.001	65.4	1.281 ± 0.019	0.734 ± 0.132
2×	5 ± 0.5	[f]	21.3 ± 0.9	0.483 ± 0.061	1.235 ± 0.001	60.9	0.473 ± 0.028	0.921 ± 0.129
1×	5 ± 0.8	9	28.0 ± 0.2	0.387 ± 0.007	1.226 ± 0.001	68.4	1.278 ± 0.016	1.161 ± 0.111
1/8×	19 ± 2	57	24.5 ± 0.4	0.326 ± 0.003	1.232 ± 0.002	73.5	1.294 ± 0.019	1.660 ± 0.340
1/10×	35	[f]	[f]	[f]	[f]	[f]	[f]	[f]
1/20×	53 ± 7	124	21.4 ± 0.4	0.309 ± 0.009	1.233 ± 0.008	74.9	0.104 ± 0.185	4.559 ± 0.714
1/26×	60 ± 18	158	20.8	0.299	1.237 ± 0.007	75.8	0.063 ± 0.087	6.212 ± 1.092
1/32×	95 ± 25	[f]	22.6	0.344	1.209 ± 0.005	71.5	[f]	[f]
$FeCl_3$								
16×	3 ± 0.1	[f]	28.2 ± 0.3	0.367 ± 0.002	1.207 ± 0.001	69.6	0.841 ± 0.018	1.180 ± 0.192
10×	16 ± 1	29	25.4 ± 1.1	0.336 ± 0.023	1.207 ± 0.001	72.2	0.552 ± 0.017	7.320 ± 0.968
8×	25 ± 4	[f]	23.6 ± 1.0	0.310 ± 0.007	1.235 ± 0.001	74.9	[f]	2.789 ± 0.228
2×	104 ±16	172	25.8 ± 0.4	0.319 ± 0.009	1.216 ± 0.003	73.8	[f]	[f]
1×	232 ± 8	303	23.1 ± 1.4	0.323 ± 0.015	1.206 ± 0.001	73.2	0.166 ± 0.012	7.680 ± 1.459

[a] Average of five samples unless no error is indicated. [b] Shrinkage = 100 × (mold diameter − sample diameter)/(mold diameter). [c] Single sample, average of 50 measurements. [d] Calculated as $P = 100\times(r_s\text{-}r_b)/r_s$. [e] From SEM using ImageJ. Average of five particles. [f] Not measured.

Table 1. General material properties and gelation times of metal catalyzed PIR-PUR aerogels (cont.).

catalyst formulation	gelation time (min)		linear shrinkage (%)[a,b]	bulk density, ρ_b (g cm^{-3})[a]	skeletal density, ρ_s (g cm^{-3})[c]	porosity, Π (% v/v)[d]	BET surface area, σ (m^2 g^{-1})	skeletal particle diameter (μm)[e]
	phenomenological[a]	rheological						
$GaCl_3$								
16×	2 ± 0.1	[f]	36.9 ± 1.3	0.482 ± 0.007	1.343 ± 0.008	64.1	[f]	0.895 ± 0.087
10×	8 ± 1	21	23.5	0.270 ± 0.011	1.244 ± 0.008	78.5	[f]	3.299 ± 0.387
9×	17	38	20.8 ± 1.3	0.285 ± 0.012	1.249 ± 0.002	77.2	0.042 ± 0.039	3.815 ± 0.291
8×	21 ± 1	48	23.3 ± 0.2	0.262 ± 0.012	1.254 ± 0.006	79.1	0.579 ± 0.024	5.972 ± 0.399
6×	70 ± 3	47	22.1 ± 1.6	0.287 ± 0.012	1.254 ± 0.003	77.1	0.101 ± 0.021	6.490 ± 0.423
1×	1440 ± 60	[f]	45.1 ± 3.0	0.687 ±0.029	1.352 ± 0.004	49.2	[f]	[f]
$InCl_3$								
2×	22 ± 2	[f]	24.5 ± 2.1	0.382 ± 0.057	1.244 ± 0.002	69.3	[f]	0.583 ± 0.083
1×	49 ± 4	[f]	20.2 ± 5.1	0.298 ± 0.044	1.238 ± 0.004	75.9	[f]	3.565 ± 0.234
1/2×	56 ± 5	[f]	18.9 ± 1.4	0.284 ± 0.009	1.224 ± 0.009	76.8	[f]	3.201 ± 0.190
1/4×	63 ± 8	[f]	17.7 ± 0.1	0.290 ± 0.001	1.251 ± 0.004	76.7	[f]	4.461 ± 0.231
1/8×	115 ± 15	[f]	18.7 ± 1.0	0.281 ± 0.002	1.241 ± 0.008	77.3	[f]	6.803 ± 0.564
$Ni(OTf)_2$								
16×	16 ± 3	[f]	27.2 ± 0.48	0.334 ± 0.014	1.258 ± 0.001	73.5	[f]	2.955 ± 0.197
4×	23	[f]	27.3 ± 0.22	0.338	1.219 ± 0.001	72.3	[f]	4.756 ± 0.514
2×	35	[f]	28.6 ± 0.26	0.345 ± 0.005	1.220 ± 0.001	71.8	[f]	9.135 ± 1.018
1×	76	[f]	23.1 ± 0.59	0.345 ± 0.008	1.225 ± 0.007	72.3	[f]	10.230 ± 4.812

[a] Average of five samples unless no error is indicated. [b] Shrinkage = 100 × (mold diameter − sample diameter)/(mold diameter). [c] Single sample, average of 50 measurements. [d] Calculated as $P = 100\times(r_s\text{-}r_b)/r_s$. [e] From SEM using ImageJ. Average of five particles. [f] Not measured.

Table 1. General material properties and gelation times of metal catalyzed PIR-PUR aerogels (cont.).

catalyst formulation	gelation time (min)		linear shrinkage (%)[a,b]	bulk density, ρ_b (g cm^{-3})[a]	skeletal density, ρ_s (g cm^{-3})[c]	porosity, Π (% v/v)[d]	BET surface area, σ (m^2 g^{-1})	skeletal particle diameter (μm)[e]
	phenomenological[a]	rheological						
$SnCl_4$								
4×	170 ± 10	[f]	18.6 ± 1.3	0.295 ± 0.023	1.218 ± 0.001	75.8	[f]	1.424 ± 0.144
2×	2 ± 1	[f]	22.7 ± 1.7	0.327 ± 0.008	1.220 ± 0.001	73.2	[f]	1.451 ± 0.082
1×	4 ± 1	[f]	23.1 ± 0.8	0.332 ± 0.004	1.252 ± 0.001	73.5	[f]	1.866 ± 0.169
1/2×	16 ± 2	[f]	19.9 ± 1.1	0.282 ± 0.031	1.236 ± 0.001	77.2	[f]	3.527 ± 0.332
1/4×	91 ± 5	[f]	19.7 ± 0.9	0.285 ± 0.009	1.248 ± 0.001	77.2	[f]	6.298 ± 0.791
$ZnCl_2$								
16×	39 ± 4	57	27.6 ± 1.5	0.357 ± 0.017	1.306 ± 0.026	72.7	0.563 ± 0.007	3.308 ± 0.337
8×	53 ± 4	78	24.9 ± 1.5	0.334 ± 0.007	1.195 ± 0.002	72.1	0.638 ± 0.009	3.170 ± 0.394
4×	81 ± 3	111	27.3 ± 2.7	0.366 ± 0.020	1.207 ± 0.002	69.7	0.325 ± 0.009	4.781 ± 0.678
2×	112 ± 0.5	127	24.7 ± 0.6	0.326 ± 0.007	1.208 ± 0.004	73.7	0.089 ± 0.015	3.374 ± 0.419
1×	152 ± 5	[f]	42.8 ± 1.5	0.797 ±0.072	1.212 ± 0.001	34.2	[f]	[f]

[a] Average of five samples unless no error is indicated. [b] Shrinkage = 100 × (mold diameter − sample diameter)/(mold diameter). [c] Single sample, average of 50 measurements. [d] Calculated as $P = 100\times(r_s\text{-}r_b)/r_s$. [e] From SEM using ImageJ. Average of five particles. [f] Not measured.

Appendix B.3: Thermal conductivity data of selected $CuCl_2$ catalyzed PIR-PUR aerogels.

Table 1. Thermal conductivity data of $CuCl_2$ catalyzed PIR-PUR aerogels at room temperature.

sample formulation [**bulk density, ρ_b (g cm^{-3})**][a]	**phenomenological gelation time (min)[b]** [**skeletal particle diameter (μm)**][a]	**total thermal conductivity, λ_{Total} (W m^{-1} K^{-1})[c]**	**porosity, Π (%)**	**surface area, σ (m^2 g^{-1})[a]**	**average pore diameter, ϕ (nm)[d]**	**gaseous thermal conductivity, λ_g (W m^{-1} K^{-1})[e]**	**solid thermal conductivity, λ_s (W m^{-1} K^{-1})[f]**
4× [0.422 ± 0.008]	4 [0.734 ± 0.132]	0.052 ± 0.001	65.4	1.28	4836.72	0.016	0.036
2× [0.483 ± 0.061]	5 [0.921 ± 0.129]	0.045 ± 0.002	60.9	0.47	10658.86	0.016	0.029
1/8× [0.326 ± 0.003]	19 [1.660 ± 0.340]	0.049 ± 0.002	73.5	1.29	6973.10	0.019	0.030
1/10× [g]	35 [g]	0.043 ± 0.001	g	g	g	0.019	0.024
1/13× [0.328 ± 0.005]	20 [3.917 ± 0.447]	0.041 ± 0.002	72.7	0.68	13045.95	0.019	0.022
1/16× [0.352 ± 0.011]	43 [g]	0.042 ± 0.001	71.7	0.29	28144.98	0.019	0.023
1/20× [0.309 ± 0.009]	61 [4.559 ± 0.714]	0.039 ± 0.002	74.9	0.10	93637.68	0.020	0.019
1/26× [0.299]	70 [6.212 ± 1.092]	0.036 ± 0.001	75.8	0.06	160257.45	0.020	0.016

[a] From Table B.2. [b] Measured with the large panels made for the thermal conductivity measurements. Fall in the range of the phenomenological gelation times of smaller samples reported in Table B.2. [c] Average of three samples. [d] Calculated via $f = 4 \times V_{Total}/s$. $V_{Total} = (1/\rho_b) - (1/\rho_s)$. [e] Calculated via Knudsen's equation, $\lambda_g = \lambda_{g,o}\Pi / [1+2\beta(l_g/\phi)]$, where $\lambda_{g,o}$ is the gaseous conductivity of the pore-filling gas (for air at room temperature and 1 bar pressure, $\lambda_{g,o} = 0.02619$ W m^{-1} K^{-1}); β is the energy transfer between the pore-filling gas and the aerogel walls (for air $\beta = 2$), l_g is the mean free path of the gas molecules (for air at room temperature and 1 bar $l_g = 70$ nm). [f] Calculated via $\lambda_s = \lambda_{Total} - \lambda_g$. [g] Not measured.

Appendix B.4: Figures of merit of the shape-memory effect.

Table 1. Strain fixity ratios ($R_f(N)$) of metal catalyzed PIR-PUR aerogels.[a.]

catalyst formulation	strain fixity ratio					
	cycle 1	cycle 2	cycle 3	cycle 4	cycle 5	Avg. of cycles 2-5
$AlCl_3$						
4×	99.27	99.27	99.27	99.27	99.34	99.29 ± 0.03
2×	99.21	99.22	99.22	99.22	99.16	99.21 ± 0.03
1×	99.12	99.16	99.17	99.16	99.15	99.16 ± 0.01
1/2×	99.18	99.16	99.17	99.17	99.18	99.17 ± 0.01
1/4×	99.18	99.17	99.19	99.21	99.17	99.19 ± 0.02
$CoCl_2$						
4×	99.15	99.17	99.18	99.17	99.18	99.18 ± 0.01
2×	99.08	99.09	99.11	99.12	99.12	99.11 ± 0.01
1/2×	98.91	98.91	98.92	98.93	98.93	98.92 ± 0.01
1/3×	99.13	99.18	99.18	99.19	99.21	99.19 ± 0.01
Cu_2Cl_2						
1×	99.15	99.14	99.12	99.12	99.11	99.12 ± 0.01
1/2×	99.11	99.14	99.16	99.15	99.16	99.15 ± 0.01
1/3×	99.14	99.16	99.15	99.18	99.14	99.16 ± 0.01
1/4×	99.06	99.07	99.08	99.09	99.09	99.08 ± 0.01
1/6×	99.23	99.22	99.24	99.23	99.21	99.22 ± 0.01
$CuCl_2$						
4×	98.98	98.99	99.00	99.02	99.01	99.01 ± 0.01
2×	99.18	99.17	99.19	99.21	99.17	99.19 ± 0.02
1×	99.18	99.16	99.17	99.17	99.18	99.17 ± 0.01
1/8×	99.12	99.16	99.17	99.16	99.15	$99.16 \pm 0.00_1$
1/13×	99.21	99.22	99.22	99.22	99.16	99.21 ± 0.03
1/20×	99.27	99.27	99.27	99.27	99.34	99.29 ± 0.03
1/26×	99.17	99.18	99.17	99.17	99.17	$99.17 \pm 0.00_1$
$FeCl_3$						
16×	99.10	99.11	99.12	99.11	99.12	$99.11 \pm 0.00_1$
10×	99.15	99.12	99.10	99.12	99.10	99.11 ± 0.01
8×	99.06	99.05	99.05	99.05	99.05	$99.05 \pm 0.00_1$
4×	99.02	99.02	99.05	99.05	99.05	99.04 ± 0.01
1×	99.16	99.14	99.15	99.15	99.15	99.15 ± 0.01

Table 1. Strain fixity ratios ($R_f(N)$) of metal catalyzed PIR-PUR aerogels (cont.).

catalyst formulation	strain fixity ratio					
	cycle 1	cycle 2	cycle 3	cycle 4	cycle 5	average of cycles 2-5
$GaCl_3$						
16×	99.34	99.36	99.36	99.37	99.37	99.37 ± 0.01
10×	99.27	99.23	99.23	99.24	99.24	99.24 ± 0.00[1]
9×	99.26	99.25	99.26	99.26	99.27	99.26 ± 0.01
8×	99.27	99.27	99.27	99.27	99.27	99.27 ± 0.00[1]
6×	99.27	99.28	99.29	99.31	99.32	99.30 ± 0.02
$InCl_3$`						
2×	99.05	99.07	99.06	99.05	99.06	99.06 ± 0.01
1×	99.20	99.16	99.16	99.22	99.17	99.18 ± 0.02
1/2×	99.17	99.17	99.15	99.16	99.15	99.16 ± 0.01
1/4×	99.24	99.24	99.24	99.24	99.25	99.24 ± 0.00[1]
1/8×	99.23	99.21	99.21	99.21	99.22	99.21 ± 0.00[1]
$Ni(OTf)_2$						
16×	99.10	99.79	99.11	99.09	99.09	99.27 ± 0.30
4×	99.16	99.15	99.16	99.17	99.17	99.16 ± 0.01
2×	99.18	99.19	99.19	99.19	99.19	99.19 ± 0.00[1]
1×	99.16	99.15	99.16	99.17	99.17	99.16 ± 0.01
$SnCl_4$						
4×	99.28	99.29	99.29	99.30	99.30	99.30 ± 0.00[1]
2×	99.27	99.29	99.29	99.27	99.28	99.28 ± 0.01
1×	97.89	99.37	99.37	99.37	99.38	99.37 ± 0.00[1]
1/2×	99.31	99.29	99.32	99.32	99.32	99.31 ± 0.01
1/4×	98.53	99.50	99.95	99.73	99.41	99.65 ± 0.21
$ZnCl_2$						
16×	99.22	99.23	99.23	99.25	99.25	99.24 ± 0.01
8×	99.10	99.16	99.15	99.15	99.16	99.16 ± 0.00[1]
4×	99.32	99.35	99.37	99.35	99.37	99.36 ± 0.01
2×	99.31	99.27	99.27	99.28	99.27	99.27 ± 0.00[1]

[a] Strain fixity ratio as a function of thermomechanical cycle (N):
$R_f(N) = 100 \times [\varepsilon_u(N)/\varepsilon_m(N)]$.

Table 2**.** Strain recovery ratios (R_r(N)) of all metal catalyzed PIR-PUR aerogels.[a]

catalyst formulation	strain recovery ratio					
	cycle 1	**cycle 2**	**cycle 3**	**cycle 4**	**cycle 5**	**average of cycles 2-5**
$AlCl_3$						
4×	84.60	82.45	81.62	81.12	80.74	81.48 ± 0.64
1×	86.40	84.77	84.07	83.66	83.37	83.97 ± 0.53
2×	88.78	87.60	86.99	86.54	86.14	86.82 ± 0.54
1/2×	91.62	90.41	89.90	89.57	88.75	89.66 ± 0.60
1/4×	92.88	92.51	92.76	92.29	92.32	92.47 ± 0.19
$CoCl_2$						
4×	81.76	79.32	78.12	77.27	76.51	77.81 ± 1.04
2×	87.72	86.46	85.82	85.30	84.90	85.62 ± 0.58
1/2×	81.20	79.55	78.84	78.37	77.96	78.68 ± 0.59
1/3×	82.30	80.59	79.65	79.12	78.59	79.49 ± 0.74
Cu_2Cl_2						
1×	85.12	83.87	83.48	83.32	82.99	83.42 ± 0.32
1/2×	89.11	87.54	86.82	86.36	85.87	86.65 ± 0.62
1/3×	85.48	84.58	83.89	83.99	84.24	84.18 ± 0.27
1/4×	89.43	87.80	87.13	86.92	86.46	87.08 ± 0.48
1/6×	89.08	87.85	87.37	87.02	86.82	87.27 ± 0.39
$CuCl_2$						
4×	84.46	82.81	81.97	81.41	81.13	81.83 ± 0.64
2×	90.66	88.93	88.26	87.88	87.77	88.21 ± 0.45
1×	96.12	94.77	93.83	92.87	91.72	93.30 ± 1.13
1/8×	95.81	94.58	94.04	93.77	93.58	93.99 ± 0.38
1/13×	96.75	95.41	94.88	94.58	94.31	94.80 ± 0.41
1/20×	97.55	95.96	95.30	94.87	94.33	95.12 ± 0.60
1/26×	98.65	99.64	99.81	99.50	99.29	99.56 ± 0.19
$FeCl_3$						
16×	86.15	83.81	82.83	82.13	81.67	82.61 ± 0.81
10×	90.57	89.30	88.72	88.35	88.09	88.62 ± 0.45
8×	90.53	88.82	88.35	87.94	87.76	88.22 ± 0.41
4×	90.46	88.99	88.35	88.17	88.04	88.39 ± 0.36
1×	89.63	88.53	88.06	87.78	87.63	88.00 ± 0.34

Table 2**.** Strain recovery ratios ($R_r(N)$) of all metal catalyzed PIR-PUR aerogels (cont).

catalyst formulation	strain recovery ratio					
	cycle 1	cycle 2	cycle 3	cycle 4	cycle 5	average of cycles 2-5
$GaCl_3$						
16×	97.27	95.84	94.99	94.31	93.79	94.73 ± 0.77
10×	97.76	96.09	95.43	95.02	94.7	95.31 ± 0.52
9×	97.2	95.89	95.28	94.99	94.61	95.19 ± 0.47
8×	97.21	95.68	95.34	95.02	94.53	95.14 ± 0.42
6×	89.18	86.63	86.07	85.65	85.37	85.93 ± 0.47
$InCl_3$						
2×	84.60	82.45	81.62	81.12	80.74	81.48 ± 0.64
1×	88.78	87.60	86.99	86.54	86.14	86.82 ± 0.54
1/2×	84.40	82.77	82.07	81.66	81.37	81.97 ± 0.53
1/4×	91.62	90.41	89.90	89.57	88.75	89.66 ± 0.60
1/8×	98.88	97.51	96.76	96.29	95.92	96.62 ± 0.59
$Ni(OTf)_2$						
16×	96.17	95.25	94.97	94.82	94.41	94.86 ± 0.30
4×	96.86	95.64	95.16	94.85	94.66	95.08 ± 0.37
2×	96.86	95.64	95.16	94.85	94.66	95.08 ± 0.37
1×	92.57	91.45	90.93	90.61	90.40	90.85 ± 0.40
$SnCl_4$						
4×	84.58	82.83	82.09	81.70	81.42	82.01 ± 0.53
2×	85.36	84.55	84.18	83.96	83.79	84.12 ± 0.28
1×	91.05	90.52	89.34	88.64	88.14	89.16 ± 0.89
1/2×	95.69	94.85	93.11	93.21	92.48	93.41 ± 0.88
1/4×	98.59	98.81	98.77	98.85	98.87	98.83 ± 0.04
$ZnCl_2$						
16×	88.24	87.29	86.77	86.46	86.18	86.68 ± 0.41
8×	85.42	84.07	83.61	83.22	82.98	83.47 ± 0.41
4×	83.61	82.11	81.36	80.98	80.66	81.28 ± 0.54
2×	87.78	86.78	86.34	86.11	85.94	86.29 ± 0.32

[a] Strain recovery ratio as a function of thermomechanical cycle (N): $R_r(N) = 100 \times s([\varepsilon_m(N) - \varepsilon_p(N)]/\varepsilon_m(N))$.

Table 3**.** Fill factors (*FF*(*N*)) of all metal catalyzed PIR-PUR aerogels.[a]

catalyst formulation	fill factor					
	cycle 1	cycle 2	cycle 3	cycle 4	cycle 5	average of cycles 2-5
$AlCl_3$						
4×	0.56	0.57	0.58	0.58	0.58	$0.58 \pm 0.00_1$
2×	0.59	0.59	0.59	0.58	0.58	0.59 ± 0.01
1×	0.57	0.57	0.57	0.57	0.57	$0.57 \pm 0.00_1$
1/2×	0.58	0.59	0.58	0.58	0.58	$0.58 \pm 0.00_1$
1/4×	0.62	0.62	0.62	0.62	0.62	$0.62 \pm 0.00_1$
$CoCl_2$						
4×	0.48	0.51	0.51	0.51	0.51	$0.51 \pm 0.00_1$
2×	0.47	0.47	0.48	0.48	0.48	$0.48 \pm 0.00_1$
1/2×	0.48	0.50	0.50	0.50	0.50	$0.50 \pm 0.00_1$
1/3×	0.48	0.48	0.49	0.49	0.49	$0.49 \pm 0.00_1$
Cu_2Cl_2						
1×	0.58	0.60	0.59	0.59	0.59	$0.59 \pm 0.00_1$
1/2×	0.56	0.57	0.56	0.57	0.56	$0.57 \pm 0.00_1$
1/3×	0.58	0.58	0.58	0.58	0.58	$0.58 \pm 0.00_1$
1/4×	0.61	0.60	0.61	0.59	0.61	0.60 ± 0.01
1/6×	0.57	0.59	0.58	0.57	0.57	0.58 ± 0.01
$CuCl_2$						
4×	0.50	0.52	0.53	0.53	0.53	$0.53 \pm 0.00_1$
2×	0.60	0.60	0.61	0.61	0.61	$0.61 \pm 0.00_1$
1×	0.59	0.59	0.60	0.60	0.61	0.60 ± 0.01
1/8×	0.59	0.60	0.59	0.60	0.59	0.60 ± 0.01
1/13×	0.62	0.62	0.61	0.62	0.62	$0.62 \pm 0.00_1$
1/20×	0.60	0.61	0.60	0.60	0.60	$0.60 \pm 0.00_1$
1/26×	0.61	0.61	0.62	0.62	0.62	$0.62 \pm 0.00_1$
$FeCl_3$						
16×	0.56	0.57	0.58	0.58	0.58	$0.58 \pm 0.00_1$
10×	0.59	0.59	0.59	0.58	0.58	0.59 ± 0.01
8×	0.57	0.57	0.57	0.57	0.57	$0.57 \pm 0.00_1$
4×	0.62	0.62	0.62	0.62	0.62	$0.62 \pm 0.00_1$
1×	0.58	0.58	0.58	0.58	0.58	$0.58 \pm 0.00_1$

Table 3. Fill factors (*FF*(*N*)) of all metal catalyzed PIR-PUR aerogels (cont).

catalyst formulation	fill factor					
	cycle 1	cycle 2	cycle 3	cycle 4	cycle 5	average of cycles 2-5
$GaCl_3$						
16×	0.54	0.58	0.57	0.56	0.57	0.57 ± 0.01
10×	0.63	0.64	0.64	0.64	0.64	$0.64 \pm 0.00_1$
9×	0.60	0.61	0.62	0.61	0.61	$0.61 \pm 0.00_1$
8×	0.61	0.62	0.61	0.61	0.61	$0.61 \pm 0.00_1$
6×	0.64	0.65	0.65	0.65	0.65	$0.65 \pm 0.00_1$
$InCl_3$						
2×	0.48	0.49	0.49	0.49	0.49	$0.49 \pm 0.00_1$
1×	0.58	0.60	0.61	0.61	0.61	$0.61 \pm 0.00_1$
1/2×	0.57	0.59	0.59	0.60	0.60	0.60 ± 0.01
1/4×	0.61	0.61	0.63	0.63	0.63	0.63 ± 0.01
1/8×	0.61	0.61	0.61	0.62	0.62	0.62 ± 0.01
$Ni(OTf)_2$						
16×	0.49	0.47	0.47	0.48	0.48	0.48 ± 0.01
4×	0.52	0.53	0.53	0.53	0.53	$0.53 \pm 0.00_1$
2×	0.57	0.57	0.56	0.56	0.56	$0.56 \pm 0.00_1$
1×	0.57	0.57	0.58	0.58	0.58	$0.58 \pm 0.00_1$
$SnCl_4$						
4×	0.62	0.63	0.62	0.62	0.62	$0.62 \pm 0.00_1$
2×	0.62	0.63	0.64	0.64	0.64	$0.64 \pm 0.00_1$
1×	0.60	0.63	0.64	0.63	0.64	0.64 ± 0.01
1/2×	0.62	0.63	0.62	0.62	0.62	$0.62 \pm 0.00_1$
1/4×	0.66	0.65	0.65	0.65	0.65	$0.65 \pm 0.00_1$
$ZnCl_2$						
16×	0.54	0.56	0.56	0.57	0.57	$0.57 \pm 0.00_1$
8×	0.55	0.57	0.57	0.58	0.57	$0.57 \pm 0.00_1$
4×	0.52	0.54	0.55	0.54	0.54	$0.54 \pm 0.00_1$
2×	0.54	0.57	0.55	0.57	0.56	0.56 ± 0.01

[a] Calculated as described in the main-paper text for each thermomechanical cycle (*N*).

Appendix B.5: Elastic modulus data of all PIR-PUR aerogels with all catalysts and catalyst concentrations.

Table 1**.** Elastic moduli, *E(N)*, of all metal catalyzed PIR-PUR aerogels.[a]

catalyst formulation	elastic modulus, MPa						skeletal particle diameter, μm[b]
	cycle 1	cycle 2	cycle 3	cycle 4	cycle 5	avg of cycles	
$AlCl_3$							
4×	0.2621	0.2511	0.2513	0.2511	0.2511	0.2512 ± 0.0001	0.563 ± 0.069
2×	0.0244	0.2322	0.2329	0.2329	0.2329	0.2327 ± 0.0003	1.125 ± 0.105
1×	0.1155	0.1019	0.1011	0.1012	0.1011	0.1013 ± 0.0003	1.250 ± 0.098
1/2×	0.0586	0.0516	0.0517	0.0516	0.0515	0.0516 ± 0.0001	2.180 ± 0.147
1/4×	0.0464	0.0448	0.0447	0.0447	0.0449	0.0448 ± 0.0001	2.875 ± 0.189
$CoCl_2$							
4×	0.1421	0.1015	0.1025	0.1010	0.1015	0.1016 ± 0.0005	3.242 ± 0.287
2×	0.1252	0.0963	0.0973	0.0963	0.0963	0.0966 ± 0.0004	4.176 ± 0.305
1/2×	0.0566	0.0560	0.0566	0.0560	0.0560	0.0562 ± 0.0003	6.415 ± 0.926
1/3×	0.0578	0.0550	0.0556	0.0550	0.0550	0.0552 ± 0.0003	11.208 ± 2.425
Cu_2Cl_2							
1×	0.0750	0.0535	0.0535	0.0535	0.0535	0.0535 ± 0.0001	3.874 ± 0.422
1/2×	0.0663	0.0510	0.0510	0.0510	0.0510	0.0510 ± 0.0001	5.206 ± 1.090
1/3×	0.0419	0.0338	0.0338	0.0338	0.0338	0.0338 ± 0.0001	2.919 ± 0.146
1/4×	0.0374	0.0312	0.0314	0.0314	0.0314	0.0314 ± 0.0001	11.209 ± 3.552
1/6×	0.0348	0.0295	0.0295	0.0295	0.0295	0.0295 ± 0.0001	8.090 ± 2.382
$CuCl_2$							
4×	0.2980	0.2651	0.2654	0.2660	0.2655	0.2655 ± 0.0003	0.734 ± 0.132
2×	0.1520	0.1476	0.1469	0.1469	0.1469	0.1471 ± 0.0003	0.9213 ± 0.129
1×	0.1443	0.1310	0.1321	0.1319	0.1311	0.1315 ± 0.0005	1.161 ± 0.111
1/8×	0.1175	0.1041	0.1042	0.1041	0.1041	0.1041 ± 0.0001	1.660 ± 0.340
1/13×	0.0891	0.0853	0.0854	0.0853	0.0853	0.0853 ± 0.0001	3.917 ± 0.447
1/20×	0.0552	0.0471	0.0470	0.0471	0.0472	0.0471 ± 0.0001	4.559 ± 0.714
1/26×	0.0788	0.0751	0.0753	0.0751	0.0758	0.0753 ± 0.0003	6.212 ± 1.092
$FeCl_3$							
16×	0.1318	0.1200	0.1200	0.1200	0.1200	0.1200 ± 0.0001	1.180 ± 0.192
10×	0.0655	0.0590	0.0590	0.0590	0.0590	0.0590 ± 0.0001	7.320 ± 0.968
8×	0.0622	0.0514	0.0514	0.0511	0.0511	0.0513 ± 0.0002	2.789 ± 0.228
4×	0.0501	0.0438	0.0438	0.0438	0.0438	0.0438 ± 0.0001	6.717 ± 1.254
1×	0.0361	0.0260	0.0260	0.0260	0.0260	0.0260 ± 0.0001	7.680 ± 1.459

Table 1. Elastic moduli, *E(N)*, of all metal catalyzed PIR-PUR aerogels (cont).

catalyst formulation	elastic modulus, MPa						skeletal particle diameter, μm[b]
	cycle 1	cycle 2	cycle 3	cycle 4	cycle 5	average of cycles 2-5	
$GaCl_3$							
16×	0.1515	0.1010	0.1012	0.1012	0.1012	0.1012 ± 0.0001	0.895 ± 0.087
10×	0.1212	0.0499	0.0499	0.0499	0.0499	0.0499 ± 0.0001	3.299 ± 0.387
9×	0.1313	0.0498	0.0498	0.0498	0.0498	0.0498 ± 0.0001	3.815 ± 0.291
8×	0.1151	0.0440	0.0440	0.0440	0.0440	0.0440 ± 0.0001	5.972 ± 0.399
6×	0.1182	0.0415	0.0415	0.0415	0.0415	0.0415 ± 0.0001	6.490 ± 0.423
$InCl_3$							
2×	0.1820	0.1692	0.1691	0.1691	0.1691	$0.1691 \pm 0.0000_1$	0.583 ± 0.083
1×	0.0440	0.0410	0.0411	0.0413	0.0411	0.0411 ± 0.0001	3.565 ± 0.234
1/2×	0.0480	0.0420	0.0419	0.0419	0.0419	$0.0419 \pm 0.0000_1$	3.201 ± 0.190
1/4×	0.0470	0.0370	0.0370	0.0370	0.0370	$0.0370 \pm 0.0000_1$	4.461 ± 0.231
1/8×	0.0310	0.0272	0.0274	0.0274	0.0274	0.0274 ± 0.0001	6.803 ± 0.564
$Ni(OTf)_2$							
16×	0.1429	0.1246	0.1246	0.1246	0.1246	$0.1246 \pm 0.0000_1$	2.955 ± 0.197
4×	0.0522	0.0482	0.0482	0.0481	0.0481	0.0482 ± 0.0001	4.756 ± 0.514
2×	0.0510	0.0440	0.0440	0.0440	0.0440	$0.0440 \pm 0.0000_1$	9.135 ± 1.018
1×	0.0420	0.0361	0.0361	0.0360	0.0361	$0.0361 \pm 0.0000_1$	10.230 ± 4.812
$SnCl_4$							
4×	0.1211	0.0922	0.0921	0.0921	0.0923	0.0922 ± 0.0001	1.424 ± 0.144
2×	0.0993	0.0872	0.0872	0.0871	0.0871	0.0872 ± 0.0001	1.451 ± 0.082
1×	0.0480	0.0431	0.0435	0.0433	0.0433	0.0433 ± 0.0001	1.866 ± 0.169
1/2×	0.0535	0.0333	0.0333	0.0330	0.0331	0.0332 ± 0.0001	3.527 ± 0.332
1/4×	0.0372	0.0285	0.0286	0.0287	0.0286	0.0286 ± 0.0001	6.298 ± 0.791
$ZnCl_2$							
16×	0.0912	0.0761	0.0760	0.0761	0.0761	$0.0761 \pm 0.0000_1$	3.308 ± 0.337
8×	0.0714	0.0632	0.0638	0.0634	0.0632	0.0634 ± 0.0002	3.170 ± 0.394
4×	0.0686	0.0586	0.0588	0.0588	0.0588	0.0588 ± 0.0001	4.781 ± 0.678
2×	0.0622	0.0510	0.0508	0.0501	0.0501	0.0505 ± 0.0004	3.374 ± 0.419

[a] Calculated as described in the main-paper text for each thermomechanical cycle (*N*).
[b] From SEM using ImageJ. Average of five particles.

BIBLIOGRAPHY

[1] Dunn, B.; Kamath, H.; Tarascon, J. M. Electrical Energy Storage for the Grid: A Battery of Choices. *Science* **2011**, *334*, 928.

[2] Manthiram, A.; Murugan, A. V.; Sarkar, A.; Muraliganth, T. Nanostructured Electrode Materials for Electrochemical Energy Storage and Conversion. *Energy Environ. Sci.* **2008**, *1*, 621-638.

[3] Alva, G.; Liu, L.; Huang, X.; Fang, G. Thermal energy storage materials and systems for solar energy applications. *Renew. Sustain. Energy Rev.* **2017**, *68*, 693-706.

[4] Scarfogliero, U.; Stefanini, C.; Dario, P. The use of compliant joints and elastic energy storage in bio-inspired legged robots. *Mech. Mach. Theory*, **2009**, *44*, 580-590.

[5] Tang, C.; Zhang, Q.; Zhao, M.-Q.; Tian, G.-L.; Wei, F. Resilient Aligned Carbon Nanotube/Graphene Sandwiches for Robust Mechanical Energy Storage. *Nano Energy*, **2014**, *7*, 161-169.

[6] Chen, K.; Xue, D. Materials Chemistry toward Electrochemical Energy Storage. *J. Mater. Chem. A*, **2016**, *4*, 7522-7537.

[7] Guerreiro, L.; Collares-Pereira, M. New Materials for Thermal Energy Storage in Concentrated Solar Power Plants. *AIP Conf. Proc.* **2016**, *1734*, 050018-1-8.

[8] Zhao, J. M.; Zhang, Z. M. Electromagnetic Energy Storage and Power Dissipation in Nanostructures *J. Quant. Spectrosc. Radiat. Transfer* **2015**, *151*, 49-57.

[9] Rasmussen, C. N.; Altiparmakis, A.; Däumling, M. Electromagnetic and electrostatic storage. *DTU International Energy Report* **2013**.

[10] IUPAC, Compendium of Chemical Terminology (the "Gold Book"), second ed., Blackwell Scientific Publications, Oxford, 1997.

[11] Vareda, J. P.; Lamy-Mendes, A.; Durães, L. A Reconsideration on the Definition of the Term Aerogel Based on Current Drying Trends. *Microporous Mesoporous Mater.* **2018**, *258*, 211−216.

[12] Kistler, S. S. Coherent Expanded Aerogels and Jellies. *Nature* **1931**, *127*, 741.

[13] Leventis, N.; Sadekar, A.; Chandrasekaran, N.; Sotiriou-Leventis, C. Click Synthesis of Monolithic Silicon Carbide Aerogels from Polyacrylonitrile-Coated 3D Silica Networks. *Chem. Mater.* **2010**, *22*, 2790- 2803.

[14] L. L. Hench, J. K. West. The Sol-Gel Process. *Chem. Rev.* **1990**, *90*, 33–72.

[15] (a) Rao, A. V.; Hegde, N. D.; Hirashima, H. Absorption and Desorption of Organic Liquids in Elastic Superhydrophobic Silica Aerogels. *J. Colloid Interface Sci.* **2007**, *305*, 124–132. (b) Rao, A. V.; Bhagat, S. D.; Hirashima, H.; Pajonk, G. M. Synthesis of Flexible Silica Aerogels Using Methyltrimethoxysilane (MTMS) Precursor. *J. Colloid Interface Sci.* **2006**, *300*, 279–285.

[16] Wang, C. T.; Wu, C. L.; Chen, I. C.; Huang, Y. H. Humidity Sensors Based on Silica Nanoparticle Aerogel Thin Films. *Sens. Actuators, B* **2005**, *107*, 402–410.

[17] Li, Y. K.; Yang, D. K.; Chen, Y. C.; Su, H. J.; Wu, J. C.; Chen-Yang, Y. W. A Novel Three-Dimensional Aerogel Biochip for Molecular Recognition of Nucleotide Acids. *Acta Biomater.* **2010**, *6*, 1462–1470.

[18] Rousset, J. L.; Boukenter, A.; Champagnon, B.; Dumas, J.; Duval, E.; Quison, J. F.; Serughetti, J. Granular Structure and Fractal Domains of Silica Aerogels. *J. Phys.* **1990**, *2*, 8445–8455.

[19] Pajonk, G. M.; Manzalji, T. Synthesis of Acrylonitrile from Propylene and Nitric Oxide Mixtures on Pbo_2-Zro_2 Aerogel Catalyst. *Catal. Lett.* **1993**, *21*, 361–369.

[20] Sayari, A.; Ghorbel, A.; Pajonk, G. M.; Teichner, S. J. Kinetics of The Catalytic Transformation of Isobutene into Methacrylonitrile with NO on Supported Nickel Oxide Aerogel. *React. Kinet. Catal. Lett.* **1981**, *15*, 459–465.

[21] Saeed, A. M.; Wisner, C. A.; Donthula, S.; Majedi Far, H.; Sotiriou-Leventis, C.; Leventis, N. Reuseable Monolithic Nanoporous Graphite-Supported Nanocatalysts (Fe, Au, Pt, Pd, Ni, and Rh) from Pyrolysis and Galvanic Transmetalation of Ferrocene-Based Polyamide Aerogels. *Chem. Mater.* **2016**, *28*, 4867−4877.

[22] Thapliyal, P. C.; Singh, K. Aerogels as Promising Thermal Insulating Materials: An Overview. *J. Mater.* **2014**, 127049-1-10.

[23] Hamann, T. W.; Martinson, A. B. F.; Elam, J. W.; Pellin, M. J.; Hupp, J. T. Atomic Layer Deposition of TiO_2 on Aerogel Templates: New Photoanodes for Dye-Sensitized Solar Cells. *J. Phys. Chem. C* **2008**, *112*, 10303–10307.

[24] Anandan, S.; Hebalkar, N.; Sarada, B. V.; Rao, T. N. In Aerospace Materials and Material Technologies; Prasad, N. E., Wanhill, R. J. H., Eds.; Springer: Singapore, **2017**; *Chapter 5*, pp 85-101.

[25] Coffman, B.; Fesmire, J.; White, S.; Gould, G.; Augustynowicz, S. Aerogel Blanket Insulation Materials for Cryogenic Applications. *Adv. Cryog. Eng.* **2010**, *1218*, 913- 920.

[26] Xia, W.; Qu, C.; Liang, Z.; Zhao, B.; Dai, S.; Qiu, B.; Jiao, Y.; Zhang, Q.; Huang, X.; Guo, W.; Dang, D.; Zou, R.; Xia, R.; Xu, R.; Liu, M. High-Performance Energy Storage and Conversion Materials Derived from a Single Metal–Organic Framework/Graphene Aerogel Composite. *Nano Lett.* **2017**, *17*, 2788-2795.

[27] Werner J. Blank, Z.A. He, E.T. Hessell, Catalysis of the isocyanate-hydroxyl reaction by non-tin catalysts, *Progress in Organic Coatings*, *Volume 35*, Issues 1–4, **1999**, Pages 19-29, https://doi.org/10.1016/S0300-9440(99)00006-5.

[28] Meador, M. A. B.; McMillon, E. Sandberg, A.; Barrios, E.; Wilmoth, N. G.; Mueller, C. H.; Miranda, F. A. Dielectric and Other Properties of Polyimide Aerogels Containing Fluorinated Blocks. *ACS Appl. Mater. Interfaces* **2014**, *6*, 6062–6068.

[29] Meador, M. A. B.; Wright, S.; Sandberg, A.; Nguyen, B. N.; Keuls, F. W. V.; Mueller, C. H. Rodriguez-Solis, R.; Miranda, F. A. Low Dielectric Polyimide Aerogels as Substrates for Lightweight Patch Antennas. *ACS Appl. Mater. Interfaces* **2012**, *4*, 6346–6353.

[30] Hong, J.-Y.; Wie, J. J.; Xu, Y.; Park, H. S. Chemical Modification of Graphene Aerogels for Electrochemical Capacitor Applications. *Phys. Chem. Chem. Phys.* **2015**, *17*, 30946-30962.

[31] (a) Kistler, S. S. Coherent Expanded Aerogels and Jellies. *Nature* **1931**, *127*, 741. (b) Kistler, S. S. The Relation between Heat Conductivity and Structure in Silica Aerogel. *J. Phys. Chem.* **1934**, *39*, 79-86. (c) Lu, X.; Caps, R.; Fricke, J.; Pekala, R. W. Correlation between Structure and Thermal Conductivity of Organic Aerogels. *J. Non-Cryst. Solids* **1995**, *188*, 226-234.

[32] http://www.aerogeltechnologies.com/silica-aerogel-samples.

[33] Pierre, A. C.; Pajonk, G. M. Chemistry of Aerogels and Their Applications. *Chem. Rev.* **2002**, *102*, 4243−4265.

[34] (a) Gould, G. L.; Lee, J. K.; Stepanian, C. J.; Lee, K. P. High Strength, Nanoporous Bodies Reinforced with Fibrous Materials. U. S. Patent Application 20070222116, 2007. (b) Ryu, J. Flexible Aerogel Superinsulation and its Manufacture. U. S. Patent 6068882A, 2000.

[35] Harasim, S. Building Envelope Applications for Reinforced Flexible Aerogel Insulation Blankets. Aspen Aerogels Inc. 2011.

[36] (a) Wittwer, V. Development of Aerogel Windows. *J. Non-Cryst. Solids* **1992**, *145*, 233–236. (b) Gerlach, R.; Kraus, O.; Fricke, J.; Eccardt, P. C.; Kroemer, N.; Magori, V. Modified SiO_2 Aerogels as Acoustic Impedance Matching Layers in Ultrasonic devices. *J. Non-Cryst. Solids* **1992**, *145*, 227–232.

[37] Pajonk, G. M. Aerogel Catalysts. *Appl. Catal.* **1991**, *72*, 217–266.

[38] Cantin, M.; Casse, M.; Koch, L.; Jouan, R.; Mestreau, P.; Roussel, D.; Saclay, C.; Bonnin, F.; Moutel, J.; Teichner, S. J. Silica aerogels used as Cherenkov radiators. *Nucl.Instrum.Meth.* **1974**, *118*, 177-182.

[39] Lagamba, L.; Cisbani, E.; Colilli, S.; Crateri, R.; Leo, R. D.; Frullani, S.; Garibaldi, F.; Giuliani, F.; Gricia, M.; Iodice, M.; Iommi, R.; Leone, A.; Lucentini, M.; Mostarda, A.; Nappi, E.; Perrino, R.; Pierangili, L.; Santavenere, F.; Urciuoli, G. M. Silica Aerogel Threshold Cherenkov Counters for the Jlab Hall A Spectrometers: Improvements and Proposed Modifications. *Nucl. Instr. Meth. Phys. Res. A.* **2001**, *471*, 325–332.

[40] (a) Leventis, N. Three-Dimensional Core-Shell Superstructures: Mechanically Strong Aerogels. *Acc. Chem. Res.* **2007**, *40*, 874-884. (b) Leventis, N.; Mulik, S.; Wang, X.; Dass, A.; Sotiriou-Leventis, C.; Lu, H. Stresses at the Interface of Micro with nano. *J. Am. Chem. Soc.* **2007**, *129*, 10660-10661. (c) Leventis, N.; Sotiriou-Leventis, C.; Zhang, G.; Rawashdeh, A.-M. M. Nano Engineering Strong Silica Aerogels. *Nano Lett.* **2002**, *2*, 957-960.

[42] Du, A., Zhou, B., Zhang, Z.; Shen, J. A special material or a new state of matter: A review and reconsideration of the aerogel. *Materials*, **2013**, *6(3)*, 941-968.

[43] Hajar Maleki, Luisa Durães, António Portugal, An overview on silica aerogels synthesis and different mechanical reinforcing strategies, *J.Non-Crystalline Solids*, **2014**, *385*, 55-74. https://doi.org/10.1016/j.jnoncrysol.2013.10.017.

[44] Meador M. A. B.; Fabrizio E. F.; Ilhan F.; Dass A.; Zhang, G.; Vassilaras, P.; Johnston, J.C.; Leventis, N. *Chem. Mater.* **2005** *17* (5), 1085-1098, DOI: 10.1021/cm048063u

[45] Wu, D.; Xu. F.;Sun, B.; Fu, R.; He, H; Matyjaszewski, K. *Chemical Reviews* **2012** *112* (7), 3959-4015, DOI: 10.1021/cr200440z

[46] Pekala, R. W.; Schaefer, D. W. *Macromolecules* **1993**, *26*, 5487

[47] Leventis, N.; Palczer, A.; McCorkle, L. Nanoengineered Silica-Polymer Composite Aerogels with No Need for Supercritical Fluid Drying. *J. Sol-Gel Sci. Tech.* **2005**, *35*, 99–105. https://doi.org/10.1007/s10971-005-1372-7

[48] Lei, Y.; Hu, Z.; Cao, B.; Chen, X.; Song, H. Enhancements of thermal insulation and mechanical property of silica aerogel monoliths by mixing graphene oxide. *Mater. Chem. Phys.*, **2017**, *187*, 183-190. https://doi.org/10.1016/j.matchemphys.2016.11.064.

[49] Y. Liu , J. Goebl and Y. Yin , Chem. Soc. Rev., 2013, 42 , 2610 —2653

[50] Ligon, S. C.; Liska, R.; Stampfl, J.; Gurr, M.; Mülhaupt, R. *Chemical Reviews*, **2017**, *117*, 10212-10290. DOI:10.1021/acs.chemrev.7b00074.

[51] Kshetrimayum, R. S. A brief intro to metamaterials, *IEEE Potentials*, **2004**, *23*, 44-46.

[52] Huang, C.; Chen, L. Negative Poisson's ratio in modern functional materials, *Advanced Materials*, **2016**, *28*, 8079-96.

[53] He, J. H.; Huang, H. H. Tunable acoustic wave propagation through planar auxetic metamaterial, *Journal of Mechanics*, **2017**, *1*,10.

[54] Han, Y.; Zhou, Y.; Qin, G.; Dong, J.; Galvao, D. S.; Hu, M. Unprecedented mechanical response of the lattice thermal conductivity of auxetic carbon crystals, *Carbon*, **2017**, *122*, 374-80.

[55] Poisson, S. D.; Gay-Lussac, L. J.; Arago, F. *Ann. Chim. Phys.* **1857,** *36*, 384-85.

[56] Mullin, T.; Deschanel, S.; Bertoldi, K. Boyce, M. C. *Phys. Rev. Lett.* **2007**, *99*, 084301.

[57] Bertoldi, K.; Reis, P. M.; Willshaw, S.; Mullin, T. *Adv. Mater.* **2010**, *22*, 366.

VITA

A B M Shaheen ud Doulah was born in Dhaka, Bangladesh. He received his Bachelor of Science in Applied Chemistry and Chemical Engineering and Masters of Science in Applied Chemistry and Chemical Engineering from the University of Dhaka, Bangladesh, in December 2009 and April 2012, respectively. After his graduation, in 2012, he started his first job in Bangladesh at DIRD Felt Ltd. as a research and development executive and worked there for 2 years. In May 2014, he moved to Bangladesh Material Testing Limited, Bangladesh as a technical manager and worked there for three years.

In January 2018, Sheheen started his doctoral study at Missouri University of Science and Technology, Rolla, USA. He worked in multiple projects under the guidance of Prof. Chariklia Sotiriou-Leventis and co-advisor Dr. Nicholas Leventis. He presented his research work at 261st ACS National Meeting in April 2021 and at ACS Midwest Regional Meeting in October 2022. In July 2023, he received his Doctor of Philosophy in Chemistry from Missouri University of Science and Technology, Rolla, MO, USA. He was a member of the American Chemical Society. Shaheen was a co-inventor of recently filed two U.S. Provisional Patent Applications entitled “Amorphous and graphitic carbon aerogels from compressed xerogel powders.” (Application Serial No. 63/170,827) and “Poly(tetrahydroquinazoline) and derived carbons” (Application Serial No. 63/170,614). Shaheen has four papers published and 1 submitted.